The Atacama Cosmology Telescope

Daniel S. Swetz

A DISSERTATION

in

Physics and Astronomy

Presented to the Faculties of the University of Pennsylvania

in Partial Fulfillment of the Requirements for the degree of Doctor of Philosophy

2009

Mark Devlin

Supervisor of Dissertation

Ravi Sheth

Graduate Group Chairperson

Acknowledgements

Over the course of my graduate career, I have had the opportunity to interact with and learn from many people. I am indebted to all of them, as they made this research possible.

First, I would like to acknowledge my advisor, Mark Devlin. He has supervised me in all aspects of my research, and provided me with numerous opportunities to develop my skills as an experimental physicist. Under his guidance, I have been able to work on almost every aspect of ACT. Mark been a mentor and friend throughout my time in Graduate school.

I would like to thank Professors Lyman Page, Suzanne Stages, and Joe Fowler of Princeton University and Professor Mark Halpern of the University of British Columbia. It is through their tireless efforts that projects like ACT succeed. They have all answered hundreds of my emails, and have always taken time out of their busy schedules to answer and explain any questions I had. I have had the pleasure of personally working with each of them in the field, and this field time has been some of the best learning experiences for me. Their guidance and expertise has made me a better scientist.

I owe a great deal of gratitude to Jeff Klein. Jeff seems to know almost everything about physics, science, and life in general. He has taught me a considerable amount about experimental physics, almost always by working directly with me. His sense of humor has always eased the pain of long days and nights spent working on the project.

The design of MBAC would not have been possible without Bob Thornton, Michele Limon, and Simon Dicker. They, along with Madhuri Kaul and Danica Marsden, were instrumental to the construction, assembly, and testing of the instrument at Penn, and were always willing to spend the time necessary to meet the deployment deadlines.

I would like to acknowledge all of the professors, research scientists, postdoctoral researchers, and graduate students who worked on ACT, including: Judy Lau, Mike Niemack, Toby Marriage, Eric Switzer, Adam Hincks, Yue Zhao, Ryan Fisher, Tom Essinger-Hileman, John Appel, Lucas Parker, Sudeep Das, Amir Hajian, Viviana Acquaviva, Rolondo Dünner, Beth Reid, Kevin Huffenburger, Elia Battistelli, Matt Hasselfield, Mike Nolta, John Sievers, Neelima Sehgal, Matt Hilton, Jo Dunkley, Norm Jarosik, Kavi Moodley, David Spergel, Omelan Stryzak, and Robert Lupton. Over the years, I have worked with all of them, often in field, in the lab, at collaboration meetings and design reviews, endless telecons and late-night Skype chats. They have all contributed in significant ways to ACT and to the research presented here.

I have also had the opportunity to work with many other students while at Penn, particularly those in the Devlin Lab. Chris Semisch, Marie Rex, Fritz Stabenau, Matt Truch, Mark Supanich, and Phil Korngut have always made time to help solve my problems and made my time here quite enjoyable. I owe a great deal of thanks to Chris for the many times he helped take care of my dogs while I was in the field.

Finally, I would like to thank my wife, Rachel. Being the spouse of an experimental physicist is not easy, with long nights and extended periods of travel. She has never failed to provide me with the necessary love and support to pursue my goals. I love her dearly and this thesis is dedicated to her.

ABSTRACT

The Atacama Cosmology Telescope

Daniel S. Swetz

Mark Devlin

The Atacama Cosmology Telescope (ACT) is a 6-meter diameter telescope designed to make detailed measurements at millimeter wavelengths with arcminute resolution. The telescope is located at an altitude of 5,190 meters in the Atacama desert in the Chilean Andes. The primary science instrument for ACT is the Millimeter Bolometer Array Camera (MBAC). MBAC measures the Cosmic Microwave Background (CMB) temperature anisotropy at angular scales corresponding to multipole $100 \lesssim l \lesssim 10{,}000$. It contains three separate kilo-pixel arrays of transition-edge sensor (TES) bolometers in frequency bands centered at 145, 220, and 280 GHz. At small angular scales, the temperature anisotropies are dominated by interactions of CMB photons with large-scale structure on their transit from the surface of last scattering to the observer. The largest signal arises from the thermal Sunyaev-Zel'dovich (tSZ) effect, a spectral distortion of the CMB caused by inverse-Compton scattering of CMB photons as they pass through hot gas in clusters of galaxies. By combining the millimeter-wave tSZ galaxy-cluster measurements with optical and X-ray data, the masses, temperatures, and redshifts of the clusters can be determined. The cluster density function (number counts as a function of redshift) will help map out the

growth of structure in the universe. The measure of structure formation will help constrain the dark-energy equation of state.

My thesis discusses the scientific background and motivation for ACT. I present on overview of the telescope design, the alignment of the mirrors, and the choice of the site location and scan strategy. A detailed design of the MBAC receiver is given, including the integration of the bolometer arrays and their multiplexed readout; the cold, refractive, reimaging optics; the band-defining filters; the liquid-cryogens-free system employed to cool the optics and arrays; and the structural interface and alignment to the telescope. I report on the characterization and performance of the receiver during the commissioning in the fall of 2007. I present an analysis of targeted planet observations that were used to assess the beam shape, optical alignment, telescope stability, and to develop a night-by-night corrected pointing model. Finally, I discuss the preliminary science results from the 2008 season.

Contents

List of Tables

List of Figures

Chapter 1

ACT Science

New experiments in observational cosmology are providing crucial data that allow us to test theories about the origin and evolution of the Universe. These studies, combined with theoretical efforts, have led to the development of a cosmological standard model based on the Big Bang theory. The basic framework of the model involves the expansion of the Universe from a hot, nearly homogeneous state at early times, followed by the cooling and evolution of matter and energy, to form the locally inhomogeneous state we see today. While the new wealth of cosmological data has provided much information about the Universe, there are still unanswered questions about the conditions in the early Universe, the formation and growth of cosmic structure over time, and the values of the fundamental parameters that govern the Universe. The purpose of this chapter is to give the scientific background and motivation for undertaking the Atacama Cosmology Telescope (ACT) project. The first section gives a brief introduction to modern cosmology. The second section describes the Cosmic Microwave Background (CMB) radiation and summarizes the most recent measurements that have been made. These results, when combined with other data

sets, imply that nearly 70% of the energy in the Universe is in an exotic form known as "dark energy". The consequences of dark energy and possible explanations and tests are discussed in the third section. The fourth section discusses one potential probe of dark energy: galaxy clusters, and in particular their detection through the Sunyaev-Zel'dovich (SZ) effect. The final section discusses the ACT project, the goals of the research and a summary of observations to date.

1.1 Introduction

Modern cosmology began in the early half of the 20th century with Einstein's Theory of General Relativity (GR) and Hubble's observation of an expanding universe. With these breakthroughs, cosmology became a quantitative science.

In 1929, Edwin Hubble, measuring the optical spectra of variable stars in extragalactic nebulae, provided the first evidence for an expanding universe. Hubble showed that distant galaxies are receding from us at a rate proportional to their distance from us, thus ruling out a static universe [Hubble, 1929]. This result, which has become known as Hubble's Law, is given simply by

$$v = H_0 d \tag{1.1}$$

where v is the recessional velocity of the galaxy, d is its the distance and H_0 is Hubble's constant which is $\simeq 70\,\mathrm{km\,s^{-1}\,Mpc^{-1}}$.

Objects[1] that are moving apart must have been closer together in the past. When extrapolated backwards sufficiently, Hubble's law predicts that at some point, all

[1] "Objects" normally do not expand because most objects (stars, galaxies, clusters) are gravitationally bound.

matter would collide in a hot dense state, from which it expanded outward. This has since become known as the Big Bang theory.

Since Hubble's first measurement, much effort, both theoretical and experimental, has gone into understanding the expansion, evolution, and ultimate fate of the Universe within the framework of GR and the Big Bang theory. A homogeneous and isotropic space is described the Roberston-Walker metric[2]. This assumption, often called the cosmological principle, appears valid on the largest scales of the Universe[3]. Using the Roberston-Walker metric and the equations of GR, the evolution of the Universe is given by the Friedmann equations:

$$\frac{\ddot{a}(t)}{a(t)} = -\frac{4\pi G}{3}(\rho(t) + 3p(t)) + \frac{\Lambda}{3} \tag{1.2}$$

and

$$\left(\frac{\dot{a}(t)}{a(t)}\right)^2 = \frac{8\pi G\rho(t) + \Lambda}{3} - \frac{\kappa}{a^2(t)}, \tag{1.3}$$

where G is Newton's constant, ρ is the density of matter and radiation, p is their pressure, κ is the curvature of the Universe, Λ is the vacuum energy, and $a(t)$ is the scale factor as a function of time t. Here, units are given with $\hbar = c = k_B = 1$. If the vacuum energy is not precisely equal to: $3\kappa/a^2(t) - 8\pi G\rho(t)$, solutions to $a(t)$ will not be static and the Universe will be either expanding or contracting. Radiation traveling in an expanding or contracting universe will be stretched or compressed.

[2]For a recent review, see eg: Dodelson [2003] and Carroll [2003].

[3]The evidence supporting the cosmological principle comes from a number of different observations including number counts of galaxies in space, observations of the diffuse X-ray background, and the CMB, which is discussed in Section 1.2

This stretching is characterized by the redshift z, defined as

$$1 + z \equiv \frac{\lambda_{obs}}{\lambda_{emit}} = \frac{1}{a} \tag{1.4}$$

where $z = 0$ at present. The density of matter scales with the volume expansion of the Universe as $\rho_m \propto a^{-3}$, while the density of radiation scales at $\rho_{rad} \propto a^{-4}$ because photons also lose energy from a^{-1} redshift expansion. Here we have assumed a constant[4] Λ, with $p = -\rho$, and $\rho_\Lambda \propto a^0$. We can further define the Hubble parameter $H(t) \equiv \frac{\dot{a}(t)}{a(t)}$ and density parameters $\Omega_i = \rho_i/\rho_{crit}$, where $\rho_{crit} \equiv \frac{3H_0^2}{8\pi G}$ and is called the critical density and H_0 is the value of the Hubble parameter today (the Hubble constant). We can then write equation 1.3 as

$$H(z) = H_0\sqrt{\Omega_\Lambda + \Omega_\kappa(1+z)^2 + \Omega_m(1+z)^3 + \Omega_{rad}(1+z)^4}, \tag{1.5}$$

where redshift has been substituted for time; Ω_κ = 1 - $\sum_i \Omega_i$ = -κ/H_0^2 determines the shape of the Universe. The values of the density parameters dictate the expansion and evolution of the Universe. Measuring these cosmological parameters and understanding their implications is a primary goal of modern cosmology.

1.2 The Cosmic Microwave Background

A direct prediction of the Big Bang is the existence of a thermal radiation permeating all of space. This Cosmic Microwave Background (CMB) radiation was first predicted in by Alpher, Bethe, and Gamow [1948] and measured by Penzias and Wilson [1965]. The existence of the CMB is still the most compelling evidence for the

[4]The equation of state is assumed to follow $p = w\rho$ with constant w in time. Then $\rho \propto a^{-3(1+w)}$. For matter, $w = 0$, for photons, $w = 1/3$, for a cosmological constant, w = -1.

Big Bang.

The CMB arises because at very early times, the density in the early Universe was high enough to produce a temperature hot enough to prevent neutral hydrogen from forming [Dodelson, 2003]. Inverse-Compton scattering of photons by free electrons, and Coulomb interactions between free electrons and protons, produced a tightly coupled photon-electron-baryon plasma throughout the Universe. The photon-field was so dense — there are $\sim 10^{10}$ photons for every baryon — that the photons ionized matter faster than it could recombine. As the Universe expanded, the density decreased and the photon wavelengths were redshifted, both leading to a cooling of the Universe. The ionization and recombination can be expressed in terms of the energy densities as the matter and energy densities scale differently (as discussed in Section 1.1). Recombination happens when the photon scattering cross section drops below the expansion rate, approximately when the mean photon path length is the size of the horizon. This occurred at a redshift of $\simeq 1100$, when the Universe was $\sim$ 380,000 years old. Free electrons and protons became bound in mostly neutral hydrogen and helium and the Universe became nearly transparent to the photons. These photons free-stream to us from all directions. The CMB is therefore the remnant thermal radiation produced roughly 380,000 years after the Big Bang.

The spectrum of the CMB has been measured by the Far-InfraRed Absolute Spectrometer (FIRAS) on the Cosmic Background Explorer (COBE) and found to follow a nearly perfect blackbody spectrum, with a temperature of $T_{CMB} \approx 2.73\,\mathrm{K}$, as shown in Figure 1.1. The FIRAS measurement, along with balloon-born, ground-based, and rocket experiments, have confirmed that the CMB has the same characteristic blackbody on all angular scales. The horizon size at the surface of last scattering is $\sim 1^\circ$ today. Regions of sky at angular sizes larger than the horizon size have had no

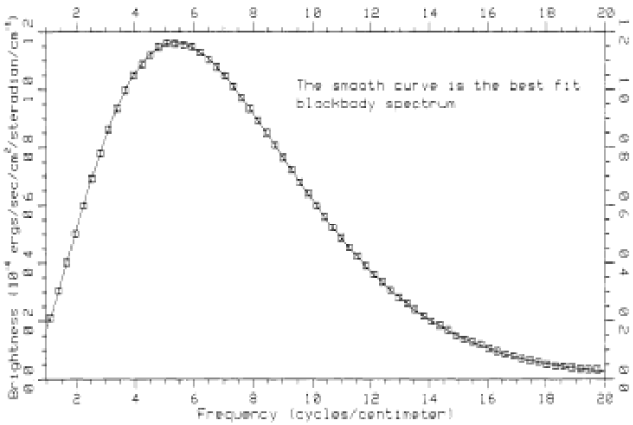

Figure 1.1 The CMB blackbody spectrum as measured by the FIRAS experiment aboard the COBE satellite. Overplotted is a blackbody with temperature of 2.73 K. Figure from Mather et al. [1990].

causal contact, hence it seems unlikely that measurements of the temperature of the CMB blackbody on scales larger than the horizon should be at the same temperature. To explain the large-scale homogeneity that has been observed at all angular scales (40,000 square degrees), a period of exponential expansion, or inflation, in the very early Universe, $\sim 10^{-35}$ seconds after the Big Bang, has been hypothesized. In this model, the entire visible Universe was originally in causal contact and inside the horizon scale at the time of the expansion. Following this extremely rapid expansion, universal causal connectiveness is lost, but the original uniformity of the Universe is imprinted on much larger, no longer connected scales. Since the CMB is generated after this expansion, a uniform temperature on all scales is expected.

1.2.1 Temperature Anisotropies of the CMB

Small density fluctuations at the surface of last scattering gave rise to gravitational instabilities which led to the growth of the present structure in the Universe. These tiny density fluctuations induce small ($\sim 10^{-5}$ K) temperature fluctuations in

the CMB. The angular scales at which these temperature fluctuations occur provide information about the cosmological parameters which dictate the expansion and evolution of the Universe. To quantify the temperature anisotropy, the size of the fluctuations are decomposed into a series of spherical harmonics Y_{lm} with amplitudes a_{lm} as,

$$\frac{\Delta T(\theta,\phi)}{T_{CMB}} = \sum_{l=1}^{l=\infty} \sum_{m=-l}^{l} a_{lm} Y_{lm}(\theta,\phi), \tag{1.6}$$

where θ and ϕ are the spherical angles on the sky, l is the spherical harmonic multipole number, and m is the directional index. Spherical harmonics are a natural choice because the surface of last scattering appears as a sphere on the sky. The angular power spectrum is then defined as

$$C_l = \langle a_{lm} a^*_{lm} \rangle = \frac{1}{2l+1} \sum_{m=-l}^{l} \mid a_{lm} \mid^2 \tag{1.7}$$

where brackets indicate an ensemble average over m, appropriate for a homogeneous and isotropic universe. The angular size on the sky is then inversely proportional to multipole expansion l, with $l \approx \pi/\theta$ for angle θ in radians.

The CMB power spectrum has been measured out to $l \sim 2500$ by several experiments. The most precise measure has come from the Wilkinson Microwave Anisotropy Probe (WMAP) which measured the angular power spectrum out to $l \sim 800$ [Nolta et al., 2009]. Figure 1.2 shows its most recent results. Studies of the temperature variations of the CMB sky and subsequent power-spectrum analysis have revealed much about the geometry, age, and contents of the Universe [Dunkley et al., 2009]. These data, when combined with big-bang nucleosynthesis, galaxy and supernovae surveys, tightly constrain cosmological parameters, leading to a standard model of cosmology,

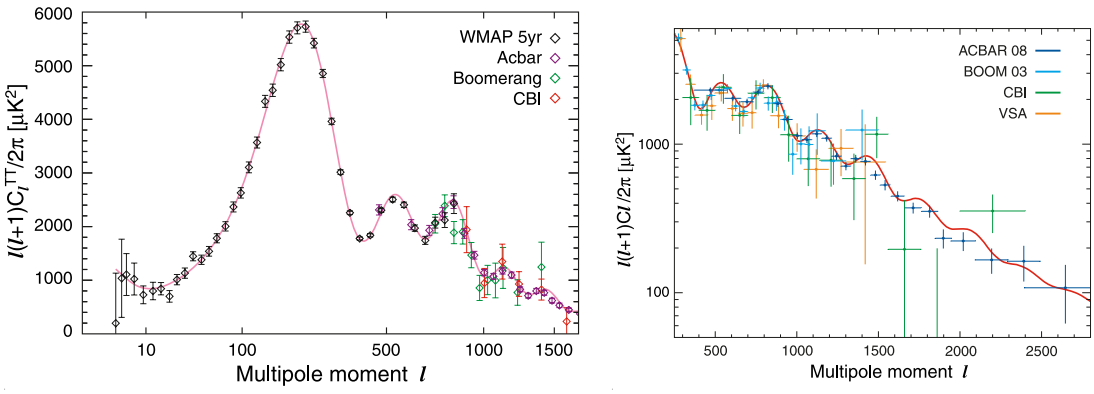

Figure 1.2 Recent measurements of the CMB angular power spectrum. The amplitude and location of the peaks in the spectrum encode information about the cosmological parameters. *Left*: The angular power spectrum at low multipoles (large angular scales, $\theta \gtrsim 0.2°$). The red curve is the best fit ΛCDM cosmology model. Figure from Nolta et al. [2009]. *Right*: The angular power spectrum at high multipole (small angular scales up to $\theta \approx 4$ arcminutes). There are few experiments beyond l of 2500; ACT will probe to $l \sim 10,000$ ($\theta \approx 1$ arcminute). Figure from Dunkley et al. [2009].

the ΛCDM model; for a recent survey see Komatsu et al. [2009]. The picture that has emerged is a universe that is flat ($\Omega_\kappa = 0$), with baryonic matter density $\Omega_b \approx 4\%$. The total matter density Ω_m is approximately 27% and mostly in the form of cold dark matter (CDM) that only interacts with normal matter gravitationally. Perhaps the most surprising consequence of the ΛCDM model is that the remaining 73% of the matter-energy content of the Universe in an exotic form of "energy" known as dark energy. This dark energy is apparently causing the rate of expansion of the Universe to increase recently (z $\lesssim$ 1).

Beyond multipole $l \gtrsim 900$, the primordial temperature anisotropies become greatly reduced in amplitude from photon diffusion during the period of recombination. This effect, known as Silk damping [Silk, 1968], arises from the finite thickness of the surface of last scattering. The scale of this damping records the period over which recombination happened, because scattering events during this period erase temper-

ature anisotropies at and below the recombination length scale. Beyond $l \sim 3000$, this damping is large enough that secondary temperature anisotropies become the dominant signal. These secondary anisotropies are not primordial, but originate from interactions of CMB photons with matter and hence structure as they propagate through the Universe. Therefore, measurements of the CMB on these angular scales can help us to understand the growth and evolution of structure. The largest of these secondary anisotropies is discussed in Section 1.4.1.

1.3 Accelerated Expansion and Dark Energy

Understanding the nature of dark energy is at the heart of cosmology and physics in general. With current measurement limits and theoretical understanding, there are three ways to explain this mysterious energy. The simplest explanation is that the dark energy arises from a constant vacuum energy. In this case, the Universe would have a cosmological constant, described by Λ in Equations 1.2 and 1.3, with $\Omega_\Lambda \approx 73\%$. Since Λ is proportional to the amount of space, its effect on expansion increases as the Universe grows. In the past, the Universe would have been matter-dominated; Λ would have not yet altered the expansion history and would not have been observable. In the future, the cosmological constant will dominate the energy density of the Universe and the contents of the Universe will continue to separate from one another with ever-growing acceleration. Taken to the extreme, in some distant future, the distance between all objects not gravitationally bound will become such that the light-travel time will be greater than the age of the Universe. Distant objects will be undetectable and we will find ourselves inhabiting what appears to be an empty universe. The cosmological constant explanation is unsatisfying because without a

theoretical motivation for its value, it appears that we are living in a unique time in the expansion history of the Universe, one where we can observe its effects. A cosmological constant is in fact predicted by many quantum field theories, but the predicted magnitude is of order 10^{100} too large and no explanation for the discrepancy has been found. Another explanation is that the dark energy is evolving in time, with a new field or unknown particle missing from the standard model of cosmology. This is quantified by the dark energy equation of state w_Λ:

$$w_\Lambda = p_\Lambda / \rho_\Lambda, \tag{1.8}$$

where p_Λ and ρ_Λ are the pressure and density of the dark energy. There are two possible scenarios if this is the case. If w_Λ is constant, then its energy density evolves as $\rho_\Lambda \propto a^{-3(1+w_\Lambda)}$. For any value of $w_\Lambda \neq -1$, the dark energy Ω_Λ is no longer constant but evolves with the expansion of the Universe. The second possibility is that w_Λ is itself evolving in time. In either case, the dark energy would not be the cosmological constant Λ (in fact not even constant), but some new and as yet unexplained field or particle. A final possibility is that our theoretical understanding of gravity is incomplete on the largest scales and that GR needs to be modified. Although several models have been proposed, none yet have been able to fit observations on all scales ranging from the CMB, to galaxies, to the solar system.

Without a firm theoretical understanding in place and without a direct detection in the near future, better characterization of the dark energy is necessary to distinguish among the above possibilities. Characterization of dark energy requires a more precise understanding of the expansion history of Universe. Evolution of the distances between unbound astronomical objects is directly related to the expansion history

and can be studied by recession velocity measurements to distant objects similar to Hubble's early studies. Dark energy could also be characterized by understanding the evolution of the Universe's matter density or by studying the growth of large-scale structure in the Universe. Accelerated expansion affects structure growth by altering how early in the Universe's history overdensities collapsed via gravitational potential wells, leading to structure formation. The expansion history and its effects are measurable through several methods [Albrecht et al., 2006], including: improved observations of Type 1a supernovae as standard candles, weak gravitational lensing of galaxies, measures of the galaxy correlation function to study the evolution of the baryonic acoustic oscillations since the time of the CMB, and counts of the number of clusters of galaxies. ACT will use galaxy-cluster counts as a probe of the formation and evolution of structure which in turn will be used to characterize the dark energy.

1.4 Galaxy Clusters as Cosmological Probes

Number counts of galaxy clusters are a potentially powerful way of exploring the expansion history of the Universe, and in turn, constraining dark energy. Galaxy clusters are the largest known scales in the Universe for which gravitational collapse has become non-linear. Galaxy clusters form in deep gravitational potential wells, with densities high enough to ionize hydrogen. The heated hydrogen gas forms an intracluster medium with gas temperatures of approximately 10^7–10^8 K. The high temperature of the gas is a distinctive characteristic of the intracluster medium and is important because it provides a signature at X-ray energies and shifts the energy of CMB photons in a distinctive manner. Clusters are interesting because their formation rate depends strongly on the cosmological parameters. Cluster counts above

some minimum mass are sensitive to the equation of state of the dark energy [Barbosa et al., 1998]. The left plot of Figure 1.3 shows the predicted number of clusters above 5 x 10^{14} M_{Sun} for a redshift range of 0.25–5 in cosmological model simulations where the dark-energy equation of state is varied. The dependance on w_Λ comes from the fact that the dark energy field dominates over the matter density at increasingly earlier times for larger values of w_Λ. Early domination of dark energy increases the expansion rate and suppresses structure formation resulting in fewer clusters. The number density of clusters as a function of redshift is an even more sensitive probe of cosmological models. The number of clusters above some minimum mass falls exponentially with redshift, and is strongly dependent on the cosmological model [Press and Schechter, 1974, Bond et al., 1991, Holder et al., 2001, Wang et al., 2004, Lima and Hu, 2005]. The right-hand side of Figure 1.3 shows this exponential dependence with varying w_Λ and Ω_m.

Extracting cosmological parameters from cluster measurements relies on having a complete, unbiased sample of clusters above some minimum mass out to high redshift. Most high-redshift clusters to date have been found from their thermal Bremsstrahlung radiation emitted in the X-ray spectrum. The X-ray surface brightness decreases with redshift $\propto \frac{1}{1+z^3}$. Measurements of high-redshift clusters require deep integration. With current X-ray satellites, blind, unbiased, wide-field surveys of the sky to detect clusters at large redshift are infeasible.

1.4.1 Sunyaev-Zel'dovich effects

The thermal Sunyaev-Zel'dovich (tSZ) effect is the inverse-Compton scattering of CMB photons by hot electrons as they pass through the hot intracluster gas in clusters

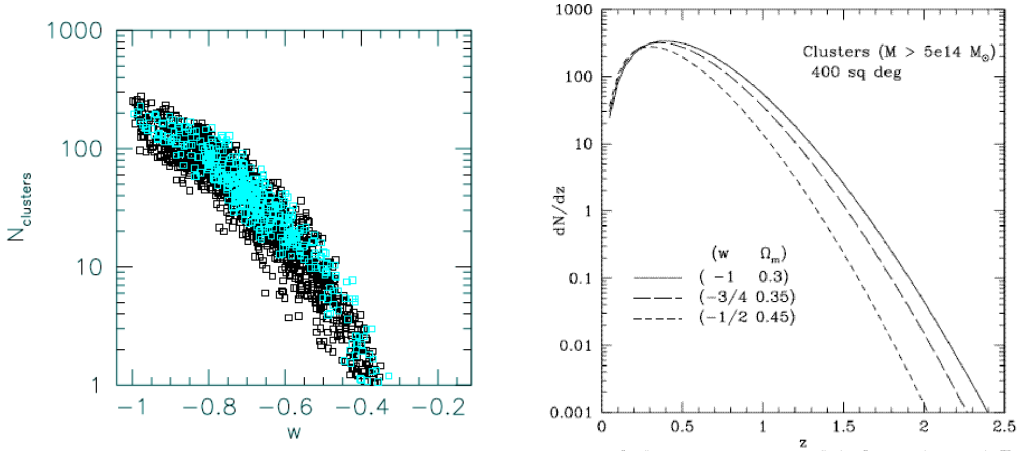

Figure 1.3 The expected number of galaxy clusters above 5×10^{14} M_{sun} with varying cosmological parameters. *Left*: Simulation showing the expected total number of clusters above 5×10^{14} M_{sun} between redshift of 0.25–5 for 1000 indistinguishable cosmological models with WMAP 1 year data. The total number of clusters depends on the cosmological parameters. The expected number of clusters varies depending on the value of the dark energy equation of state (w). Figure from D. Spergel and the ACT proposal. *Right*: Expected number of clusters above 5×10^{14} M_{sun} as a function of redshift for 3 cosmological models in a 400 square-degree survey. The number of clusters as a function of redshift is highly sensitive to the cosmological parameters. Estimating w requires an unbiased cluster survey out to high redshift. Figure from C.P. Ma and the ACT proposal.

of galaxies, causing a net increase in the photon energy [Sunyaev and Zeldovich, 1972]. Even in the most massive clusters, only $\approx 1\%$ of CMB photons are expected to be scattered, so the spectral distortion to the CMB will be small [Carlstrom et al., 2002]. The size of the distortion is proportional to the Compton y-parameter, which is a measure of the pressure along the line of site, given by

$$y = \frac{\sigma_T}{m_e c^2} \int n_e k_b T_e dl = \frac{\sigma_T}{m_e c^2} \int p_e dl, \tag{1.9}$$

where σ_T is the Thompson cross section, n_e is the electron number density, $m_e c^2$ is the electron rest mass, k_B is the Boltsmann constant, T_e is the electron temperature, and p_e the electron pressure. Since the net photon number is conserved, the effect of this distortion is to decrease the number of photons at lower frequencies and increase the number at higher frequencies. The cross over or "null" point between the distorted and undistorted CMB blackbody is at approximately 218 GHz (see Figure 1.4). The spectral dependence of the tSZ is given by[5]

$$f(x) = x\frac{e^x + 1}{e^x - 1} - 4, \tag{1.10}$$

where $x \equiv \frac{h\nu}{k_B T_{CMB}}$, h is Planck's constant, ν is the frequency, T_{CMB} is the CMB blackbody temperature. The fractional temperature difference caused by the tSZ is then given by combining Equations 1.9 and 1.10:

$$\frac{\Delta T_{CMB}}{T_{CMB}} = f(x)y. \tag{1.11}$$

[5]This assumes non-relativistic electrons. For relativistic corrections, an additional $(1 + \delta(x, T_e))$ term should be added. See Itoh et al. [1998].

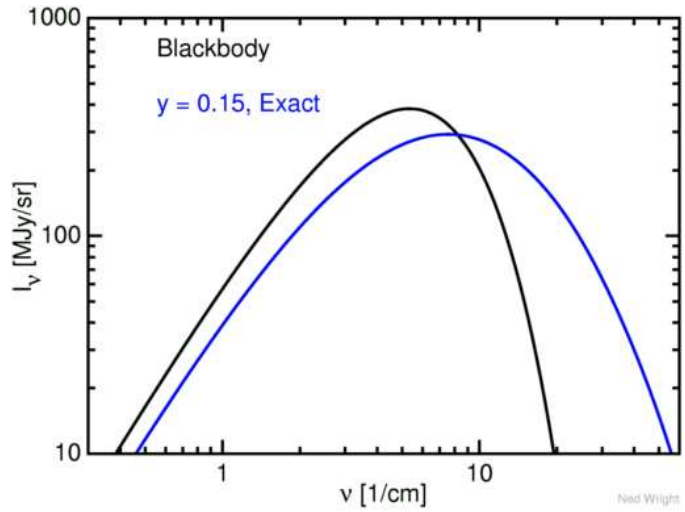

Figure 1.4 The spectral shift of the CMB caused by the tSZ effect. The undistorted thermal CMB blackbody spectrum is shown as the black line, and the tSZ distorted CMB spectrum is the blue line. A Compton-y parameter of 0.15 was used in the calculation to enhance the size of the effect for illustrative purposes. This is approximately 1000 times more massive than a typical cluster. The tSZ shifts CMB photons to slightly higher temperatures. The cross over point is at a frequency of $\approx 218\,\mathrm{GHz}$. Figure by N. Wright.

There are several features that make searches for galaxy clusters using the tSZ appealing. The amplitude of the signal is proportional to the temperature and density of the cluster gas, and independent of the redshift of the cluster. The relative amplitudes of the tSZ and CMB are independent of distance (see Equation 1.11) because both the background CMB and tSZ-induced distortion are redshifted together after the scattering takes place. The tSZ has a characteristic spectral shape: a temperature decrement, a null and an increment compared to a (CMB or any other) blackbody spectral energy distribution (SED) that allows one to distinguish clusters from other thermal sources (see Figure 1.7). This spectral shape is independent of cluster redshift. Because of these features, blind surveys may yield unbiased, mass-limited catalogues of the positions of the galaxy clusters on the sky.

Measurements of the tSZ effect are a potentially powerful tool for understanding

the properties of our Universe. However, these measurements present many challenges. Typical clusters will have a Compton y-parameter of 10^{-4}–10^{-5} and the expected signal is small; $\Delta T_{CMB} \lesssim 500\,\mu\text{K}$ (see Figure 1.5). The typical size of the clusters will be on order of a megaparsec and the angular diameter of most clusters will be $\lesssim$ a few arcminutes at most redshifts [Carlstrom et al., 2002]. Large diameter single-dish telescopes or interferometers are required to achieve this angular resolution, preventing space-based observations. Ground-based telescopes are limited to observations at frequency windows were atmospheric attenuation is low. They are also subject to atmospheric noise caused by variations in the emission of the atmosphere. Furthermore, the data will be contaminated from sources such as radio point sources and dusty submillimeter galaxies. A measure of the tSZ flux alone is not sufficient to determine important cluster properties such as mass and temperature, and provides no information on redshift. Follow-up observations at multiple wavelength bands, from optical to X-ray, can help to determine these parameters as they probe different cluster properties (see Section 1.5). However, clusters are collapsed objects that are described by complicated, nonlinear processes. Interpreting tSZ data will likely require a better understanding of cluster physics.

If the cluster has a peculiar velocity relative to the CMB rest frame, the scattered CMB photons will be Doppler shifted, changing the effective temperature of the radiation. This effect is known as the kinetic SZ (kSZ). Unlike the tSZ, the kSZ has the same thermal spectrum (in the rest frame of the cluster) as the CMB. Additionally, the size of the kSZ will typically be an order of magnitude lower than the tSZ, except in the null region (see Figure 1.5). However, multifrequency observations at and around the null, with sufficient sensitivity, should be able to separate the kSZ from primary CMB. If measurable, the cross correlation of the kSZ signal and the kSZ-

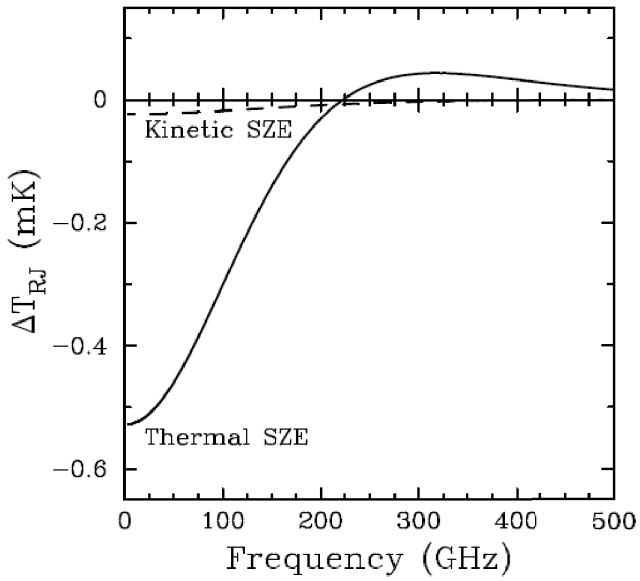

Figure 1.5 Temperature distortion to the CMB from SZ effects. The solid line is the distorthion from the tSZ effect and the dashed line is from the kSZ effect. The cluster properties used to calculate the spectra are a Compton y-parameter of 1×10^{-4}, an electron temperature of 10 keV, and a cluster peculiar velocity of 500 km/s. Figure from Carlstrom et al. [2002].

tSZ ratio can be used to constrain the evolution of the dark-energy equation of state [Hernandez-Monteagudo et al., 2006].

Early work to detect the tSZ effect focused on targeted observations of known clusters. The first reliable detections of the tSZ were made by radio telescopes operating at centimeter wavelengths (see e.g. Birkinshaw et al. [1991], Herbig et al. [1995], Myers et al. [1997], Mason et al. [2001]) and by radio interferometers (see e.g. Jones et al. [1993], Carlstrom et al. [1996, 2000], Reese et al. [2002]). To date, these experiments have measured tSZ decrements for tens of clusters (for a recent review see Carlstrom et al. [2002]). The first significant detections at millimeter wavelengths using bolometric detectors were made by the Sunyaev-Zel'dovich Infrared Experiment (SuZIE) instrument [Holzapfel et al., 1997] on the 12 m Caltech Submillimeter Observatory

(CSO). They measured the tSZ spectrum in three frequency bands centered at 145, 221, and 355 GHz. With 4 detectors at each band frequency, they have tSZ detections of 15 clusters [Benson et al., 2004]. Combining the data from these bands around the tSZ-null, they have separated the tSZ signal from the kSZ signal for 6 clusters, providing the first limits on the cluster peculiar velocity from a measure of the kSZ effect [Benson et al., 2003]. Recently, the 10 m South Pole Telescope (SPT) became the first experiment to find clusters in a blind survey from their tSZ signal. SPT simultaneously observes in three frequencies using an array of 960 bolometers spread between bands centered at 95, 150 and 225 GHz [Ruhl et al., 2004]. They report the detection of 3 previously unknown clusters in a 40 square-degree survey region [Staniszewski et al., 2008]. The clusters show signal decrements at 90 and 150 GHz with corresponding non-decrements at 225 GHz near the tSZ-null. The cluster detections were subsequently verified with optical images from the Blanco Cosmology Survey (BCS). This first blind detection is exciting as it demonstrates the potential for multifrequency observations at millimeter wavelengths to detect clusters from their tSZ spectral signature. Progress in the field has come from a combination of improved observing techniques employing specialized instruments, better control systematics, and the development of large arrays of detectors that allow for the mapping of large regions of sky to the required sensitivity.

1.5 The Atacama Cosmology Telescope Project

The strength of the current cosmological standard model comes from its ability to explain the results of several experiments. Similarly, dark-energy models of the Universe will be constrained best by combining the results of several different types of

experiments, as each will probe the expansion history slightly differently. The work presented here describes one such experiment designed to measure both the growth of structure and the evolution of matter density. The goal is to probe the nature of dark energy and better constrain cosmological parameters by measuring the anisotropy to high l the CMB over a wide field (~ 500 deg^2) with better sensitivity ($\sim 15\,\mu$K/map pixel) and resolution (~ 1 arcminute) than has previously been achieved [Kosowsky, 2003].

The Atacama Cosmology Telescope (ACT) is a 6-meter diameter telescope designed to make detailed measurements at millimeter wavelengths with arcminute resolution. The construction of the ACT was completed in the summer of 2007. The telescope is located at an altitude of 5,190 meters in Atacama desert in the Chilean Andes. The receiver for ACT is the Millimeter Bolometer Array Camera (MBAC). MBAC and ACT were designed in tandem to make detailed measurements of the CMB temperature anisotropy at angular scales from a few degrees to approximately one arcminute, corresponding to multipole ranges of $100 \lesssim l \lesssim 10{,}000$. An expected CMB power spectrum for MBAC on ACT is shown in Figure 1.6. The large spatial coverage at arcminute resolution will allow ACT to measure directly the transition from the linear to non-linear regime, probing both the primordial anisotropies at low l and secondary anisotropies at high l.

MBAC simultaneously observes in three frequency bands at 145 GHz, 220 GHz and 280 GHz, with bandwidths of approximately 20 GHz for each frequency. Each array consists of 1024-pixel array of Transition Edge Sensor (TES) bolometers. These frequency bands were chosen to probe the decrement, null, and increment of the tSZ signal and to minimize atmospheric foregrounds at the high-altitude site. Choosing the frequencies in this way allows for better separation of the galaxy clusters from

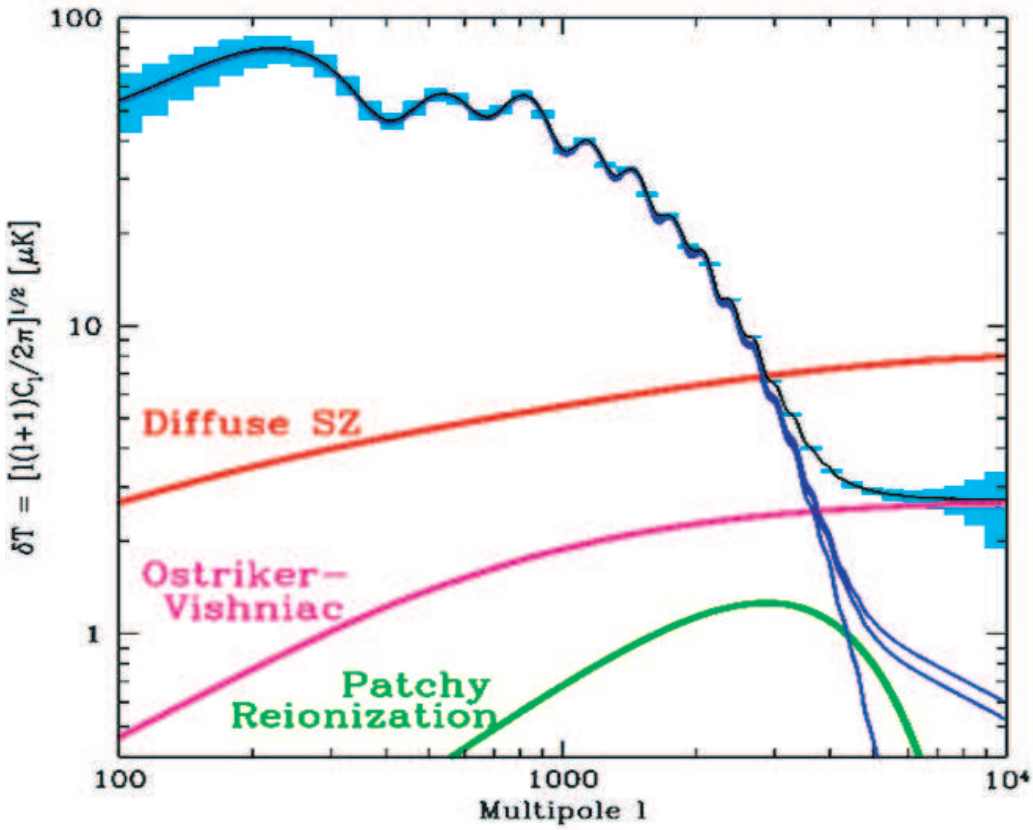

Figure 1.6 The prior-to-construction anticipated CMB power spectrum with errors for the MBAC receiver on ACT. The figure is based on a simulation assuming a 100 square-degree CMB map cleaned of foregrounds by combining the maps at 145, 220, and 280 GHz. The simulation assumes a map sensitivity of $\sim 2\,\mu$K per map pixel. However, the current plan for ACT is to map 500 square-degrees to a sensitivity of $\sim 15\,\mu$K per map pixel. The decreased sensitivity limit is partly due to the larger sky coverage and partly to larger-than-anticipated detector noise. The increase is partially offset by a longer planned observation period (the figure assumes 30 high-quality nights while we are planning $\sim$ 200 nights over two seasons). The lower sensitivity will cause the expected error bars to grow. Despite being out-of-date, this figure shows the approximate angular scales and multipole coverage that MBAC on ACT will measure. ACT will probe both the primary CMB anisotropy at low l and the secondary anisotropies at high l. Figure from M. Devlin, M. Tegmark, and the ACT proposal.

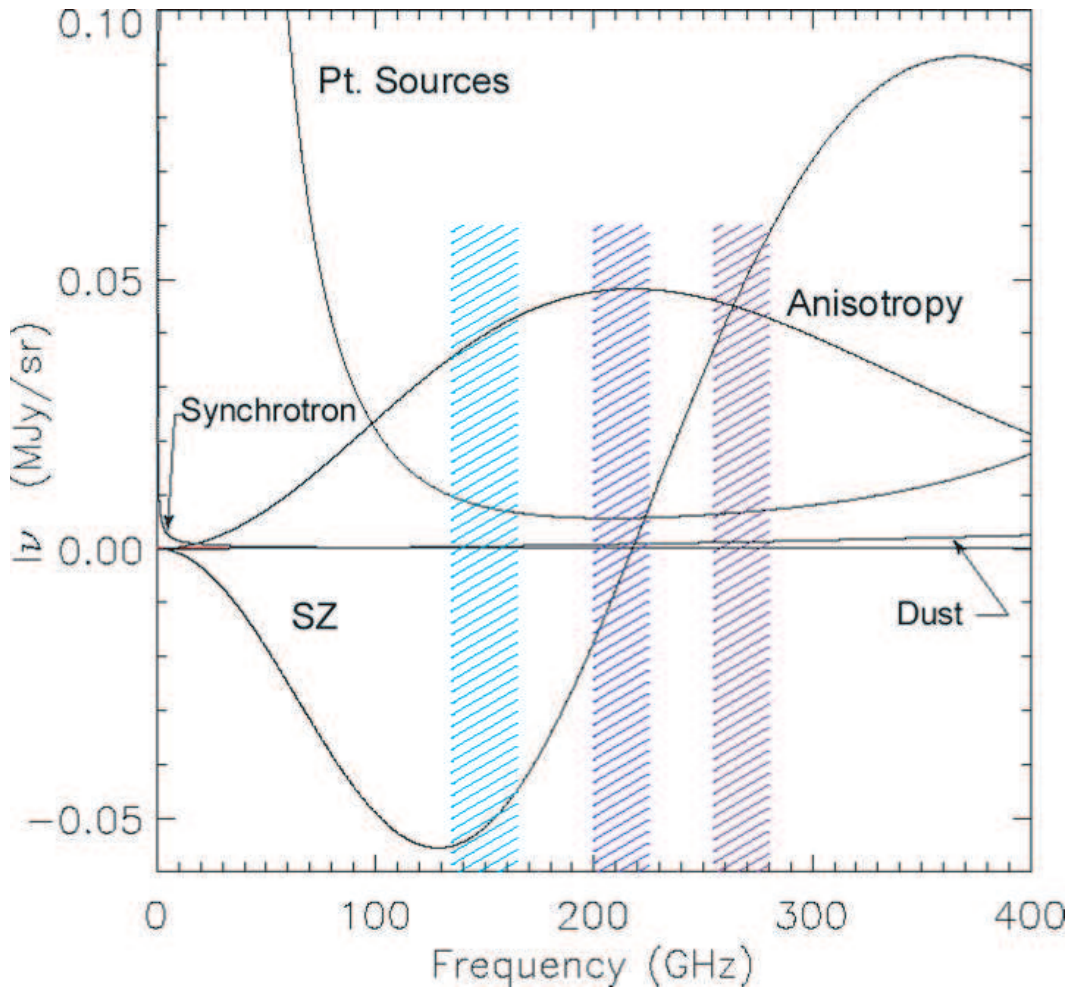

Figure 1.7 Plot of the fluctuation spectrum of the mm-wave sky around the ACT spectral bands. Here the plot has been normalized by the CMB blackbody curve. The CMB anisotropy is given as $(\delta B_\nu/\delta T)\delta T$ with $\delta T = 100\,\mu K$. A Compton y = 5 $\times 10^{-5}$ was used for the tSZ effect, typical for a cluster. The ACT observing frequency bands are overplotted as colored hatched regions. They probe the decrement (145 GHz – shown in teal), null (220 GHz — shown in blue), and increment (280 GHz — shown in purple) of the tSZ. The central band will see minimal tSZ contribution, mainly CMB and point sources. The fluctuation levels for diffuse free-free, synchrotron, and dust emission are for a Galactic latitude of b = 20° and l = 1000 [Tegmark et al., 2000, De Oliveira-Costa et al., 2002]. The CMB anisotropy, point sources, and tSZ effects are separable by their frequency signatures. Figure from M. Devlin, L. Page, and M. Tegmark

primary CMB anisotropy and other foreground contamination such as point sources (Figure 1.7). For a given detector sensitivity, a trade-off is required between map depth (which sets the minimum cluster mass detectable) and survey area (the more sky coverage, the more potential clusters). Figure 1.8 shows the expected number of clusters for two simulations as a function of cluster mass and survey area. A deep survey gives many more lower-mass cluster detections, but a wide survey is advantageous for finding the rarer, massive clusters at high redshift ($z \gtrsim 1$) which are important because their number is especially sensitive to cosmological parameters (Figure 1.3). For ACT, the expected map sensitivity of $\sim 15\,\mu\mathrm{K}$ per map pixel corresponds to to a detectable cluster mass-limit of approximately 4.5–$5 \times 10^{14}\,\mathrm{M}_{sun}$ [Sehgal, 2008]. With a 500 square-degree survey at this depth, we expect to detect ~ 100 galaxy clusters (Figure 1.8). From the tSZ-detected clusters in our maps, we will produce a mass-limited galaxy-cluster catalog [Sehgal et al., 2007].

To fully exploit the ability of the galaxy-cluster catalog to constrain cosmology, the redshifts and masses of the clusters must be known. The ACT collaboration is pursuing a program of follow-up observations in the optical and X-ray of the tSZ-selected clusters to determine their masses, redshifts, and temperatures. Spectroscopic and photometric measurements in the optical can be used to determine the redshift. Furthermore, if multiple galaxy members are observed with sufficient resolution and precision, the cluster's velocity dispersion can be determined. The velocity dispersion is proportional to the mass of the cluster.[6] Thermal Bremsstrahlung X-ray emission from the cluster is $\propto n_e^2 T_e^{1/2}$, where n_e is the electron density and T_e is the gas temperature. Recall that the tSZ signal is $\propto n_e T_e$ (Equation 1.9). Because

[6]Mass estimates determined from velocity dispersion measurements depend on the cluster-mass profile assumed. For clusters with similar mass profiles, relative masses can be determined.

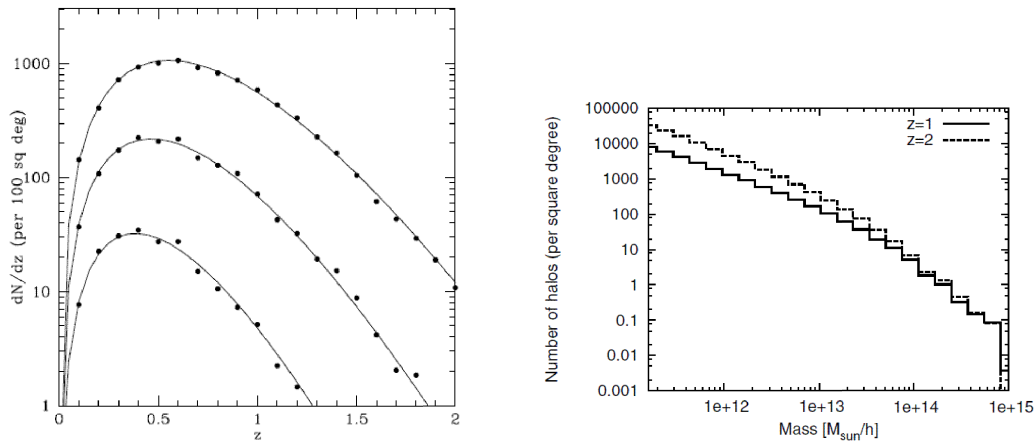

Figure 1.8 Two simulations showing the expected number of clusters as a function of cluster mass and survey area. *Left*: The expected number of clusters above some minimum mass as a function of redshift for a 100 square-degree region of sky. The three sets of lines, from top to bottom, correspond to minimum masses $M_{min} = (1, 2, 4) \times 10^{14}\, M_{Sun}/h$. Figure from Sehgal et al. [2007]. *Right*: The expected number of clusters as a function of cluster mass in a square-degree. The solid and dashed lines show all clusters above z = 1 and z = 2, respectively. Figure from Pace et al. [2008].

the two measurements probe the gas density and temperature differently, combining tSZ observations with X-ray flux measurements potentially allows for the separation of the two components, providing an estimate of the cluster mass.[7] Alternatively, measurements of the weak gravitational lensing of background galaxies by the cluster can be used to determine the total cluster mass. The above discussion shows the importance of combining observations at multiple wavelengths to probe different cluster properties, and hence determine the masses, temperatures, and redshifts. The cluster density as a function of redshift will help map out the growth of structure in the Universe, which in turn will constrain the dark-energy equation of state (Figure 1.3).

The MBAC was deployed to the ACT site in September 2007. For this first observ-

[7]One approach would be to assume a standard cluster morphology and simultaneously solve for the electron density and temperature from the tSZ and X-ray measurements. Another method is to use the X-ray luminosity to temperature relationship to determine the cluster gas temperature from the X-ray signal alone; the tSZ signal could then be used to determine the mass [Arnaud and Evrard, 1999].

ing season, it was outfitted with the 145 GHz array. Science observations began on 15 November 2007 and continued to 14 December 2007. The camera was brought back to North America in January 2008 at the onset of the Bolivian winter. The two other arrays were subsequently installed at Penn. After testing at Penn was completed, a fully populated MBAC was redeployed for a second observing season in August 2008, and completed a second observing season with simultaneous observations at three frequencies of 145, 220 and 280 GHz, ending in December 2008. Data analysis from the first and second observing seasons are underway and we are preparing for a third observing season to begin in May of 2009.

Chapter 2

The Atacama Cosmology Telescope

The Atacama Cosmology Telescope is designed to make detailed measurements at millimeter wavelengths on scales from a degree to an arcminute. To meet the science goals discussed in Chapter 1, a custom designed telescope with dedicated observations was required. A 6-meter dish enables arcminute resolution for diffraction-limited optics through the ACT bands which probe the null of the tSZ spectrum (at 220 GHz). Large arrays of detectors are necessary to map 500 square-degrees of sky to the required sensitivity of 10 µK per map pixel in a timely manner. These large arrays in turn require a large focal plane. The telescope is designed to work in conjunction with MBAC (described in Chapter 3), but also be as generic as possible for upgrades with future receivers. In this chapter I present the overall design and architecture of the telescope. I discuss the alignment of the mirrors and how alignment affects telescope gain. Finally, I discuss the telescope's location and scan strategy, both chosen for optimized observations with minimal systematic effects for CMB ground observations.

2.1 Telescope Overview

The telescope consists of a two reflector system: a 6-meter primary mirror and a 2-meter secondary mirror. The diffraction-limited beam is approximately 0.8 arcminutes at 280 GHz. The mirrors are arranged in an off-axis configuration to give an unobstructed image of the sky. The telescope's mechanical structure was designed and built by Empire Dynamic Structures Ltd.[1] and assembled in Port Coquitlam, British Columbia in 2006 prior to shipping to Chile. Figure 2.1 shows the major components of the telescope and Table 2.1 lists the important parameters. The telescope consists of an approximately 40 metric ton movable upper structure which sits atop a 12 metric ton base pedestal. The telescope is movable in both azimuth and elevation. The primary focal length was fixed to $\approx 5\,\mathrm{m}$, which allowed for a compact arrangement of the primary and secondary mirrors. A compact design allows for a more rigid structure and reduces the angular momentum during azimuthal scanning (discussed in Section 2.4), thereby reducing manufacturing and engineering costs. To minimize ground pick-up during scanning, the telescope has two ground screens. A large, stationary outer ground screen surrounds the telescope and a second, inner ground screen connects the open sides of the primary mirror to the secondary mirror, and moves with the telescope during scanning. A climate-controlled receiver cabin is situated underneath and between the primary and secondary mirrors and is part of the upper structure (Figure 2.2).

The two mirrors are arranged in an off-axis Gregorian configuration. Using the Gregorian design as a starting point, the mirror shapes were numerically optimized using Code V optical design software[2] to give the best mean image quality over a

[1]Formerly AMEC Dynamic Structures. Business address: 1515 Kingsway Ave., Port Coquitlam BC V3C 1S2, Canada. Internet URL: http://www.dynamicstuctureslt d.com.

[2]Business address: Optical Research Associates, 3280 East Foothill Blvd., Pasadena, CA, 91107.

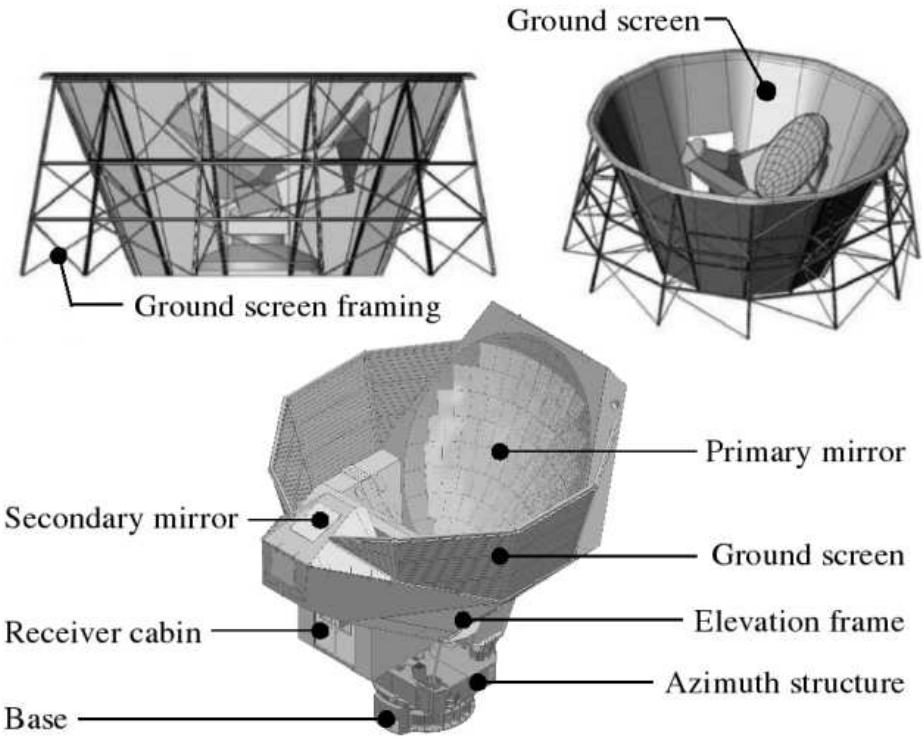

Figure 2.1 Mechanical rendering of ACT and its ground screens. The telescope has a low profile; the full height is 12 m. The entire upper structure ("Azimuth structure" and above) rotates as a unit. The surrounding outer ground screen completely shields the telescope from ground emission. The screen also acts as a weather shield. An inner ground screen mounted on the telescope connects the sides of the secondary and primary. The primary mirror is 6 m in surrounded by a 0.5 m guard ring (. Figures courtesy of AMEC Dynamic Structures.

square-degree field (for details of the exact numerical optimization and mirror formulae see Fowler et al. [2007]). The final shapes of both mirrors are ellipsoidal. The image quality was assessed using the Strehl ratio S, the ratio of the peak intensity of a point spread function over the theoretical maximum peak of a diffraction-limited mirror of the same diameter. Strehl ratios were estimated by calculating the rms path deviation, σ, for a large number of rays at wavelength λ and taking $\ln S \approx -(2\pi\sigma/\lambda)^2$ [Born and Wolf, 1999]. At the Gregorian focus before reimaging (Section 3.1), the telescope achieves a Strehl ratio greater than 0.9 over a 1 square-degree field at 280 GHz.

Internet URL: http://www.opticalres.com/.

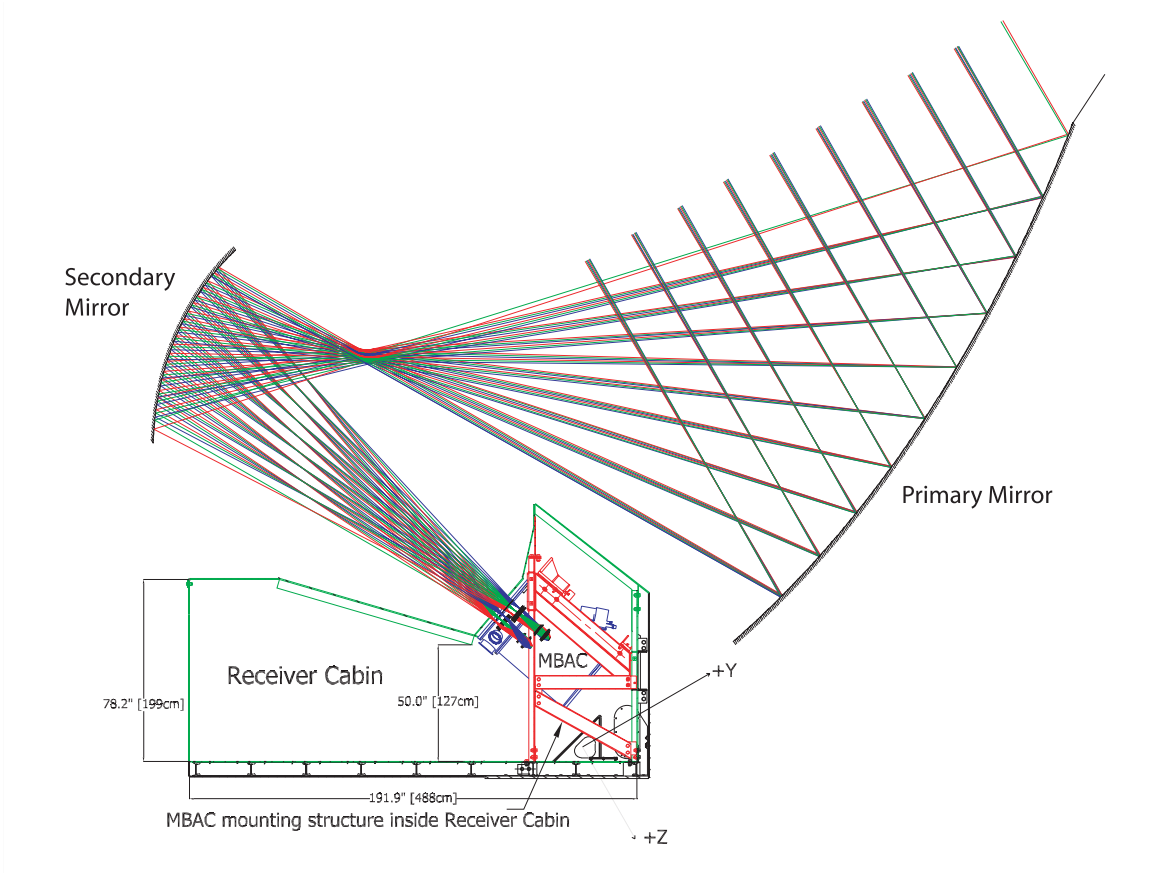

Figure 2.2 Ray trace of ACT's primary and secondary mirrors. The telescope is an off-axis numerically optimized Gregorian. The rays are traced into the MBAC cryostat, mounted on the far right of the receiver cabin. The service position (position where the receiver-cabin floor is level) is shown, corresponding to a viewing elevation of 60°. The normal observing elevation is 50.5°. The rays are traced for the highest (blue), central (green), and lowest (red) fields in the 280 GHz camera (higher in the cryostat) and the 220 GHz camera (lower in the cryostat). The figure also shows the dimensions and location of the receiver cabin and MBAC mounting structure.

Telescope Properties		**Location**	
Telescope height	12 m	Altitude	5190 m
Ground screen height	13 m	Longitude	67°47′15″W
Total mass	52 t	Latitude	22°57′31″S
Mass of moving structure	40 t		
Optics		**Motion**	
Focal ratio at focus	2.5	Azimuth range	−220° – +220°
Field of view at focus	1 sq-deg	Max. azimuth speed	2°/s
Primary mirror diameter	6 m	Max. azimuth acc.	10°/s^2
No. of primary panels	71	Elevation range	30.5° – 60°
Secondary mirror diameter	2 m	Max. elevation speed	0.2°/s
No. of secondary panels	11		

Table 2.1 Important telescope parameters.

The telescope approaches an aplanatic system with no leading-order spherical aberrations or coma in the focal plane [Schroeder, 2000]. Figure 2.2 shows side-view ray traces for the primary and secondary mirrors. The focal ratio, F $= f/D$, where f is the focal length and D the illuminated primary mirror diameter, of the Gregorian is 2.5. This relatively fast focus minimizes the size of the MBAC window (see Section 3.1.1).

To minimize the beam sizes and maximize the collecting area, a large fraction of the primary mirror is illuminated ($\approx 5.8\,$m). Diffraction at the cold pupil stop (inside MBAC, discussed in Section 3.1) can load the detectors with radiation emitted from warm, nearby structures. To combat this, each mirror is surrounded by a reflective aluminum ring. These rings effectively increase the area beyond the geometric diameter of the mirror that is at the sky temperature, thereby reducing the amount of warm, stray radiation from reaching the detectors.

2.2 Mirror Alignment

The telescope's 6-meter primary and 2-meter secondary mirrors are composed of individually machined aluminum panels mounted to back-up structures (BUS). The primary consists of 71 roughly rectangular panels, laid out in eight rows; the panels comprising each row are identical, but the curvature of the panels decreases with increasing height of the BUS (Figure 2.3). An individual panel measures $\approx 0.65 \times 0.85\,\mathrm{m}$ and weighs 10 kg. The secondary mirror is assembled by arranging 10 trapezoidal panels, measuring $\approx 0.35 \times 0.80\,\mathrm{m}$, around a $\approx 0.50 \times 0.80\,\mathrm{m}$ decagonal-shaped central panel (Figure 2.4). The panels, manufactured by Forcier Machine Design[3], were individually cast and machined to their required surface shape. The panels were measured using a coordinate-measuring machine (CMM) to have an rms deviation from the expected shape of $\lesssim 3\,\mu\mathrm{m}$.

The panels are attached to the BUS at their four corners approximately 6 cm from the corner edge. The connecting mechanisms allow for coarse and fine adjustment of the panel position by adjusting the distance between the BUS and panel mount points. Adjustment is achieved by manually turning two screws on the connector which are accessible from the back side of the BUS. The surface rms of the mirror, which is dominated by the relative panel alignment, affects the forward gain, G, of the telescope, defined as

$$G = \frac{4\pi}{\Omega_A} \quad ; \qquad \Omega_A = \int_0^{2\pi} \int_0^{\pi} P_n(\theta, \phi)\, \sin\theta \, d\theta \, d\phi, \tag{2.1}$$

where Ω_A is the beam solid angle and P_n is the normalized antenna power [Rohlfs and Wilson, 1996]. We can approximate the loss in forward gain from panel misalignment

[3]Business address: 123 Marshall Ave, Petaluma, CA 04052, USA.

using the Ruze formula [Ruze, 1966],

$$G = G_0 \exp\left[-\left(4\pi\sigma/\lambda\right)^2\right], \tag{2.2}$$

where G_0 is the forward gain for an ideal antenna, σ is the mirror surface rms, and λ is the observing wavelength. This formula is only marginally applicable because each panel represents 1/71 of the total primary surface area, a comparatively large percentage of the the mirror. However, we can use Equation 2.2 as a guide to assess how accurately the panels must be aligned. To recover $\approx 90\,\%$ of the optimal forward gain at our highest frequency of 280 GHz, a surface rms of $\approx 27\,\mu$m is required.

The panel positions are measured using a laser tracker manufactured by Faro[4]. The tracker measures the time of flight of a laser pulse to determine the distance to a point on the mirror's surface. The actual measurement is made by holding a reflecting corner-cube mounted in a 1.5" (38.1 mm) diameter precision steel sphere (spherically-mounted retroreflector SMR) centered with an accuracy of ±0.0001" (2.5 µm) against the surface of the panel mirror. The tracker is mounted as needed to a 3.5" (88.9 mm) threaded flange permanently mounted on the telescope's structure between the primary and secondary mirrors. A set of permanently mounted fiducial reflectors are located on the boundaries of both the primary and secondary mirrors. These fixed points are used to determine the position of the laser tracker in the coordinate system of the telescope and allow the laser tracker to regain the telescope's reference frame. Eight measurements (two in each of the four corners) are made on each panel by holding the reflector to the mirror segment. This produces a 3-dimensional shape of the primary and secondary mirrors. The residuals are least-

[4]Internet URL: http://www.faro.com.

squares fit to the functional form of the mirror to calculate the individual panel corrections. The panel adjustments are then made, and the process is repeated. In this way, the mirrors are iteratively brought into alignment.

The panels must be measured at night because of large telescope deformations during the day caused by solar heating of the primary BUS and elevation structure [Hincks et al., 2008]. During the course of the night-time measurement, small ambient temperature changes can induce a flexing of the telescope structure that causes the primary to shift relative to the position of the secondary (and laser tracker) by about 100 µm, but which does not seriously affect the relative positions of the panels in the primary relative to one another. To account for this temperature drift, the fiducial points are measured in between every six panel measurements, and allow for the temperature-dependant repositioning of the panels to be taken out. The measurement of 8 points on 6 panels requires about 25 minutes. A complete set (about 570 individual measurements of panels, and 12 measurements of fiducials) of panel measurements takes about 6 hours.

The panel alignment was completed October 2007 prior to beginning the 2007 observing season. A mirror surface rms of 31 µm was achieved for the primary and 10 µm for the secondary. The alignment has since been rechecked several times with small panel corrections made to improve the rms further. The first recheck was done in January 2008 after the completion of the first season to test for creep in the panel alignment. Both the primary and secondary mirrors were measured to have an rms of 35 µm. After the panel creep was determined, the panels were realigned to 31 µm and 12 µm for the primary and secondary, respectively. A second check for panel creep was performed in June 2008, 6 months after the previous adjustments, and prior to the beginning of the 2008 observing season. This time, the primary mirror was

found to have a surface rms of 35 µm and secondary a surface rms of 12 µm. It is not understood why the secondary changed so dramatically during the first year; perhaps it was erroneously set initially. Slight adjustments were made, and the primary panels were repositioned to 25 µm prior to the 2008 observing season; the secondary was left at 12 µm. A final check was done at the end of the this past observing season. The panels were found with the primary at 27 µm and secondary at 12 µm. These repeated measurements indicate that the panels are holding their relative positions and consequently the mirror's surface to within the required tolerance, with only minor adjustments required every ~ 6 months. Figures 2.3 and 2.4 show the alignment results obtained prior to the 2008 observing season.

After the panels have been set, the position of the secondary can be adjusted as a unit using linear actuators mounted on the secondary frame and controllable remotely by software using the telescope's main control program. The adjusters allow ± 1 cm motion in y and z, and rotations of $\pm 1°$ in azimuth and elevation. These actuators are used to focus the system by peaking up the detector response to planets. Adjustments were made after the installation of MBAC, and can, in principle, be used to correct for telescope deformation at different observing elevations. So far we have not found it necessary to correct for elevation deformation, primarily because our scientific observations have been made almost exclusively with the telescope observing at 50.5°.

2.3 Site Location and Logistics

The telescope is located in the Atacama Desert in the northern Chilean Andes. The site is at an altitude of 5190 m near the peak of Cerro Toco overlooking the

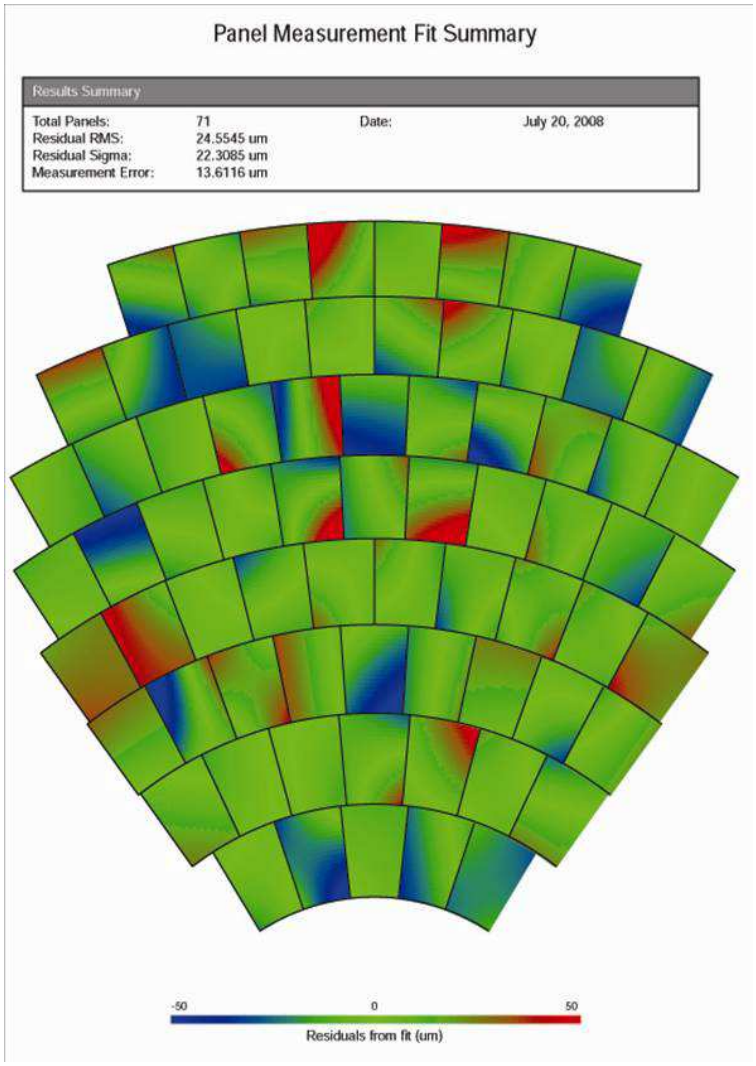

Figure 2.3 Primary mirror layout and final mirror alignment. The primary is composed of 71 approximately rectangular panels arranged in eight rows. The panels are attached to the telescope BUS and are aligned using four adjustment screws on the panel back-side. Panel positions are measured using a laser tracker. The residuals of a fit to the mirror's equation give the necessary adjustments. The figure shows the residual after the final adjustments for the 2008 observing season were made. The mirror was aligned to better than 25 µm. Figure courtesy of R. Dünner.

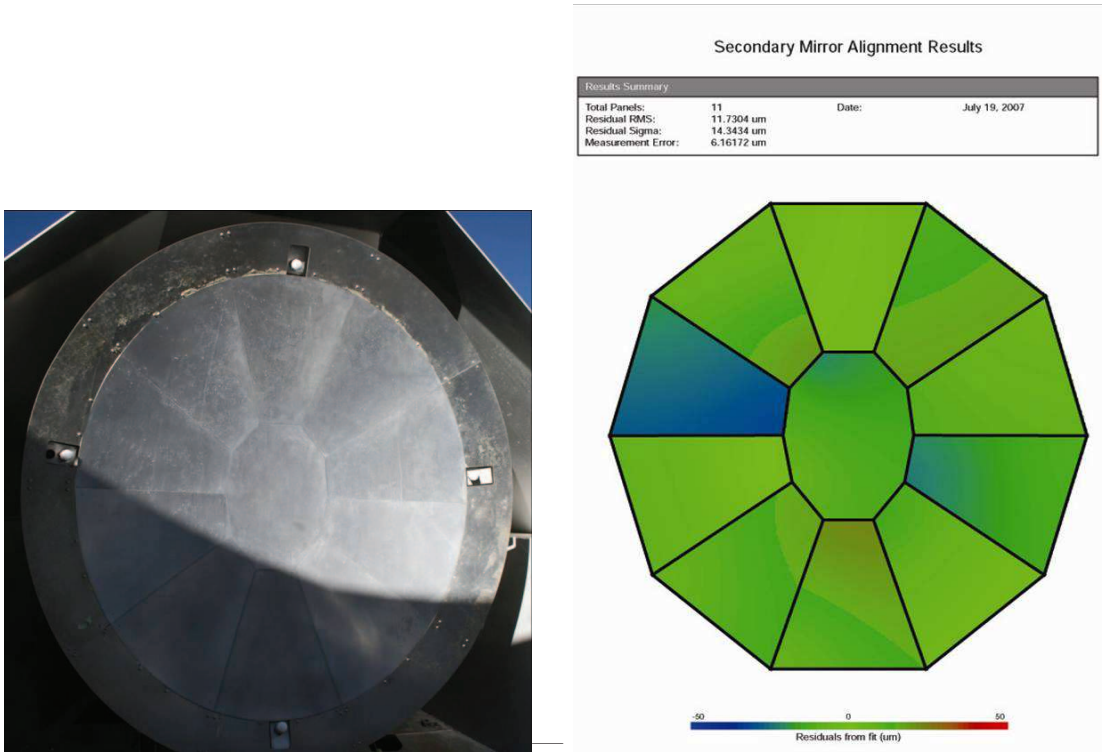

Figure 2.4 *Left* : Picture of the secondary mirror. The secondary is composed of 10 trapezoidal sections of a concave ellipsoid positioned around a central panel in a petal configuration. An aluminum ring (Δ R $\sim$ 200 mm) surrounds the mirror, increasing the effective size of the mirror at the sky temperature, and thereby reducing stray loading onto the detectors. Fixed fiducial points (in a cross pattern in the ring) are used to remove temperature dependent alignment drifts during panel measurements. Photo courtesy of M. Devlin. *Right* : Alignment of the secondary mirror. The panels are attached to a frame and are aligned using four adjustment screws accessible from the front of the panel. Panel positions are measured using a laser tracker. The residuals of a fit to the mirror's equation give the necessary adjustments. The mirror was aligned to better than 12 µm before the start of the 2007 observing season. Figure courtesy of R. Dünner.

Chajnantor plain. The Chajnanotor plain is the home to several millimeter-wave experiments, including the Llano Chajnantor Observatory (formerly home to the Cosmic Background Imager (CBI) and currently hosting the Q/U Imagining ExperimenT (QUIET)), the Atacama Pathfinder Experiment (APEX), and the Atacama Large Millimeter Array (ALMA). The specific ACT site has also been used by the TOCO and Millimeter INTerferometer (MINT) telescopes.

The extreme location is chosen because of the its millimeter and submillimeter atmospheric transparency due to its low precipitable water vapor (PWV) and high elevation. The intensity $I(\nu)$ of a cosmic signal is attenuated by the atmosphere according to

$$I_{Trans}(\nu) = I(\nu) \exp(-\tau A), \tag{2.3}$$

where τ is the opacity (or optical depth), A is the airmass[5], and I_{Trans} is the transmitted intensity. The atmosphere radiates as a gray body according to

$$I_{atm}(\nu) = B(\nu, T_{atm})(1 - \exp(-\tau A)), \tag{2.4}$$

where $B(\nu, T_{atm})$ is the blackbody intensity with atmospheric effective temperature T_{atm}). The National Radio Astronomical Observatory (NRAO) in collaboration with the European Southern Observatory (ESO) have been monitoring the opacity in the Chajnantor plain as part of the site evaluation for the ALMA project [Radford et al., 2001, Radford, 2002]. They use a "tipping" radiometer operating at 225 GHz to measure $I_{atm}(225\,GHz)$ through different airmasses and Equation 2.4 as a model

[5]It is common to assume a horizontally stratified atmosphere and ignore the curvature of the earth. In that case, the airmass is given as $A = \sec z$, where z is the zenith angle.

to estimate τ. Using the NRAO/ESO data and an atmospheric modeling program developed by Pardo et al. [2001], the opacity and Raleigh-Jeans (RJ) brightness temperatures have been extrapolated in and around the ACT bands throughout the year with the results shown in Figure 2.5 [Marriage, 2004, 2006]. The ACT bands are situated between three large emission features, an O_2 resonance at 119 GHz and water resonance lines at 183 GHz and 325 GHz [Danese and Partridge, 1989]. The level of emission in the continuum where the ACT bands lie is dominated by the size of the wings of the two water lines, and so the transmission and absorption in the ACT bands is dominated by the amount of PWV in the atmosphere. Seasonal changes in the weather provide sustained periods with low amounts of water vapor and naturally set the ACT observing seasons to the austral winter months with the best observation conditions typically between June and December.

The high-altitude location presents several significant logistical challenges, including site accessability, remote operation, and health concerns such as altitude sickness from extended periods at high altitude. The ACT site is approximately 50 km from the town of San Pedro de Atacama ($\sim$ 2750 m), where our lodging and main field offices are located. It takes about 45 minutes to travel from San Pedro to the ACT site: 35 km on paved roads and 15 km on abandoned mining roads. The roads are clear year-round with brief (1–2 day) periods of inaccessibility due to snow. Communications with the site are possible through a data link consisting of a 60 cm parabolic antenna in San Pedro and a 1.2 m parabolic antenna at the site, and an Orthogon PTP600 transreceiver pair operating at 5.8 GHz. The overall communications rate is $\sim$ 100 Mb/s. Connection to the Internet is made in San Pedro; this connection limits the speed of communication from North America to the site to 1 to 10 Mb/s. The data link allows for most telescope systems be monitored and controlled remotely

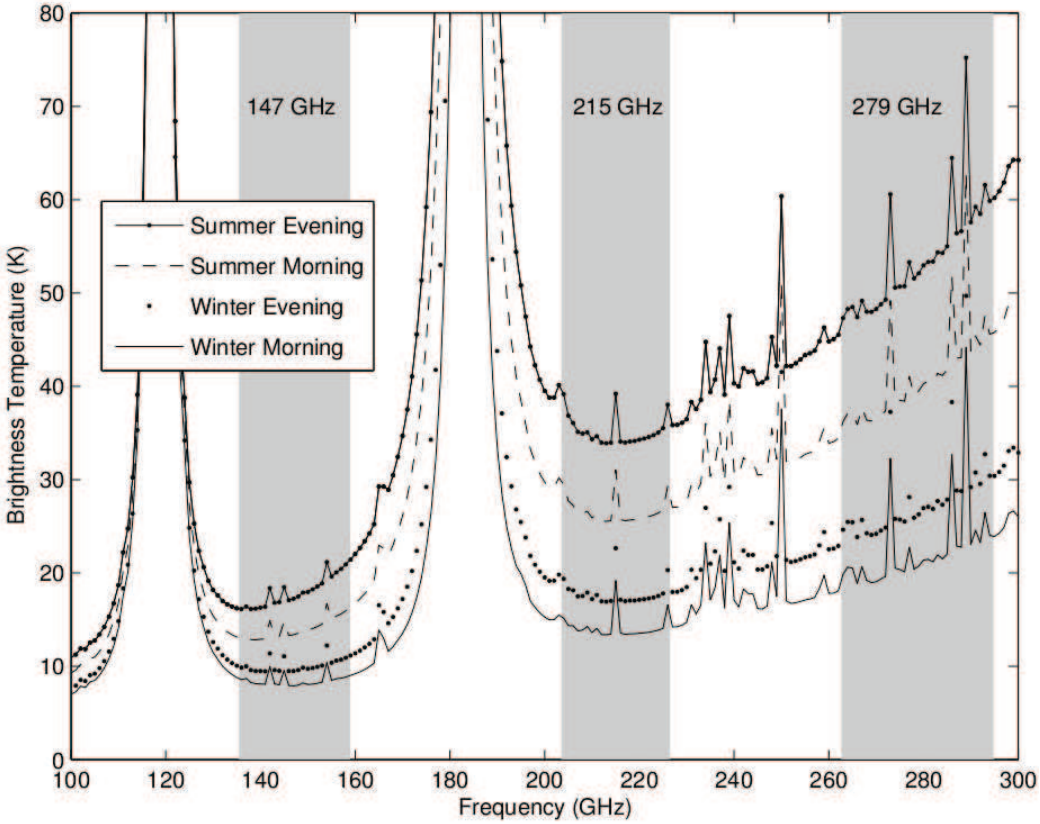

Figure 2.5 Estimated Rayleigh-Jeans brightness temperature spectrum for average values of PWV for different seasons and times of day. Data are estimated from an atmospheric transmission model using NRAO/ESO radiometer measurements at 225 GHz over the Chajnantor plain near the ACT site. The ACT bands are approximately given by the gray shaded regions. The emission in the ACT bands are dominated by water vapor. Seasonal changes and diurnal changes in the level of water vapor cause changes in the size of the water lines, which change the continuum level in the ACT bands. Morning is 5:00–17:00 UTC. Winter is June to November. Here, "Summer Evening" is 2.15 mm PWV, "Summer Morning" is 1.55 mm, "Winter Evening" is 0.94 mm, and "Winter Morning" is 0.69 mm. Figure from Marriage [2006].

from North America. Four sea-shipping containers are located near the telescope and are used during on-site work. A climate-controlled main container houses the site computers and work stations, along with the compressors for the pulse-tube cryocoolers (Section 3.5) and robotics motion control system (Section 6.1). A second container is used for reassembling MBAC and serves as our laboratory and workshop. The final two containers are used for storage. Figure 2.6 shows a picture of ACT and the site layout taken from above on Cerro Toco.

2.4 Scan Strategy

Signal modulation is often incorporated by CMB experiments to reduce the effects of drifts in the detector response. Typically, this is done by moving the telescope beam on the sky on timescales faster than the $1/f$ knee of the low frequency noise but slower than the time constants of the detectors. For ACT, the sky signal is modulated by scanning the entire 40 metric ton upper structure $\pm 2.5°$ in azimuth while holding the elevation fixed (typically at 50.5°). Scans are done at two positions east and west of an arc between the south celestial pole (SCP) and the zenith. As the sky rotates, an annulus around the SCP is mapped out (Figure 2.7).

This observing strategy has several benefits for observations from the ground. Changing the amount of airmass affects both the gain of the system from atmospheric absorbtion (Equation 2.3) and the background loading from gray body emission (Equation 2.4). Keeping the elevation fixed ensures the amount of atmospheric airmass is constant during a scan, preventing a scan-synchronous atmospheric signal. Second, by performing scans both east and west along the SCP-zenith arc, the mapped annulus will be observed in two different crosslinked orientations (see Figure

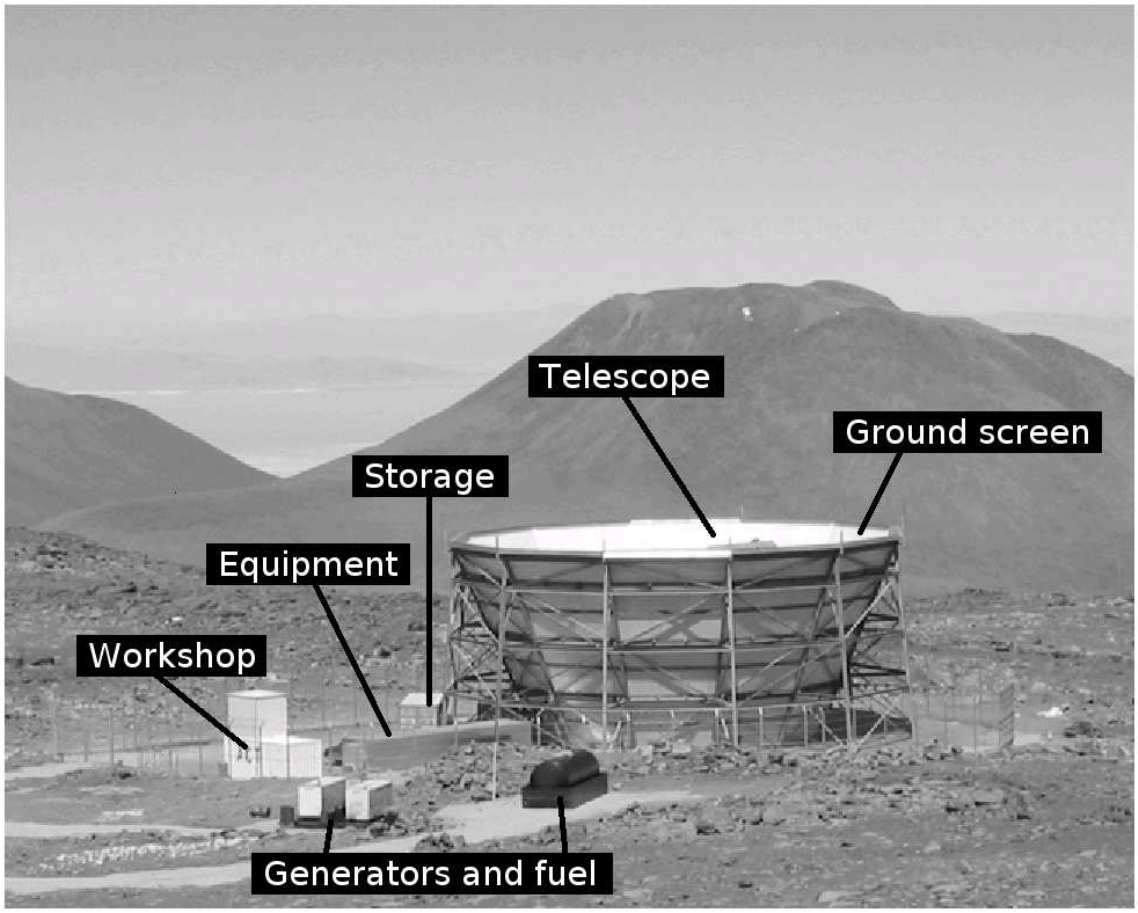

Figure 2.6 The ACT site at 5190 m on Cerro Toco. The telescope is surrounded by a 13 m high outer ground shield. Outside the ground shield are four sea-shipping containers: an Equipment Room 12 m $\times$ 2.5 m $\times$ 2.5 m, a Lab Workshop 6 m $\times$ 2.5 m $\times$ 2.5 m with a vertical extension over half of the container that increases the height to 5 m, and two storage containers 6 m $\times$ 2.5 m $\times$ 2.5 m. The Lab Workshop is used to reassemble MBAC on-site; the climate-controlled Equipment Room houses the compressors, motion control system, and site computers; two containers are used for storage. The site is powered by switching between two diesel generators which are automatically filled by a storage tank which holds approximately 15000 L of diesel. During normal operations $\sim$ 250 L are consumed per day. Picture from E. Switzer.

2.7). Crosslinking has been shown to be critical for the removal of scanning-induced systematic effects such as striping from the maps [Bennett et al., 2003, Tegmark, 1997]. Finally, by moving the entire upper structure of the telescope, including the primary, secondary, and receiver, the detectors are constantly looking through the same optical chain. Scanning with the complete optical system on the sky (as opposed to using an optical chopping mirror) avoids many scan-synchronous signals that could potentially arise from changing the optical path such as beam shape, mirror emission, or ground pick-up. Chapter 6 discusses the considerable requirements this modulation strategy places on the scan and pointing stability of the telescope structure.

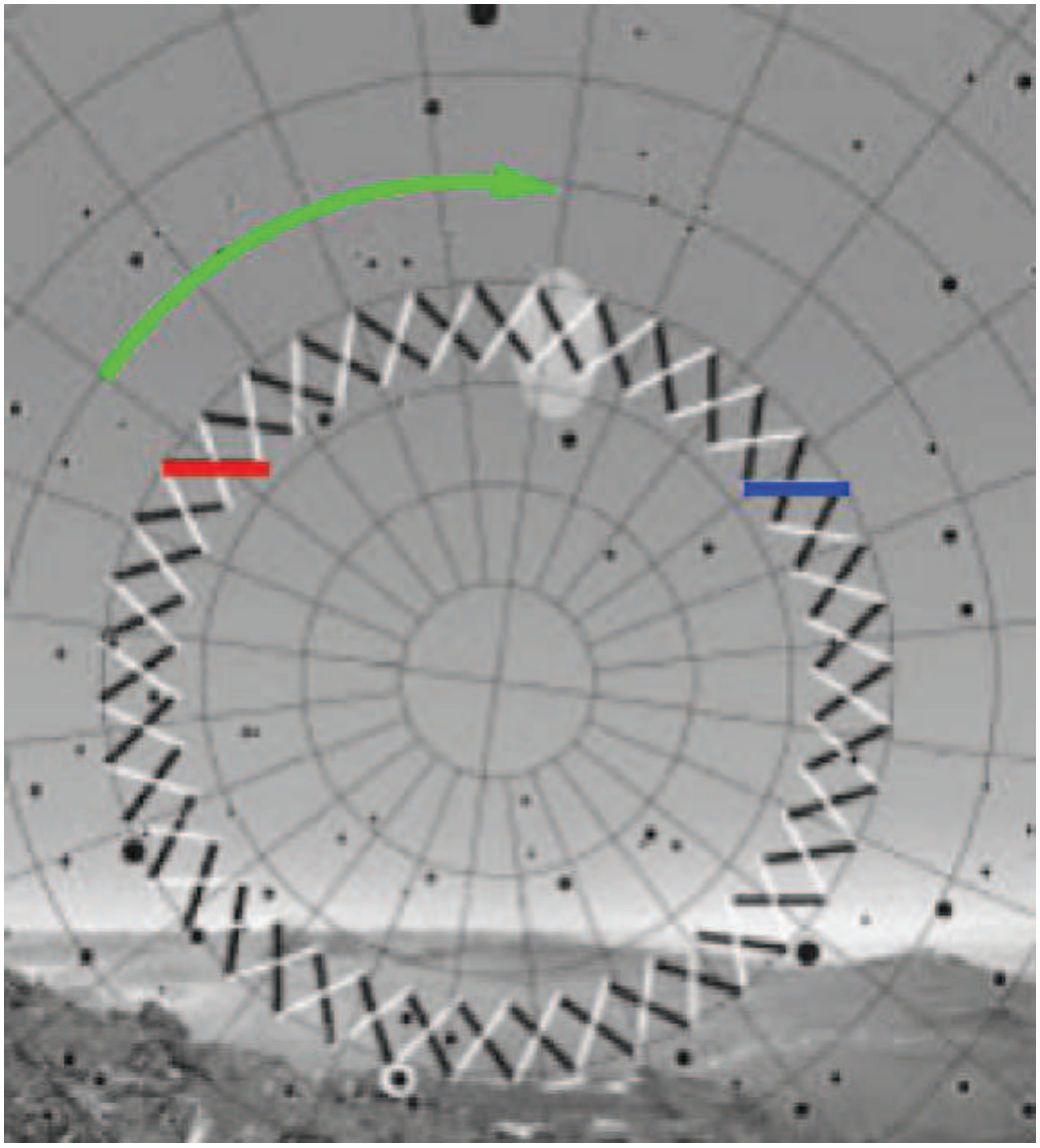

Figure 2.7 An example of the ACT scan strategy. The telescope scans at constant elevation at two azimuth positions east and west of the arc between the SCP and the zenith (the red and blue lines). As the sky rotates (green arrow), an annulus is mapped out. Because the scan is offset from the SCP, sky rotation changes the crossing angle of the east and west scans (black and white lines). This crosslinked scanning helps to remove systematic effects from the maps. Figure courtesy of J. Klein.

Chapter 3

The Millimeter Bolometer Array Camera

MBAC is a cryogenic receiver and science camera designed specifically for ACT. The design was based on meeting the scientific goals and requirements of the ACT project discussed in Section 1.5. These requirements mandated a new instrument, with unique capabilities. This chapter discusses the design, implementation, and integration of the major systems of MBAC. We found that to map the temperature anisotropies of the CMB to the required signal to noise simultaneously in three frequencies, three separate sets of reimaging optics were necessary to feed the three arrays. The first section discusses the optics design, the choice of vacuum windows, and spectral filtering necessary to define the three frequency bands. It describes the mechanical design chosen that provided sufficient close-packing such that the three arrays could be fit onto the focal plane of the telescope, while still being able to maintain optical elements feeding them at five temperatures ranging from 300 K to 300 mK. The second section presents an overview of the design of the optics tubes,

including a description of the cryogenic and mechanical mounts for the optical elements. The heart of the instrument is the three detector arrays, which are the subject of Section 3.3. A complete description of the arrays is presented elsewhere. I do, however, give a brief overview of the detector technology, and a description of the actual detectors and readout used. The readout of the bolometer arrays is sensitive to magnetic fields, and the implementation of magnetic shielding is discussed in Section 3.4. In order for the detector arrays to be sufficiently sensitive to map the anisotropies of the CMB, they have to be cooled to 300 mK. The refractive optics could not be at 300 K either as their emissivity would be too large. Therefore, it was necessary to design a cryogenic system where the temperature of each element was optimized to be cold enough not to contribute a significant thermal background, yet minimize the loads at 1 K and 300 mK where the cooling capacities are limited. Further constraints came from the remote site location and the whole structure had to be rigid enough to withstand the stresses produced by the rapid scanning and turnarounds of the telescope. The cryogenic design is the subject of Section 3.5. MBAC mates directly to the telescope, roughly on the rotation axis, and scans with it; all optical elements move together during the scan. With this scan strategy in mind, the MBAC cryostat was designed to be extremely rigid while being as lightweight as possible. Section 3.6 gives an overview of the overall mechanical design that houses the optics, detectors and cryogenics. The mating and alignment to the telescope is also presented. The final section presents mechanical tests of rigidity to which the receiver was subjected.

3.1 Cold Reimaging Optics and Filters

ACT's primary and secondary mirrors are an off-axis Gregorian that produces a 1° square field of view. Three sets of reimaging optics transfer a piece of the telescope's square-degree field onto three separate focal planes. At each focal plane is an array, one optimized for observations at 145 GHz, another at 220 GHz and the third at 280 GHz. The images are diffraction-limited for each array, and the field of view (FOV) for each array is an approximately $0.3° \times 0.3°$ field on the sky that does not overlap (or even touch) the FOVs of the other detectors (see Figure 3.2). Each set of reimaging optics has a cold aperture stop that defines the illumination of the secondary and primary mirrors.

Several designs were considered, including all reflective systems, all refractive systems, and hybrids of the two. Designs using a shared optical path with dichroic beamsplitting filters to separate the frequencies were compared with designs containing separate optical paths. The reimaging optics must be cooled to reduce loading from emission. It also needs to fit inside a roughly cubic meter space because of size and weight restrictions incorporated in the design of the telescope. We were not able to develop a reflective design that would fit inside a cubic meter because dichroic beam splitters are (even at the time of this writing) not available at the diameters necessary. Their development could have slowed down deployment or would have mandated slower cold optics that increased the size beyond the space available. We finally settled on using three separate optical paths, each with its own refractive lenses and filters optimized for its observing frequency. This separate three-camera design has several advantages. Wide-band anti-reflective (AR) coatings are difficult to make, optimizing over a small band insures higher transmission through the op-

tical elements. The three-camera design decouples each array's optics and filters, which allowed for the development and deployment of the receiver in stages. The optical components at a given frequency are on-axis with cylindrical symmetry. This geometry allows the optical elements to be placed in an optics tube that provides shielding for the arrays against stray radiation. A disadvantage of the design is that the three arrays do not image the same region of sky simultaneously. The offset between arrays is minimized by packing the three optics tubes as closely together as is mechanically possible. The resulting triangular configuration (shown in Figure 3.1 and 3.7), has the 280 GHz camera placed in the telescope's plane of symmetry due to its tighter diffraction requirements, and the 145 GHz and 220 GHz cameras below and on either side of the telescopes plane of symmetry. This arrangement coupled with the ACT scan strategy maximizes the sky coverage overlap. As the telescope scans back and forth, the bottom two arrays mostly observe the same region of sky; only in the turnaround region are their fields not overlapping. Quick turnarounds reduce the amount of observing time where the fields are not overlapped. Sky rotation moves the lower observed region through the upper camera (or vice-versa when the telescope is observing on the west side of south).

The final design incorporates three lenses for each optics path. Details of the design procedure, optimization, and analysis can be found in Fowler et al. [2007]. A three dimensional model with a ray trace for the three frequencies is shown in Figure 3.1. All the lenses are made out of high-purity silicon. Silicon was chosen as the lens material because of its high index of refraction (n = 3.416 [Lamb, 1996]) and its high thermal conductivity at cryogenic temperatures. All the lenses are plano-convex to ease manufacturing and simplify mechanical mounts. High-purity was used to reduce absorption loss at millimeter wavelengths. An AR layer is added to each lens by

coating it on both sides with a thin layer ($\sim$ 300 µm thick) of machined Cirlex (n = 1.84) that is glued to the surface of the silicon using Stycast 1266 [Lau et al., 2006b]. The first lens, located just after the Gregorian focus, forms an image of the primary mirror on a cold aperture stop (Lyot stop) that defines the illumination of the primary by the arrays. The second and third lenses refocus the sky onto the focal plane where the arrays are placed. The optics were designed to maximize the Strehl ratio over the focal plane. Calculations using the CodeV optics design software predict greater than 0.97, 0.94, and 0.96 across the entire focal plane region, with average Strehl ratios of 0.99, 0.98 and 0.98 for the 145, 220, and 280 GHz cameras, respectively.

Table 3.1 lists the physical and optical parameters of the arrays. The detectors are 1.05×1.05 mm squares, with a spacing of 1.05 mm (horizontal) by 1.22 mm (vertical) configured in a 32×32 rectangular grid with dimensions of approximately 34×39 mm. The geometry is the same for the three arrays. The focal ratio F is ≈ 0.9 for all arrays, with effective focal length $f \approx 5.2$ m and primary mirror illumination of $\approx$ 5.8 m. Each array's field of view is approximately 22 arcminutes $\times$ 26 arcminutes. In terms of angle on the sky, the detectors are spaced approximately $1/2F\lambda$ to $1.1F\lambda$ going from the lowest to highest frequencies, with a detector spacing of approximately 42 arcseconds by 49 arcseconds on the sky. For 145 GHz, the entire field is fully sampled in a single pointing. Figure 3.2 shows the the relative sky spacing of the detectors for the three arrays with disks that illustrate the approximate beam size.

A series of capacitive-mesh low-pass filters and a band defining filter are used to define the frequency band of each detector array (Section 3.1.2). The optical components, including the filters, are held at five different temperatures: 300 K, 40 K, 4 K, 1 K, and 300 mK (Figure 3.1)[1]. The temperatures of the filters and lenses were

[1]These are the approximate temperatures these stages reside at. These separate cryogenic stages

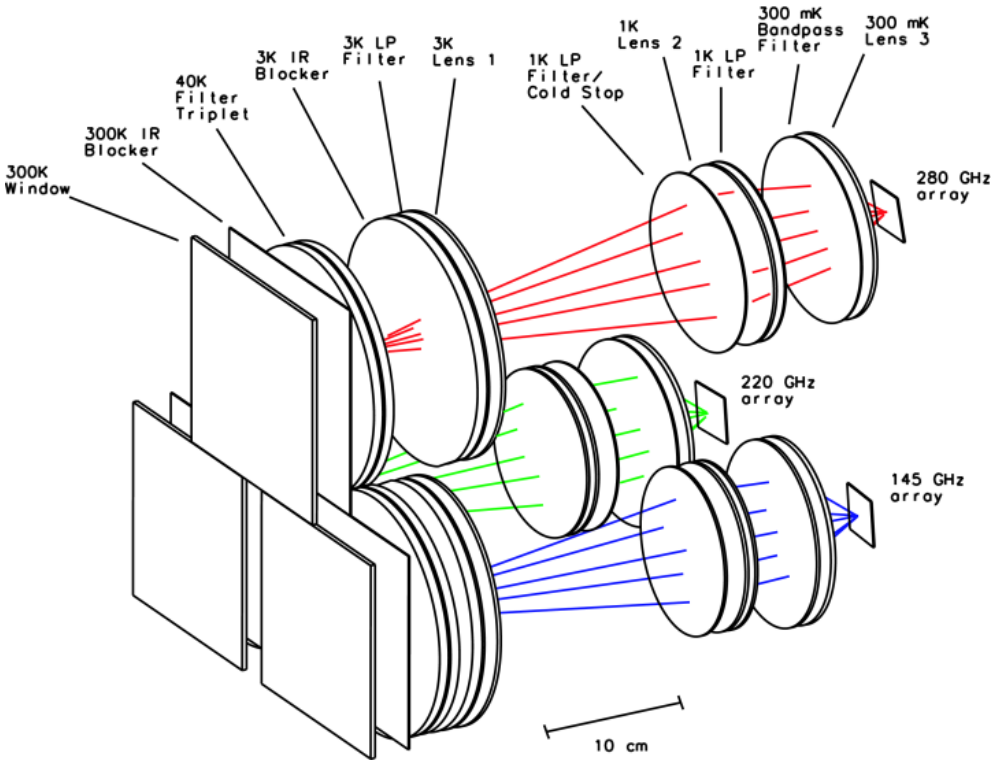

Figure 3.1 Three dimensional model of the cold reimaging optics for MBAC. The optical elements for each array are separated into individual optics tubes. Each array has a similar set of optical elements. The 280 GHz elements and temperatures are labeled. The lenses are labeled Lens 1 to 3, with Lens 1 one being closest to the 300 K window. The low-pass capacitive-mesh filters are labeled LP and the band-pass filter as BP. Infrared blocking filters are labeled IR. The temperature of the components decrease moving toward the arrays to reduce the loading, with the band-pass filter, Lens 3, and arrays all held at 0.3 K. Figure made in collaboration with R. Thornton

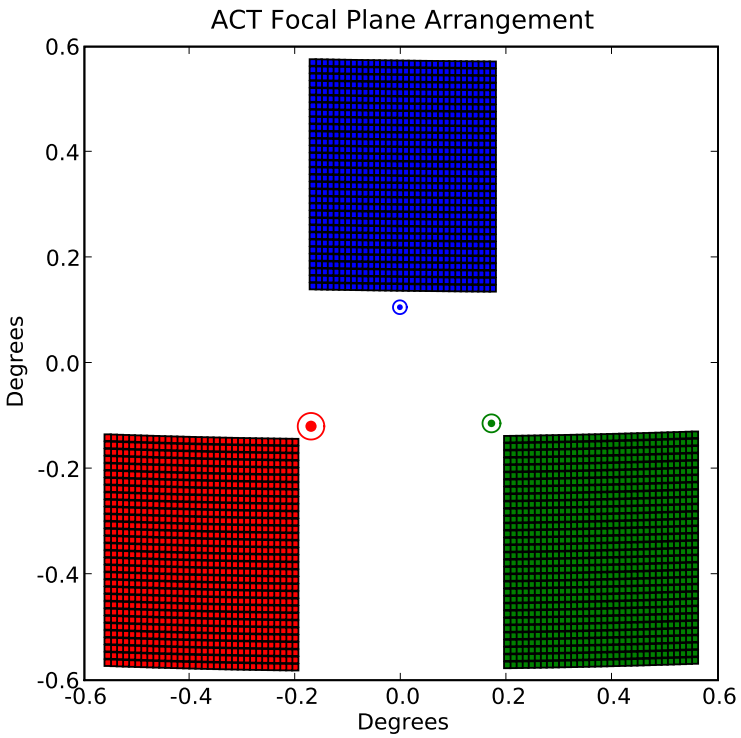

Figure 3.2 The idealized arrangement of the ACT detectors on the sky. The red squares represent the 145 GHz detectors, the green squares represent the 220 GHz detectors, and the blue squares the 280 GHz detectors. The circles represent the approximate size of each detector's beam. Filled circles show the extent of the approximate full width at half-maximum. The open circles show the first minimum in the beam and give the size of the main lobe. Figure courtesy of J. Fowler

Physical Properties	
Pixel size	1.05×1.05 mm
Pixel spacing	≈ 1.05 mm horizontal $\times$ 1.22 mm vertical
Array configuration	32×32 rectangular grid
Array size	≈ 34 mm horizontal $\times$ 39 mm vertical
Optical Properties	
Effective focal length	≈ 5.2 m
Primary illumination	≈ 5.8 m
Focal ratio	≈ 0.9
Detector spacing	$\approx 42''$ horizontal $\times$ $49''$ vertical
Array FOV	$\approx 22'$ horizontal $\times$ $26'$ vertical

Table 3.1 Important parameters for the MBAC detector arrays. The properties for all three arrays are similar.

chosen both out of necessity and mechanical convenience.

The close-packed detector design does not allow for the use of feedhorns. Therefore, each detector sees loading from 2π steradians. The Lyot stop defines the mirror illumination, and is cooled to 1 K so that the non-sky spillover power reaching the detectors from their large acceptance angle is at or below this temperature. The set of filters and the second lens nearest to the Lyot stop are also cooled to 1 K with all elements held in a single assembly. The placement of the final lens with respect to the array has the tightest tolerance[2] of all optical elements, $\approx 600\,\mu$m, and is attached directly to the array mounting assembly and cooled to ≈ 300 mK. This arrangement made it possible to have a strong mechanical connection at a single temperature so that the 600 µm tolerance could be insured. The final band-pass filter sits in front of the final lens and is also cooled to ≈ 300 mK. Behind the band-pass filter, the array is enclosed in a 300 mK cavity which is painted with a Stycast and lampblack coating to absorb stray light [Bock, 1994]. The actual temperatures of the remaining upstream

are also mechanically separated. We will refer to them throughout by these approximate temperatures.

[2]The necessary tolerance was defined as the amount a lens needed to be misplaced to produce a 1% decrease in the Strehl ratio. Details of the tolerancing calculations can be found in Dicker [2005].

optical elements are not critical; they are cooled in stages to limit the loading on the downstream optical elements and the cryogenics needed to cool them.

3.1.1 Vacuum Windows

One challenge posed by the optical design was building a vacuum window that would accommodate all three arrays simultaneously. The vacuum window was placed near the Gregorian focus of the telescope to minimize the size of the window and reduce the radiative load entering the cryostat. Even at this position, the smallest single window which encircled the beams for all three arrays was over 50 cm in diameter. At this size making a single large window becomes difficult. Another problem with a single large window is in the application of an AR coating. The optimal thickness to minimize reflections for an AR layer at wavelength λ with coating refractive index n is $\lambda/4$n while an AR layer of thickness $\lambda/2$n gives maximum reflections; therefore a single thickness AR coating is not possible for all three of the ACT wavelength bands. To accommodate these demands, we chose to use three separate rectangular vacuum windows. A rectangular window takes advantage of the image shape of the array at the window (shown in Figure 3.19 and Figure 3.1). The drawback to a rectangular window is that the stress is not uniformly distributed along the circumference, as in a circular window, but instead is concentrated in the corners.

A number of window materials were considered. Thin window materials ($\sim$ 200 µm thick), such as Mylar and Kapton, have several disadvantages. Because they are thin, they are fragile—the chance of an accidental breakage is considerable. They also typically have high refractive indices ($\sim$ 1.83 at 140 GHz [Lamb, 1996]) that increase reflections and reduce transmission. Thick window materials ($\gtrsim$ 20 mm thick) made

of expanded or extruded foam (such as Zotefoam) have been used by several groups for robust, low-loss ($\approx 1\%$ at 150 GHz) vacuum windows [Glenn et al., 2003, Runyan et al., 2003, Yoon et al., 2006]. However, they have several disadvantages that make them unusable as windows for MBAC. The thickness of the pieces make them difficult to mount given the close spacing of the beams and the material deforms considerably along the beam axis when the cryostat is evacuated. Absorption loss in the window is also a concern at our higher frequency bands. The amount of loss is strongly dependent on the density of the foam (with higher densities having more loss) and begins to rise above 220 GHz [Kerr et al., 1992]. Therefore, we were left with medium thickness materials ($\sim$ 4–9 mm) with moderate indices of refraction. We choose to use 4 mm thick Ultra High Molecular Weight Polyethylene (UHMWPE) as the window material with an index of refraction of ~ 1.53 at 160 GHz [Lamb, 1996]). Peter Ade's group at Cardiff University in Wales was able to bond expanded-Teflon sheets as an AR coating. Expanded-Teflon is obtainable with indices of refraction in the range of ~ 1.1 to 1.44 at 140 GHz; we use an index of 1.2, which is approximately $\sqrt{1.53}$. Since each wavelength has its own window, we are able to use the correct thickness ($\lambda/4$n) to minimize reflections on each window. UHMWPE is nearly ideal: it is extremely strong and deforms only $\sim$ 3 mm in the middle of the $\sim$ 15 cm $\times$ 15 cm window, and has low absorption at millimeter wavelengths. With the correct AR coatings, such as those just described, reflections at the interfaces can be kept low. Measurements of the MBAC windows using a Fourier transform spectrometer show transmissions of over 96% for the 145 GHz and 220 GHz bands and over 93% in the 280 GHz band (shown in Figures 3.4, 3.5, and 3.6).

3.1.2 Filters and Bandpass Measurements

The frequency response of the bolometric detector arrays for MBAC are defined by the transmission through the optical elements in the optical path to the detectors. The frequency transmission band is set primarily by the series of low-pass (LP) capacitive-mesh filters and a band-defining edge (BP) filter provided by Cardiff University. Details of the filter design can be found in Ade et al. [2006]. Multiple filters are used because the LP filters tend to have transmission leaks at harmonics of their cut-off frequency. The use of filters with a range of cut-off frequencies allows subsequent filters to suppress the out of band leaks from previous filters. Filters are placed at each successive cryogenic stage along the optics path, to limit loading on the next stage. They are arranged from highest frequency cut-off to lowest. There are also a series of 4 µm thick infrared-blocking (IR) reflective filters to reduce the optical loading on the cold stages [Tucker and Ade, 2006]. These IR blocking filters prevent the center of the poorly conducting LP filters from heating up and consequently reduce the radiative loading from the windows. Each optics tube contains 10 filter elements, including the windows. Table 3.2 lists the temperature, location, and low-pass cut-off frequency for each of the filters in the MBAC optics chain, and Figure 3.8 shows the filter mounting locations along the optical path of the 145 GHz channel. Figure 3.1 shows all the filter and lenses in free space.

Prior to installation, each filter's frequency response was measured using a Fourier transform spectrometer (FTS) by Cardiff. A composite transmission spectrum was made by multiplying together the individually measured filter responses. After the filters were installed into MBAC, FTS measurements were made on the entire optical path at Penn. We adapted the FTS (based on a polarizing Martin-Puplitt interfer-

ometer design) designed for the BLAST experiment to measure the bandpass. To align the FTS with MBAC, the FTS was placed on a lab bench and MBAC was rotated to a horizontal position to match the optical path of the FTS. The FTS has a focal length of 24 inches (60.96 cm), fed at F of 4.8. The FTS was placed so that the focus of the FTS aligned roughly with the ACT Gregorian focus, which occurs ~ 50 mm behind the MBAC front window plate, allowing us to use the FTS without having to make separate reimaging optics for the FTS. The drawback was that the FTS only illuminates a small fraction of the detector array. Several interferograms were taken on each of the three arrays (an example interferogram is shown in Figure 3.3). The Fourier transform of the resulting interferogram is a measure of the spectral transmission of the optical system. The individual interferograms were analyzed separately, and the resulting spectrum, $\Theta(\nu)$, were averaged to give the final results. Plots of both the warm individual filter measurements and the average measured cold filter bandpass in MBAC are shown in Figures 3.4, 3.5, and 3.6 for the 145, 220, and 280 GHz frequency channels. For the MBAC transmission spectrum, we first divided by the spectral emission of the FTS source (which was a thermal blackbody at 980° C) and normalized to the peak transmission of the composite spectrum. We then calculate the effective bandwidth as

$$\Delta\nu = \int d\nu \Theta(\nu), \tag{3.1}$$

and effective bandcenter as

$$\nu_0 = \int \nu d\nu \Theta(\nu)/\Delta\nu. \tag{3.2}$$

The results are given in Table 3.3. There is a slight discrepancy between the

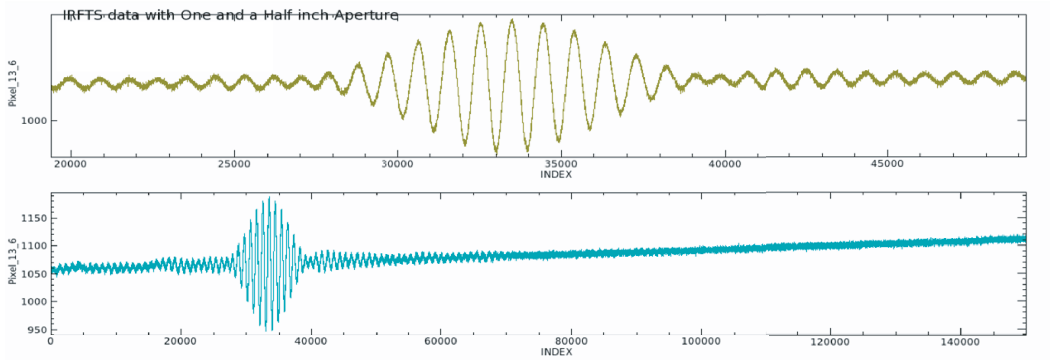

Figure 3.3 Interferogram measured in MBAC using the BLAST FTS on a detector in the 145 GHz array. The interferogram was taken through all the optical elements at their cold operating temperatures. In both plots, the y-axis is in digital detector readout units and the x-axis is in detector frame samples ($\approx$ 400 samples/second). The top plot shows a close-up of the zero-path length of the FTS. The bottom plot shows the entire 200 mm path length of the FTS's movable mirror. The Fourier transform of the interferogram is the spectral transmission of the optical system. The path length sets the maximum frequency resolution of the transmission spectrum to be 0.75 GHz. The slope is from a slow temperature rise in the 300 mK stage caused by loading in the cryostat from the 980° C blackbody source.

composite results from the individually measured filters and the spectrum obtained through the complete optical chain in MBAC. We also see structure in the bandpass measured for the cold filter set measured in MBAC which is not in the product of individual filters measured warm at Cardiff. We are currently trying to understand whether these differences are real, or artifacts induced by optical reflections and/or misalignments of the FTS.

Table 3.2 Filter location, temperature, and cut-off frequency of the filters in the order they are placed in the optical path. For low-pass filters, the approximate frequency cut-off is listed. For the band-pass filters, the expected band center is listed. Filter reference numbers are used for tracking purposes.

Filter Type	Ref. no.	Location	Size	Frequency
145 GHz			mm	GHz (cm^{-1})
Window	UHMWPE 1	Window Plate	150 × 150	—
IR blocker	C8–C12	Window Plate	150 × 150	—
IR blocker	C8–C12	40 K Filter Stack	ϕ 200	—
Low-pass	W1180	40 K Filter Stack	ϕ 200	360 (12)
IR blocker	C12–C16	40 K Filter Stack	ϕ 200	—
IR blocker	C16–C25	4 K Optics Stack	ϕ 200	—
Low-pass	W1318	4 K Optics Stack	ϕ 200	270 (9)
Low-pass	W1206	1 K Optics Stack	ϕ 135	210 (7)
Low-pass	W1223	1 K Optics Stack	ϕ 135	186 (6.2)
Band-pass	W1177	300 mK Optics Stack	ϕ 150	145 GHz
220 GHz				
Window	UHMWPE 2	Window Plate	150 × 150	—
IR blocker	P13695–P13656	Window Plate	150 × 150	—
IR blocker	P13461–P13486	40 K Filter Stack	ϕ 200	—
Low-pass	W1320	40 K Filter Stack	ϕ 200	360 (12)
IR blocker	P13460–P13487	40 K Filter Stack	ϕ 200	—
IR blocker	P13155–P13714	4 K Optics Stack	ϕ 200	—
Low-pass	W1232	4 K Optics Stack	ϕ 200	330 (11)
Low-pass	W1263	1 K Optics Stack	ϕ 135	300 (10)
Low-pass	W1231	1 K Optics Stack	ϕ 135	255 (8.5)
Band-pass	W1224	300 mK Optics Stack	ϕ 150	220 GHz
280 GHz				
Window	UHMWPE 3	Window Plate	156 × 156	—
IR blocker	P13657–P13694	Window Plate	156 × 156	—
IR blocker	P13615–13593	40 K Filter Stack	ϕ 200	—
Low-pass	W1xxx	40 K Filter Stack	ϕ 200	540 (18)
IR blocker	P13154–P13140	40 K Filter Stack	ϕ 200	—
IR blocker	P13703–P13679	4 K Optics Stack	ϕ 200	—
Low-pass	W1342	4 K Optics Stack	ϕ 200	450 (15)
Low-pass	W1264	1 K Optics Stack	ϕ 145	390 (13)
Low-pass	W1262	1 K Optics Stack	ϕ 145	360(12)
Band-pass	W1222	300 mK Optics Stack	ϕ 150	280 GHz

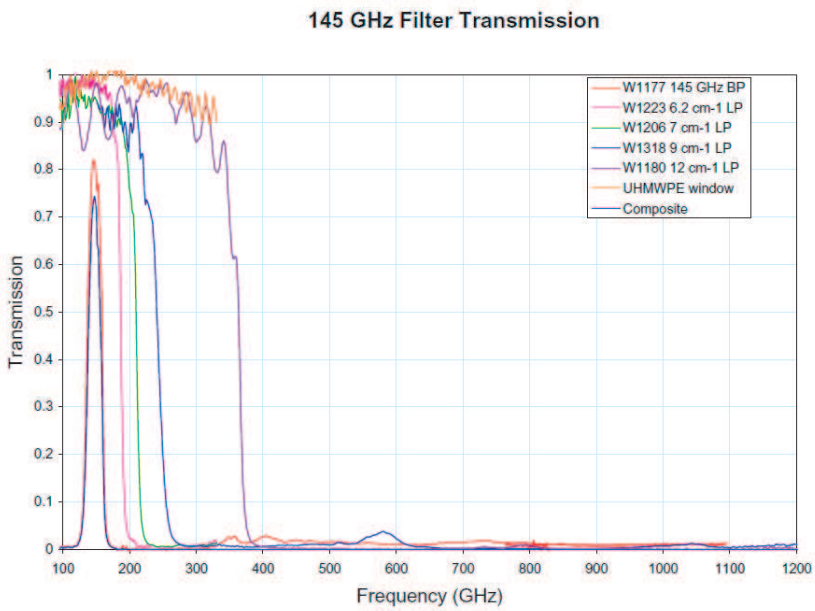

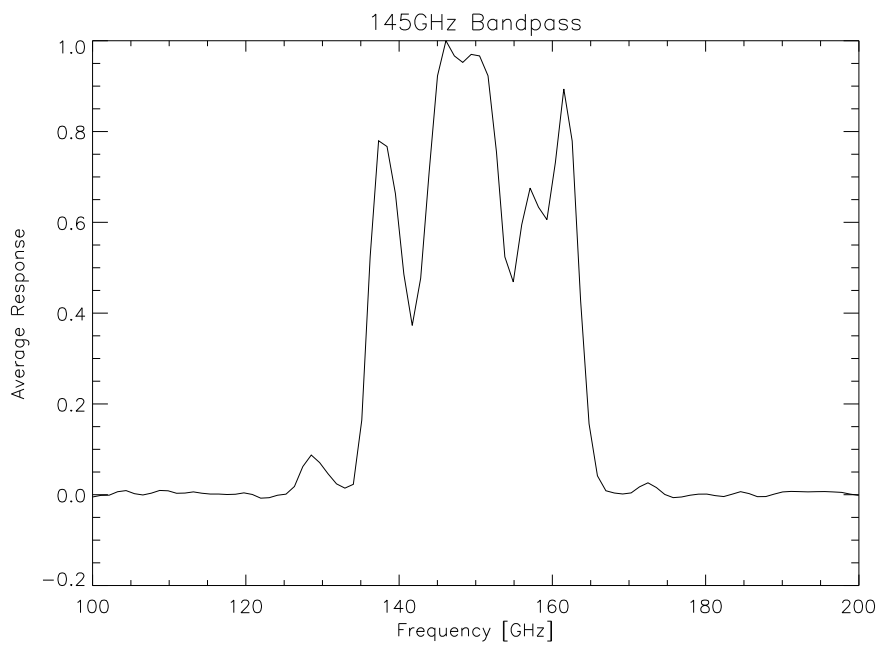

Figure 3.4 The 145 GHz filters. *Top*: Transmission of the individual optical filters and vacuum window that define the frequency transmission bandpass. A composite pass band of all filters is also plotted. The frequency resolution of the composite spectrum is 1.5 GHz. *Bottom*: Measured bandpass of the optical elements in MBAC. The frequency resolution of the measured bandpass is 0.75 GHz. Bandpass figure courtesy of D. Marsden.

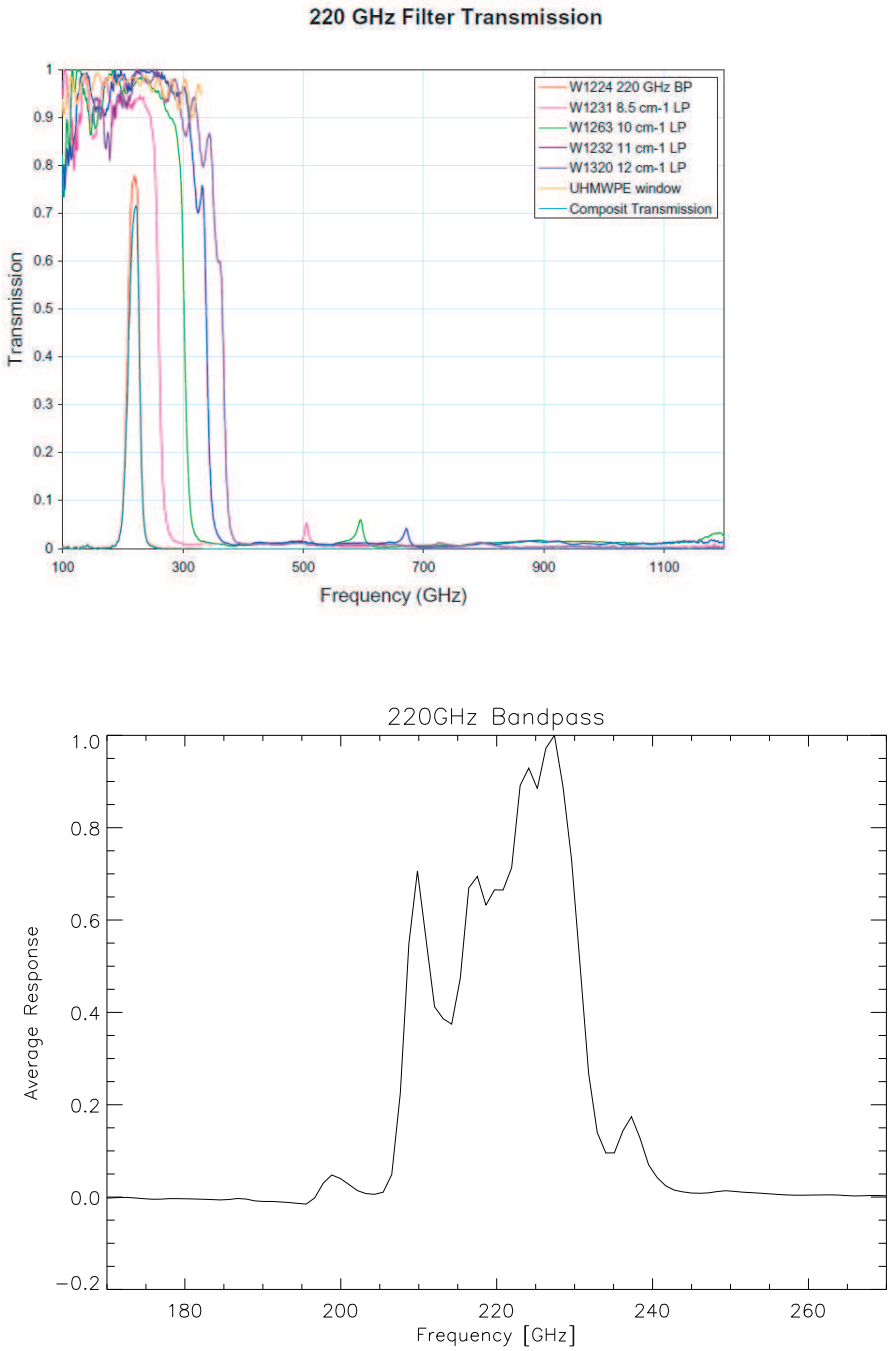

Figure 3.5 The 220 GHz filters. *Top*: Transmission of the individual optical filters and vacuum window that define the frequency transmission bandpass. A composite pass band of all filters is also plotted. The frequency resolution of the composite spectrum is 1.5 GHz. *Bottom*: Measured bandpass of the optical elements in MBAC. The frequency resolution of the measured bandpass is 0.75 GHz. The Bandpass figure courtesy of D. Marsden

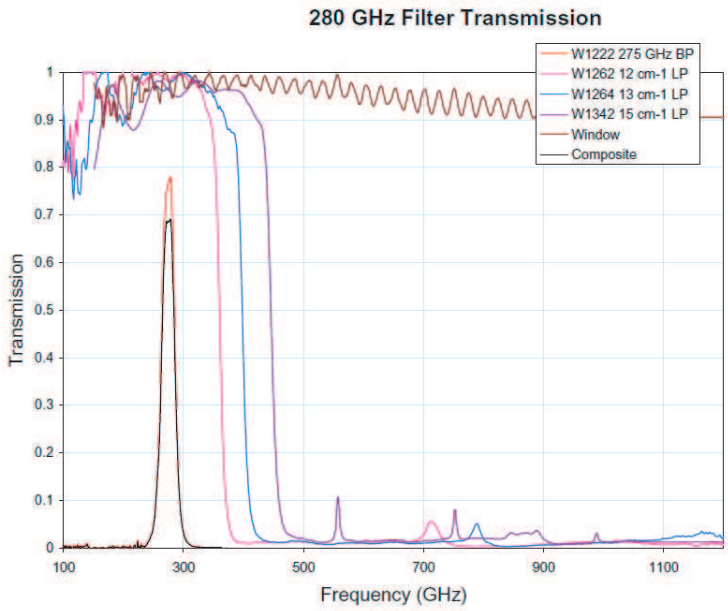

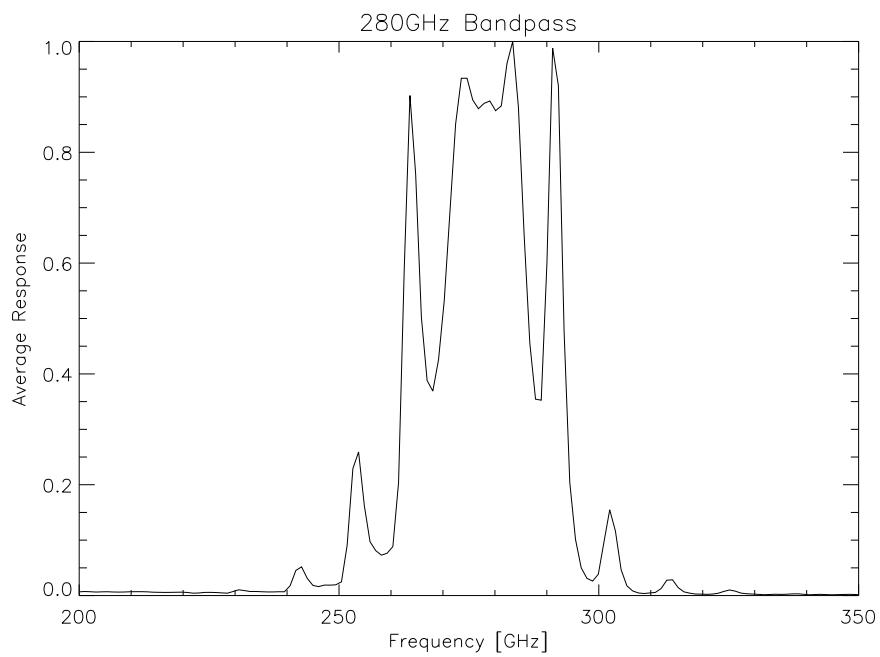

Figure 3.6 The 280 GHz filters. *Top*: Transmission of the individual optical filters and vacuum window that define the frequency transmission bandpass. A composite pass band of all filters is also plotted. The frequency resolution of the composite spectrum is 1.5 GHz. *Bottom*: Measured bandpass of the optical elements in MBAC. The frequency resolution of the measured bandpass is 0.75 GHz. Bandpass figure courtesy of D. Marsden

Table 3.3 Summary of the calculated properties from measurements of the MBAC filters. The composite transmission is obtained by multiplying the individual filter transmissions given by Cardiff. The MBAC measurements were made with all filters installed. The MBAC numbers are from averaging multiple bandpasses; the errors are the RMS deviation of those measurements. The number in parenthesis below the frequency array is the number of individual interferograms analyzed.

Array		Bandcenter ν_0	Bandwidth $\Delta\nu$	Max Trans.
145 GHz	Composite	146.8 GHz	21.2 GHz	0.774
(24)	MBAC	149.1 GHz ± 2.5 GHz	20.6 GHz ± 1.3 GHz	
220 GHz	Composite	217.8 GHz	21.5 GHz	0.716
(47)	MBAC	222.4 GHz ± 2.2 GHz	17.5 GHz ± 0.9 GHz	
280 GHz	Composite	274.3 GHz	26.9 GHz	0.691
(42)	MBAC	277.8 GHz ± 2.3 GHz	25.3 GHz ± 1.2 GHz	

3.2 Design of the Optics Tubes

3.2.1 Design Overview

As ACT is an off-axis Gregorian, the optimal focal plane is not perpendicular to the optical axis, and because the Gregorian focal plane is not telecentric, the lenses must be held at compound angles inside the cryostat. Each array has a separate optical path and the optical elements for each array must be closely packed to maximize sky overlap. The mechanical design must support the lenses, filters, and detectors in a space efficient way even during the fastest scanning motions of the telescope. Further constraints on the size of the optics tubes came from the size limitation of the cryostat and the volume within it occupied by the adsorption refrigerators required to cool under 4 K, radiation shields, and other structures. We decided that our requirements would be best met by a modular design that would allow the optics tubes to be individually disassembled, and reinstalled a number of times and the arrays could be deployed sequentially. Mounts are made large enough that there is at least 5

wavelengths of clearance between the most extreme ray and any mounting structures. The coefficients of thermal expansion of the various components were taken into account so that the relative positions between lenses are correct when the instrument is at its cryogenic operating temperatures. Thermal conduction between stages at different temperatures are minimized to enable roughly 18-20 hours of uninterrupted observations. Finally, the magnetic sensitivity of the superconducting detector multiplexers and amplifiers (Section 3.3) required that magnetic shielding be integrated into each optics tube.

To minimize weight, aluminum was generally used to mount elements at 300 K, 40 K, and 4 K. For the 1 K and 300 mK assemblies, where conductivity is critical and where aluminum is superconducting (and consequentially has reduced thermal conductivity), oxygen-free high-conductivity copper (OFHC, Copper 101) was generally used. Another reason for using mostly copper below ≈ 1 K is potential problems with trapped magnetic flux in superconducting aluminum alloys.

For flexibility of assembly, we have an interface plate to which all three tubes are bolted (Figure 3.7). This plate can be removed from the primary 4 K cold plate, allowing the removal of all three tubes from the cryostat as a unit. On this interface plate are mounted three individual aluminum wedges. The wedges fix the angles of the optical axes for each frequency channel. The angle is a compound one for 145 GHz and 220 GHz.

The base of the 4 K tube is attached to the wedge for each frequency. The supporting structure for the rest of the optics is mounted to the base of the 4 K tube (Figure 3.8). By removing a 4 K tube from its wedge, each frequency channel can be completely removed from the cryostat, which allowed the 145 GHz optics tube to be deployed in MBAC for the 2007 season while the 220 and 280 GHz optics tubes were

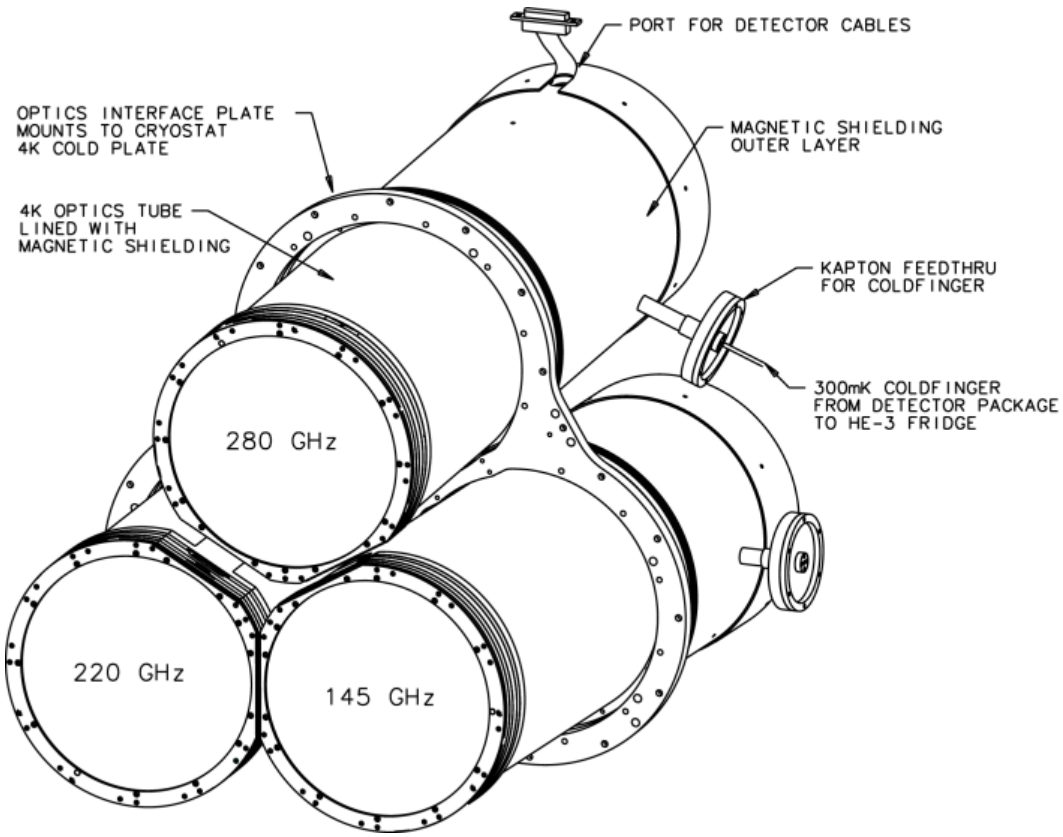

Figure 3.7 Outside of the assembled three-tube mechanical structure. Figure courtesy of R. Thornton.

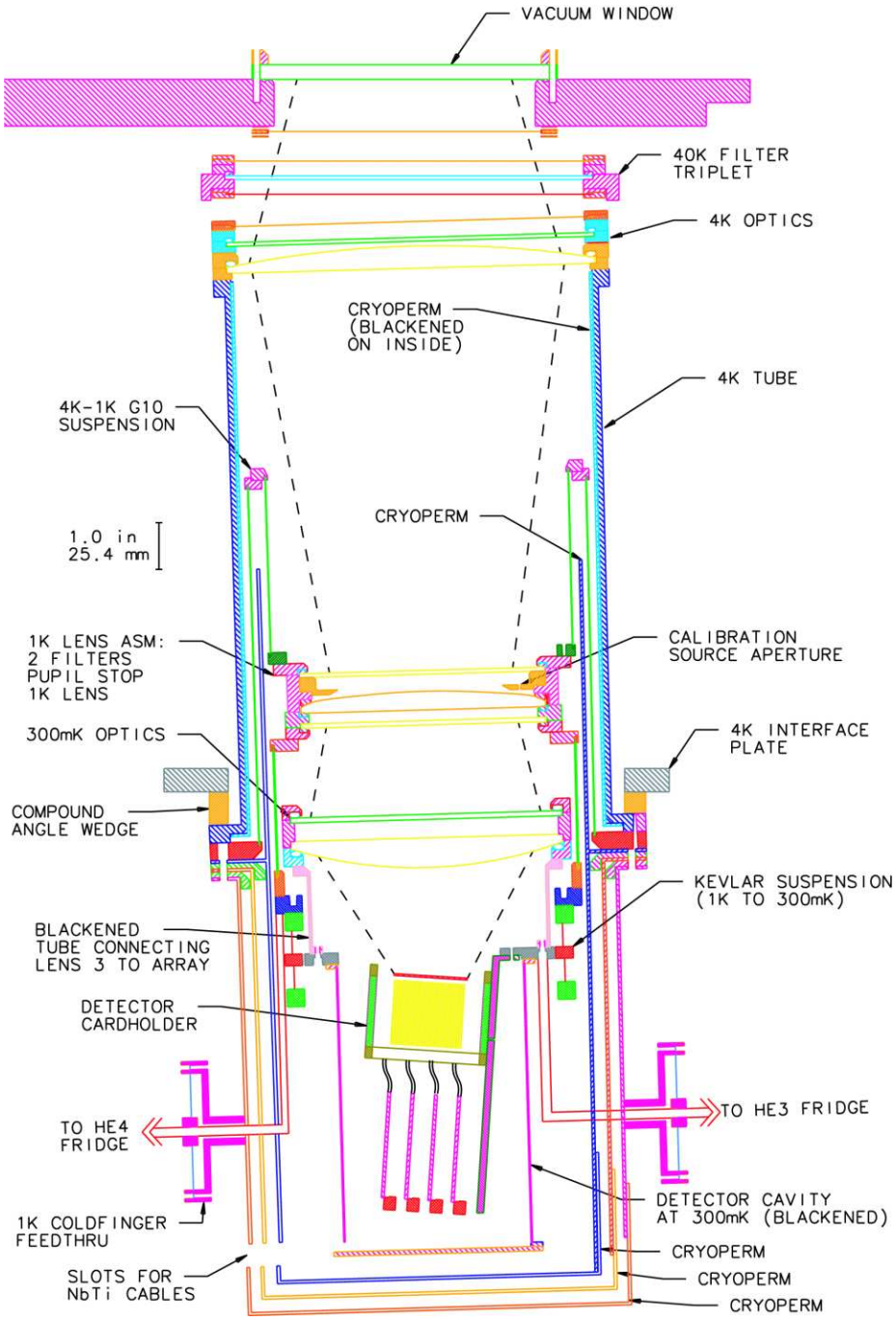

Figure 3.8 Cross-section of 145 GHz optics tube (the other two frequencies are similar). The dotted lines approximate the envelope of the light rays.

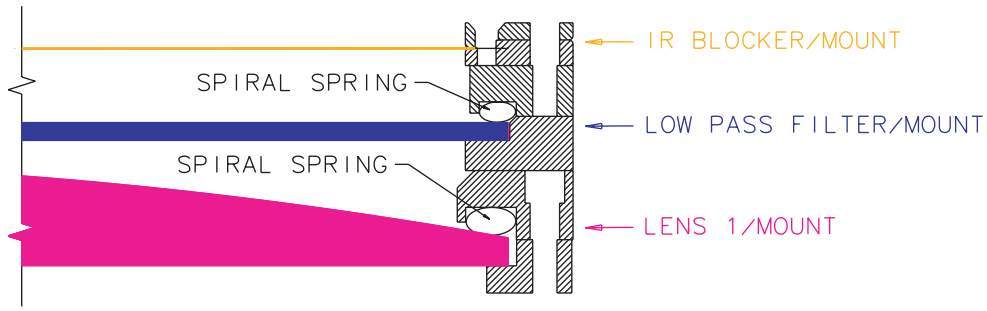

Figure 3.9 Cross-section of the edge of the 4 K optics stack. Light enters from the top, where a 4 micron-thick IR blocking filter is glued into an aluminum clamp. The next element is a low-pass filter, axially clamped by a spiral spring, as is the plano-convex 4 K lens.

being constructed. The three optics tubes are similar; hence the following discussion makes distinctions between frequencies only when appropriate.

3.2.2 4 K Optics Assembly

The 4 K optics stack consists of an thermal blocking filter, a LP filter, and the first lens, each 200 mm in diameter. They mount on the top of the 4 K tube. The cross-section shown in Figure 3.9 illustrates how the lenses and low-pass filters in MBAC are clamped in a rigid but compliant mount. The spring is a commercial electromagnetic interference gasket from Spira Manufacturing[3] wound out of spring-temper beryllium copper. The spring accommodates the curved lens surface as well as differential thermal contraction. It supplies a uniform clamping force around the circumference of the lens, which is important as the silicon lenses are brittle. To aid in thermal conductivity, a thin layer of low-temperature grease is applied around the circumference of the LP filter and lens.

We considered a second spiral spring (or other self-centering method) around the

[3]Internet URL: http://www.spira-emi.com.

perimeter of the lens to provide radial self-centering and conduction. However, space was limited in this direction, and decenter tolerances (roughly 3 mm, [Dicker, 2005]) were large enough so that it was acceptable to omit this second spring.

3.2.3 1 K Optics Assembly

The temperature of the next stack of optics is at $\approx 1\,\mathrm{K}$. The support structure between the 4 K and 1 K optics needs to provide enough thermal path length to minimize the load on the 1 K refrigerator, while having enough strength to rigidly support the remaining 7 kg of optical and detector structures ($\approx 2\,\mathrm{kg}$ for the 1 K assembly and 5 kg for the 300 mK assembly). We found that we could not use a single cylinder to support the 1 K optics on the 4 K tube because the cylinder could not simultaneously meet the requirements of stiffness and low thermal conductivity. Therefore we use two concentric and re-entrant G-10 (fiberglass) tubes (see Figure 3.8), each 0.38 mm thick and commercially available, to lengthen the conducting path.

Situated at the bottom of the inner suspension, the 1 K optics stack contains, in order: a low-pass filter, a pupil stop (Lyot stop), the second lens, and another low-pass filter. All mechanical structures are Copper 101 (OFHC). Mounted on the three pupil stops of each frequency are two calibration sources (see Section 5.2). The devices are connected with low-thermal-conductivity manganain wires that are routed out of the optics tube 4 K cavity through the same ports that the coldfingers feed through (Figure 3.7).

Connecting the 1 K optics stack to the 300 mK assembly is a third G-10 tube that extends down toward the port for the 1 K coldfinger from the ^{4}He refrigerator. It is necessary to have high thermal conductivity between the 1 K coldfinger and the 1 K

optics; but G-10 was chosen due to overall weight concerns. The G-10 tube is copper-clad and 6 additional copper straps are attached to the sides to increase thermal conductivity along its length. The internal part of this tube up to the location of the 300 mK lens cell, including the exposed flat surfaces of the lens cell and Lyot stop, are blackened with a mixture of Stycast and carbon lamp black to deaden the cavity to reflections [Bock, 1994]. At the end of this 1 K tube is a suspension for supporting the 300 mK assembly. The limited cooling capacity at 300 mK ($\sim$ 5 J and desired hold time of $>$ 18 hours, means the total loading from all three frequencies must be less than 80 µW; see Section 3.5.1) prevented G-10 from being used here. Four separate aluminum frames at 1 K hold, via taught Kevlar threads (1 mm diameter), a central inner frame that is bolted to the 300 mK assembly central mount plate (Figure 3.10). This arrangement makes the suspended plate extremely rigid in all directions. To insure proper alignment of the 300 mK mount plate to the rest of the optical system, an assembly jig is used which pins the location of the 1 K flange to the 300 mK mount during the Kevlar frame suspension assembly. Due to the tendency of Kevlar to stretch over time as well as its negative coefficient of thermal expansion, each segment was pre-stretched by hanging 11.4 kg for one week prior to assembly. After assembly, constant tension is applied to the thread by a system of vented screws and spring washers on each frame.

3.2.4 300 mK Assembly

The heat sink for the detectors must be well below the critical temperature, $T_c \approx$ 500 mK, of the TES devices (Section 3.3). Our system has a base (no-load) temperature of $\sim$ 250 mK with a nominal, loaded, temperature of 310 mK achieved via a

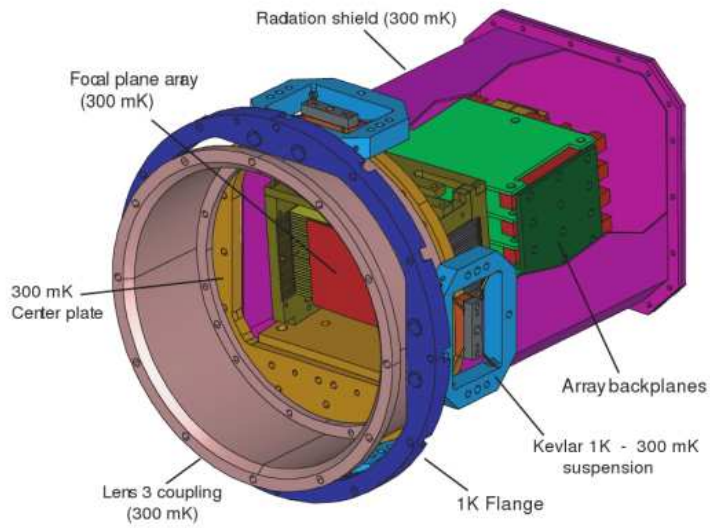

Figure 3.10 Detector 300 mK assembly CAD model showing the 1 K to 300 mK Kevlar suspension and a cutaway of the 300 mK detector shell. Figure made in collaboration with R. Thornton

^{3}He sorption refrigerator. For reasons already discussed, the final lens and band pass filter were designed to be at the same temperature as the detectors. The lens and detector assemblies are mounted on either side of the center plate supported by the Kevlar suspension. The filter and lens are clamped in a manner similar to that used to hold the 4 K optics. The tube connecting the 300 mK lens cell to the center plate is light tight and is blackened on the inside with a mixture of Stycast and carbon lamp black to absorb stray radiation.

On the other side of the 300 mK center plate (Figure 3.10), the 32 columns of the array are mounted in a array holder manufactured out of tellurium copper (Te copper). This material, while considerably easier to machine than OFHC, has a lower thermal conductivity; a worthwhile tradeoff given the complexity of the array holder. Each column is held in place by springs that apply force in two perpendicular directions to achieve the required array alignment specifications of roughly $\pm$ 20 µm [Lau, 2006,

Niemack, 2008]. The detector side of the 300 mK center plate is enclosed in a shell made of welded copper sheet. This shell shields the detector from 4 K radiation from the surrounding magnetic shielding (Figure 3.8). It is blackened on the inside with the mixture of Stycast and carbon lamp black used on other components. The shell also protects the detector array when handling the 300 mK assembly. The total mass of the 300 mK assembly for each array is approximately 5 kg.

3.3 Detectors and Readout Electronics

MBAC houses three 1024-element bolometer detector arrays designed to work at 145, 220, and 280 GHz respectively. These separate arrays are arranged in a triangular configuration at the reimaged focal plane of ACT (Figure 3.2). The arrays elements consist of pop-up TES bolometers developed at NASA Goddard Space Flight Center (GSFC) [Li et al., 1999]. Each array consists of 32 individually stacked columns, with each column consisting of 32 TES elements. The array elements are close-packed with no feed horns, filling the ACT focal plane.

Bolometric detectors are devices that absorb incident radiation and convert their photon energy, E, to heat. A bolometer typically consists of an absorber and a thermometer at temperature T with heat capacity C that are connected through a weak thermal link of conductance G to a heat sink held at a fixed temperature T_{bath} (see Figure 3.11). The photons heat the absorber above the bath temperature. The resulting temperature increase is measured by the thermometer and is proportional to the energy of the incident photons according to $\delta T = E/C$. The increased temperature of the device then decays back to its equilibrium temperature with a thermal time constant $\tau = C/G$. Phonon noise from thermal fluctuations in the bolometer can

limit their sensitivity [Moseley et al., 1984, Richards, 1994]. This noise arises from random phonon fluctuations across the thermal link and is $\propto \sqrt{T^2 G}$. To limit this noise, these devices are cooled to cryogenic temperatures ($\lesssim$ 500 mK), which reduces this thermal background noise.

In a TES bolometer, the thermometer is a superconducting thermistor [Irwin and Hilton, 2005]. During normal operation, the TES is voltage-biased approximately midway along its superconducting to normal transition. The large change in resistance over a small temperature change on the transition forms an extremely sensitive thermometer. Absorbed photons increase the temperature of the TES, causing an increase in resistance of the device. In MBAC, the TES is roughly voltage-biased by applying a constant current bias, I_b, across a small shunt resistor, R_{shunt}, in parallel with the TES, such that $R_{shunt} \ll R_{TES}$ (Figure 3.11)[4] . When photons are absorbed in the bolometer, the Joule heating of the device, $P_{ohm} = V^2/R_{TES}$, decreases as R_{TES} rises. This strong negative electrothermal feedback [Irwin, 1995] allows the TES to be stably biased along its superconducting transition, and also permits biasing of multiple TESs off a common line even with slight differences in their transition temperatures. The TES output signal is the device current which can be read out using multiplexed Superconducting Quantum Interference Devices (SQUIDs) [Chervanek et al., 1999, Yoon et al., 2001], allowing for TES arrays to be scaled to thousands of detectors with minimal wiring.

The MBAC TES thermistors are superconducting MoAu bi-layer devices with superconducting transitions tuned to $\sim$ 500 mK. The TES thermistors are patterned on 1.05 mm $\times$ 1.05 mm $\times$ 1.4 µm silicon absorbers which are implanted with phosphorous

[4]For the MBAC arrays, molybdenum nitride resistors manufactured at GSFC were used as shunt resistors. Typical values for R_{shunt} are 0.7 mΩ. The TES normal resistances were $\sim$ 25 mΩ.

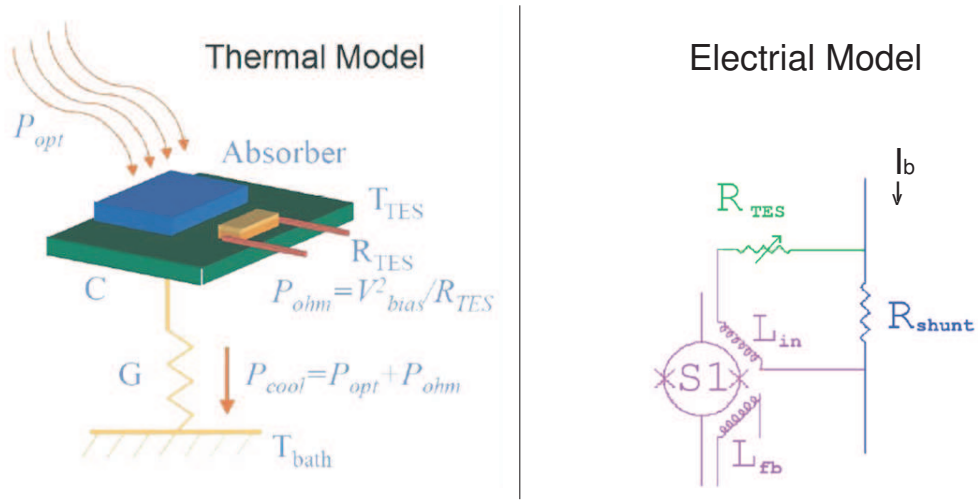

Figure 3.11 Simple thermal and electrical schematic of a single TES circuit. *Left*: A TES is implanted on an absorber with heat capacity C. It is connected to a heat sink bath, T_{bath} through a weak thermal link with conductance G. Incident optical power, P_{opt} raises the temperature of the absorber which causes an increase in the resistance of the TES. *Right*: The TES is voltage biased with $R_{shunt} \ll R_{TES}$. A change in resistance of the TES from incident optical power causes a changing current through an inductor L_{in}. The changing current produces a changing magnetic flux which is measured by the SQUID. A feedback inductor L_{fb} cancels the induced signal and keeps the SQUID linear on the V–ϕ and becomes our signal. Figures from D. Benford.

ions tuned to give the pixels the correct impedance for absorption at our frequencies. The sharp transition from normal to superconducting happens over a temperature range of $\sim 2\,\mathrm{mK}$, providing a steep R vs.T curve. The TES bolometers are fabricated on Si wafers in individual columns containing 32 detectors, with the bolometers suspended from the Si card by $4 \sim 1\,\mu\mathrm{m} \times 5\,\mu\mathrm{m}$ cross-section legs. These legs serve to both conduct electrical signal from the TES and also to set the conductance G to the temperature bath. The individual columns are then folded on these suspension legs so that the absorber and TES are perpendicular to the Si card. This pop-up folded design allows for close-packing of the stacked columns, producing a CCD-like array of bolometers. A 1×32 TES column is then cooled, tested, and characterized in a separate LHe dip-probe cryostat with the best columns being selected for insertion into the array. The chosen columns are then inserted into the array holder (see Section 3.2.4). Figure 3.12 shows the finished 32×32 145 GHz array. At the time of their deployment, these were the largest arrays of bolometers ever deployed. The design, fabrication, testing and characterization of the MBAC TES arrays have been the subject of several Ph.D theses and papers. Details on the TES parameters selected for ACT can be found in Marriage et al. [2006] and Marriage [2006]. The folding procedure, array assembly, and column pretesting can be found in Lau [2006]. Characterization and performance of the 145 GHz array can be found in Niemack et al. [2008] and Niemack [2008]. Unfortunately, noise properties of TES bolometers do not appear to follow a simple bolometer model and is the subject of ongoing investigation by the community. See Irwin and Hilton [2005] and Irwin [2006] for a complete description of TES bolometers and noise modeling. A bolometer model for the MBAC detectors can be found in Zhao et al. [2008].

To measure the output of a TES bolometer, an inductor, L_{in}, is placed in series

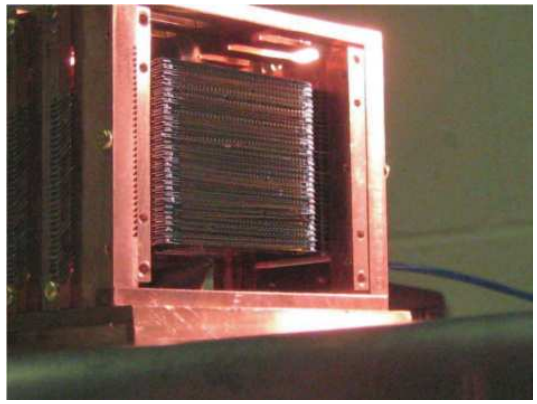

Figure 3.12 Photo of the 145 GHz 32 × 32 array before installation into MBAC. The individual columns (running horizontally in this photo) are stacked; a column contains 32 ∼ 1 mm square pixels. The finished array is ∼ 34 mm wide by 39 mm tall.

with the TES and coupled to a SQUID (Figure 3.11). The change in resistance in the TES induces a change in current through the inductor. The changing current produces a change in magnetic flux, ϕ, which is detected by the nearby SQUID. The SQUID voltage response to a changing magnetic flux is given by:

$$V = \frac{R}{2}(I^2 - [2I_c \cos(\pi\phi/\phi_0)]^2)^{\frac{1}{2}} \tag{3.3}$$

where R is the resistance of the Josephson junctions, I is the SQUID bias current, I_c is the critical current of the Josephson junctions, and ϕ_0 is the magnetic flux quantum[5] [Tinkham, 1996]. The individual bolometers are read out in a time-multiplexed fashion through SQUID multiplexers designed and provided to us from the National Institute of Standards and Technology (NIST) that are controlled and read out by the Multi-Channel Electronics (MCE) developed by the University of British Columbia. An electrical schematic is shown if Figure 3.13. Details of the MCE readout electronics can be found in Battistelli et al. [2008a] and Battistelli et al. [2008b] .

[5] $\phi_0 \equiv h/2e$ where h is Plank's constant and e is the charge of the electron.

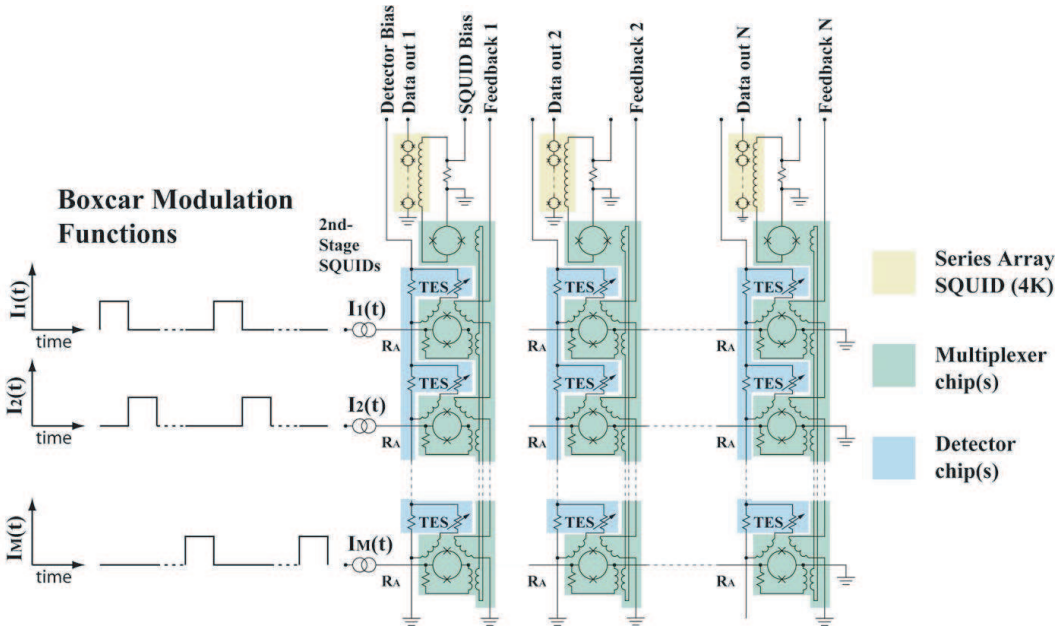

Figure 3.13 Schematic of the NIST multiplexing readout electronics. The readout consists of three stages of SQUIDs. Each TES is inductively coupled to a first stage SQUID (S1). Another inductor is coupled to the S1 SQUID loop. This inductor is one in a series of inductors running the length of a single detector column, forming an inductor loop, with inductors placed by each S1 coupling inductors in the column. The induction loop is coupled to a single second stage SQUID (S2) for each column and resides on a single multiplexing chip. When the S1 SQUIDs along a row are turned on, that row of detectors is read out. The S1 SQUIDs in other columns remain off, and contribute no signal to that column's series inductor loop. The 2nd stage SQUID inductively couples to an array of SQUIDs in series (SA) that amplify the signal before is exits the cryostat. The S1 and S2 SQUIDs reside on the multiplexing chip located near the detector columns at 300 mK, while the series array SQUIDs are located on the 4 K plate. The S2 SQUIDs are connected to the SA amplifier SQUIDs through NbTI superconducting wiring. Feedback inductors, controlled by a PI loop on the MCE, cancels the signal on each SQUID stage, keeping them linear along their V–ϕ curve (Equation 3.3). The S1 SQUIDs are connected in series along the rows and are turned on successively in time; one detector along each column is read out on each row in time. Multiplexing reduces the number of wires necessary to read out a 1024-pixel array from 2048 to 384. Figure courtesy of K. Irwin

3.4 Magnetic Shielding

The SQUID multiplexers (muxes) and amplifiers are sensitive to changing magnetic fields [Battistelli et al., 2008b]. They require magnetic shielding from both Earth's DC field and AC fields induced by the telescope motion through Earth's DC field and potential fields such as those generated from the telescope motors. The series array amplifiers are located outside of the optics tubes and are self-contained units enclosed within their own magnetic shielding. The SQUID muxes, however, are mounted on the silicon cards that make up each column in the detector array holder (see Figure 3.10 and Figure 3.8). Because of their proximity to the array it would be difficult to provide individual magnetic shielding. We therefore chose to surround them with as close to an "infinitely long cylinder" as possible. In that approximation, the effectiveness of the magnetic shielding for a single layer of shielding is given by:

$$A = (\mu/4)[1 - \left(\frac{R_i^2}{R_o^2}\right)] + 1\,, \tag{3.4}$$

where A is the DC attenuation, μ is the permeability of the shielding material, and R_i and R_o are the inner and outer radii of the shield.

Cryoperm-10[6] is an alloy with a high nickel concentration. Its composition coupled with a proprietary heat treatment give it increased permeability at cryogenic temperatures. To achieve the maximum attenuation, our shielding uses the thickest available Cryoperm, 1.5 mm. We also use multiple layers which, given sufficient spacing between them, approaches the limit of multiplicative increases in the field attenuation.

[6]Cryoperm is a trademark of Vacuumschmelze GmbH in Hanau, Germany
Local Distributor: Amuneal Manufactoring Corporation, 4737 Darrah St., Philadelphia, PA 19124, info@amuneal.com, (800)-755-9843.

Each of the three frequency channels has its own set of magnetic shielding. Because of the proximity of the 300 mK lens to the superconducting multiplexers, for a shield to have a length-to-diameter ratio of at least 4:1 (roughly the lower limit a shield can be treated as an infinite cylinder), it needed to enclose the 300 mK lens cell in addition to the more critical muxes. The length is limited by structures inside the main aluminum 4 K tube, mainly the 4 K to 1 K G-10 suspension (Figure 3.8). Outside of each tube, surrounding cryostat structures, mainly the sorption refrigerators, limits the size of the shields (see Figure 3.14). The final design features multiple layers of shielding: an upper layer that lines the inside of each 4 K tube down to where the tube attaches to the 4 K plate, a "through" layer that extends from the peak of the 4 K to 1 K G-10 suspension down beyond the rear of the 300 mK radiation shield, and two additional layers that surround the bottom half of each tube around the location of the muxes.

Each layer of shielding has different dimensions, ports, and tubulations, making it difficult to calculate the magnetic field attenuation at the SQUIDs analytically. Computer simulations using Maxwell[7] were employed to apply AC fields to the exact geometry of our shields. These simulations estimate the attenuation to be nearly 40 dB [Thornton et al., 2008].

Ports were laser cut in the shielding for the 1 K and 300 mK coldfingers and the NbTi cables connecting the detector backplanes to the series arrays (Figures 3.7 and 3.14). The mass of the magnetic shielding for each tube is approximately 10 kg.

[7]Maxwell is a product of Ansoft. Internet URL: http://www.ansoft.com.

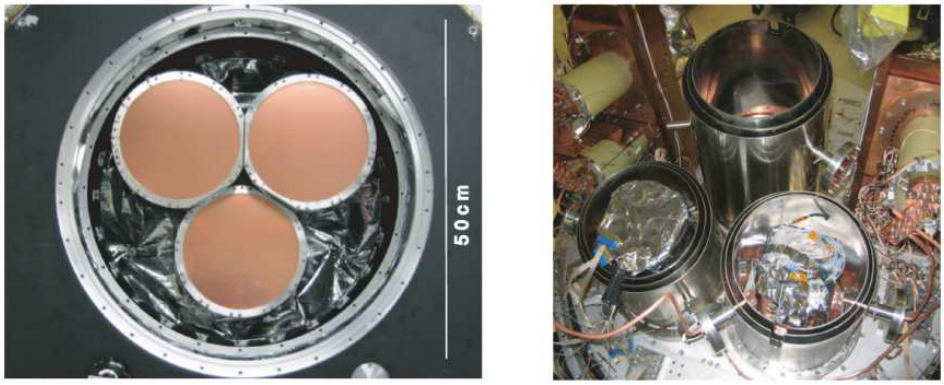

Figure 3.14 Assembled optics tubes. The left picture shows the three sets of optics as viewed from the front of the cryostat. The visible elements are the 4 K IR blocking filters. On the right are the exposed back ends of the tubes as viewed from the rear of the cryostat, where the triple layers of magnetic shielding and routed cold straps to the sorption refrigerators are visible.

3.5 Cryogenics and thermal design

The cryogenic design was dictated by many requirements. The site location precludes the use of liquid cryogens; the optics design requires multiple stages of cooling to reduce detector loading; the three detector arrays need to be maintained at 300 mK continuously for over 12 hours (the "hold time"), and the system must recycle in less than 12 hours[8]. The cryogenics must be stable when the telescope is scanning. In order to meet these requirements, MBAC incorporates a series of different types of cooling mechanisms including pulse-tube cryocoolers, closed-cycle ^{4}He-sorption refrigerators, and a closed-cycle ^{3}He-sorption refrigerator.

The primary cooling is achieved using two pulse tube cryocoolers[9]. The pulse tubes provide the first two stages of cooling, a 45 K first stage at a loading of 40 Watts and a 4.2 K second stage at 1 Watt. The next stage of cooling is accomplished using in-house

[8]The ACT observes from sunset to sunrise; daytime observations are not possible because solar heating of the telescope causes deformation of the telescope structure significantly increasing the $\sim$ 30 µm rms of the primary mirror [Hincks et al., 2008].

[9]Model PT-410 cryorefrigerator from Cryomech. For more information see www.cryomech.com.

built closed-cycle ^{4}He-sorption refrigerators [Devlin et al., 2004, Lau et al., 2006a]. The sorption refrigerators were measured to have $\sim$ 80 Joules cooling capacity and base temperatures of $\sim$ 670 mK. The final stage of cooling is accomplished using a in-house built ^{3}He-sorption refrigerator [Devlin et al., 2004]. A separate ^{4}He refrigerator is used to precool and back the ^{3}He refrigerator. The ^{3}He refrigerator was measured to have 5.8 Joules cooling capacity and a base temperature of 254 mK.

A schematic of the thermal connections in the cryostat is shown in Figure 3.15. The pulse tubes and sorption refrigerators are thermally arranged to provide two quasi-independent 4 K stages and two independent 1 K stages. In the first system, the pulse tube ("PT 1") is connected to the condenser plate of the ^{4}He backing refrigerator, condensing the helium gas in the refrigerator into liquid helium-4 collected in the evaporator when the charcoal in the sorption part of the refrigerator is heated. The charcoal sorption pump for the ^{4}He backing refrigerator is then cooled, the pressure in the refrigerator drops from $\sim$ 1 atmosphere to $< 10^{-5}$ torr and the evaporator is cooled to $\sim$ 700 mK by the evaporating ^{4}He. The evaporator plate (so called 1 K stage) of the ^{4}He backing refrigerator is connected to the condensing plate of the ^{3}He refrigerator, providing the cooling necessary to condense the ^{3}He gas into liquid collected in its evaporator. The charcoal is subsequently cooled and the evaporator of the ^{3}He refrigerator drops to $\sim$ 250 mK when unloaded. The ^{3}He evaporator is connected to the 0.3 K lenses, and 0.3 K filters ("lens cell") and most importantly the detector arrays. The second pulse tube ("PT 2") is connected to the ^{4}He optics refrigerator. Cycling and operation for this refrigerator is the same as for the other ^{4}He refrigerator. The evaporator for the ^{4}He optics refrigerator is connected to the 1 K lens cells for the 145 GHz and 220 GHz channels. The 280 GHz 1 K lens cell is cooled by the ^{4}He backing refrigerator.

Decoupling the 1 K stages of the two ^{4}He refrigerators has several advantages. Using a ^{4}He backing refrigerator provides more complete condensation of the ^{3}He gas, ensuring we get efficient recycling of the ^{3}He refrigerator. After the ^{3}He refrigerator is recycled, the ^{4}He backing refrigerator has enough capacity to stay cold for the duration of the ^{3}He hold time, reducing the overall parasitic load on the ^{3}He refrigerator and allowing for longer hold times and lower base temperatures at 300 mK. Having two separate pulse tube/sorption refrigerator systems also allows us to thermally recycle the refrigerator systems faster than with one.

The two refrigerator assemblies are mounted into the cyrostat on separate copper towers (Figure 3.19). These copper towers provide a rigid mechanical mount for the sorption refrigerators and also provide high thermal conductivity from the sorption refrigerators to the pulse tubes. The base of a copper tower is bolted to the 4 K plate (Figure 3.18), making the whole system mechanically robust enough to withstand the scanning motion of the telescope.

The system is cold until the liquid helium supply in the evaporator pots is exhausted. After this point, the charcoal is heated, releasing the gas and the condensing process is repeated. Various techniques were tried to minimize the recycling time while still maintaining complete condensation of liquid helium for maximum cooling capacity (hold time). We found that heating the charcoal pumps simultaneously, but cooling them sequentially was optimal; the key is to allow sufficient time after each charcoal cooling for the pulse tubes to recover to their base temperatures.

Table 3.4 lists the steps and wait times for the various recycling stages and Figure 3.16 plots the temperatures of the important components during a typical recycle. The recycling procedure is as follows: first, the three gas-gap heat switches that connect the charcoal pumps to the 4 K base plate are turned off and allowed to cool

for 10 minutes, thereby thermally isolating the charcoal pumps from the 4 K stage. Next, power is applied to all three charcoals, heating the ^{4}He refrigerator charcoals to 50 K and the ^{3}He charcoal to 30 K. The charcoals are held at these temperatures while the helium gas is released from the charcoal pumps and condensed into liquid in the evaporator pot. After the helium has condensed, the heat switch for the ^{4}He optics refrigerator is turned on and the charcoal cools from 50 K to 4 K. As the charcoal cools and begins pumping on the liquid helium, the pulse tubes rise in temperature from the excess load of cooling the charcoal, raising the condensing plate temperatures. If the other refrigerators were cooling at this time, there would be some loss in the amount of condensed liquid helium in the other sorption refrigerator. Lose of cooling capacity can be prevented by keeping the charcoals of the other two refrigerators warm to prevent the charcoal from absorbing the gas until the condenser comes back to its nominal temperature. Recycling efficiency is very sensitive to the condenser temperature when its temperature is near the boiling point of the gas at atmospheric pressure. After the pulse tubes have recovered to their base temperatures and the helium gas has recondensed, the heat switch is turned on to the ^{4}He backing refrigerator and its charcoal is cooled, again causing a rise in pulse-tube temperature. Until the backing refrigerator starts to cool, the ^{3}He charcoal is kept at 30 K to keep the gas released from its charcoal. When the backing refrigerator evaporator pot reaches $\sim$ 1 K the ^{3}He liquid has condensed and the ^{3}He charcoal is cooled, which pumps on the liquid ^{3}He and provides the 300 mK bath.

The recycling procedure is completely automated and can be controlled remotely. The total recycle time for all three sorption refrigerators is $\sim$ 6 hours. Over the course of a night, the ^{3}He refrigerator can have small temperature drifts. To prevent these drifts from affecting the detectors, we thermally regulate the temperature of

Table 3.4 The recycling of the helium sorption refrigerators is done sequentially in the following steps. The time listed is the wait time before starting the next step. Arrows show the $\sim$ starting and ending temperatures for the charcoals and evaporators. When the Char. Servo is On power is being applied to the charcoal to release helium gas. The heat switch is denoted by HS. When the HS is Off (On), the charcoal is isolated from (connected to) the pulse tube.

Cycle Step	Sorption Fridge	Char. Temp. [K]	Char. Servo	HS	Evap. Temp. [K]
1	^{4}He Optics	4	Off	Off	1
HS cool	^{4}He Backing	4	Off	Off	1
600 seconds	^{3}He Fridge	4	Off	Off	0.3
2	^{4}He Optics	$4 \rightarrow 50$	On	Off	$1 \rightarrow 4$
Release Gas	^{4}He Backing	$4 \rightarrow 50$	On	Off	$1 \rightarrow 4$
6000 seconds	^{3}He Fridge	$4 \rightarrow 30$	On	Off	$0.3 \rightarrow 4$
3	^{4}He Optics	$50 \rightarrow 4$	Off	On	$4 \rightarrow 1$
Pump ^{4}He Optics	^{4}He Backing	50	On	Off	4
6000 seconds	^{3}He Fridge	30	On	Off	4
4	^{4}He Optics	4	Off	On	1
Pump ^{4}He Backing	^{4}He Backing	$50 \rightarrow 4$	Off	On	$4 \rightarrow 1$
6000 seconds	^{3}He Fridge	30	On	Off	$4 \rightarrow 1$
5	^{4}He Optics	4	Off	On	1
Pump ^{3}He refrigerator	^{4}He Backing	4	Off	On	1
3600 seconds	^{3}He Fridge	$30 \rightarrow 4$	Off	On	$1 \rightarrow 0.3$
6	^{4}He Optics	4	Off	On	1
System Cold	^{4}He Backing	4	Off	On	1
Recycle Complete	^{3}He Fridge	4	Off	On	0.3

each detector stage with independent servos that consist of a resistor used as a heat source and a feedback loop run by the main acquisition program [Switzer et al., 2008].

3.5.1 Thermal Model

Because of the limited cooling capacity of the pulse-tube cryocoolers and sorption refrigerators, their operating temperatures are set by their loads. Loading also sets the length of time the sorption refrigerators remain cold before needing to be recycled.

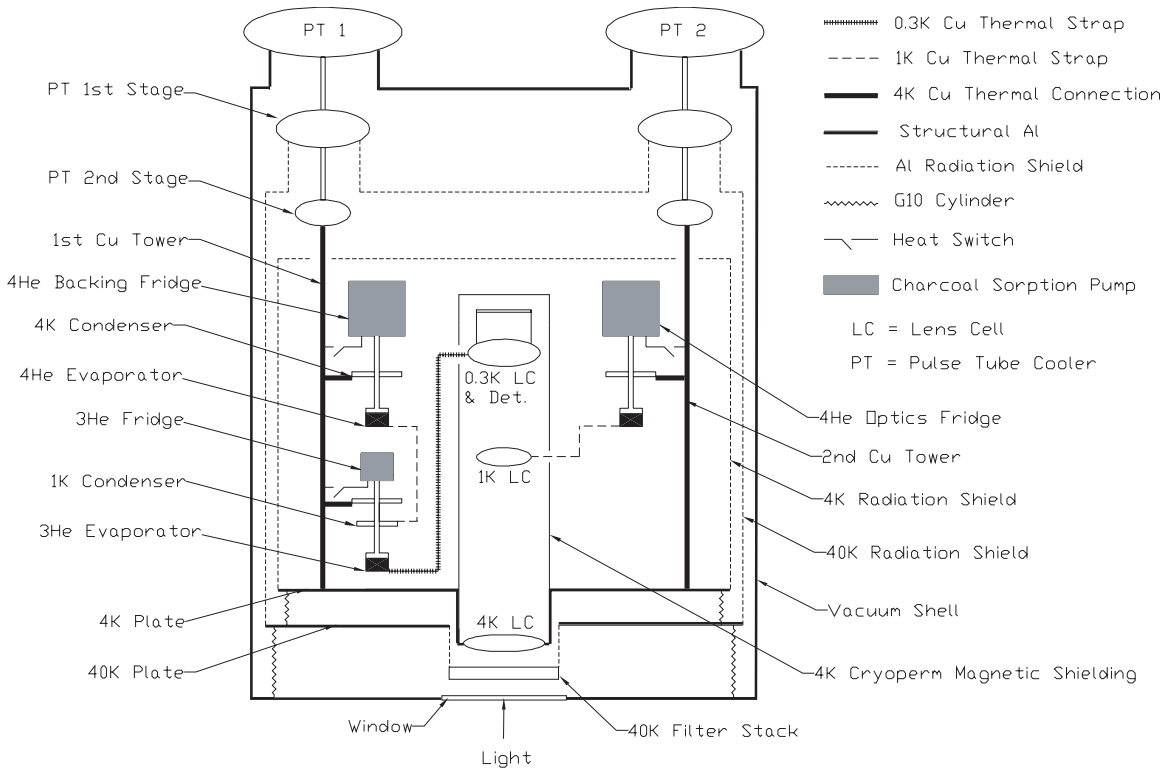

Figure 3.15 Schematic of the radiation shielding and thermal connections in MBAC. Only a single optics tube is shown, depicting the 145 and 220 GHz channels. The 280 GHz 1 K optics (not shown) are connected to and cooled by the ^{4}He backing refrigerator.

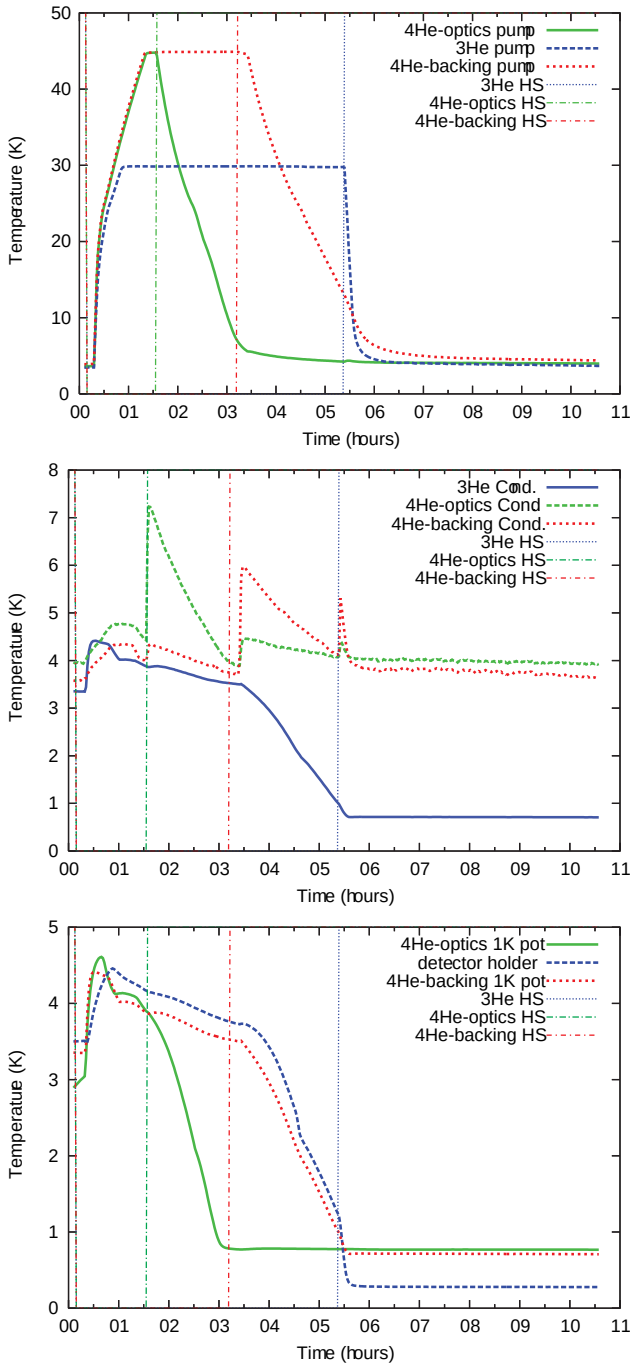

Figure 3.16 Temperatures of key stages during the recycling of the refrigerators. Vertical lines indicate when the gas-gap heat switches activate. The topmost plot shows the charcoal pump temperatures; the middle plot shows the condensation plate temperatures; the lowest plot shows the liquid evaporator pot temperatures. Figure made in collaboration with E. Switzer and J. Klein

During the design phase of the cryostat, a detailed thermal model for each temperature stage was developed so that sufficient refrigerator capacity and thermal lagging could be built into the cryostat to meet the desired hold times and temperatures. Loading arises from the deposition of power from a hotter stage onto a colder stage. Heat is transferred by conduction, radiation, and joule heating.

Structures at different temperatures are thermally isolated, but each temperature stage has some mechanical connection to stages at higher temperature. The conductive loading from these connections can be calculated by

$$P_{cond} = \int_{T_{low}}^{T_{high}} \frac{A}{l} \kappa(T) dT \tag{3.5}$$

where A is the cross sectional area of the connection, l is the effective path length between temperature stages along the connection, and $\kappa(T)$ is the thermal conductivity of the connecting material[10]. For structural supports, materials with high strength but low thermal conductivity are used. A balance must be reached that minimizes the cross-sectional area and maximizes the length while maintaining the necessary strength and rigidity. In the case of MBAC, there are many severe geometrical constraints. Wiring and cabling required materials with low thermal conductance but sufficient strength that they are not overly fragile. Most of our cables are made of manganin or constantin conductors (which can be made thinner than copper because they are stronger) supported in a web of Nomex (Nylon) made by Tekdata[11]. Typically, cabling is heat sunk at the next highest temperature.

The grey-body radiative power emmitted by a component of temperature T and

[10]Values for $\kappa(T)$ for most materials used in MBAC can be found at http://chile1.physics.upenn.edu/ec/calc.asp.

[11]Tekdata Interconnections, Ltd., Westport house, Federation Road, Bursalem Stoke On Trent, Staffordshire, ST6 4HY, UK, +44-1782-577677.

absorbed on a colder stage can be calculated using the Stephan-Boltzmann law,

$$P_{rad} = A\sigma\epsilon_{eff}T^4 \tag{3.6}$$

where A is the emitting surface area, ϵ_{eff} is the effective emissivity of the warm grey body multiplied by the absorbance of the colder surface, and σ is the the Stephan-Boltzmann constant. The radiative load is minimized by enclosing successive cold surfaces in light-tight radiation shields at the next highest temperature (see Figures 3.15 and 3.18). Exposed cold surfaces facing warmer ones are wrapped in ~ 30 layers of aluminized Mylar "super insulation" also known as MLI (Multi-Layer Insulation). The Mylar substrate of the MLI has low thermal conductivity and the thin aluminum sheets have high reflectivity which lowers the absorbance of photons onto the cold stage. Surfaces of optical elements, such as lenses and filters, obviously cannot be wrapped in this way. Therefore, IR-blocking filters are placed on the warm face of each optic up to and including the 4 K lens cell along the optical path, to limit emissive loading.

Joule heating is heat loss due to resistance to the moving particles that make up the electrical current. At many of the temperature stages, the heating loss in the wires from Joule heating is negligible. At the lowest temperature stages, NbTi superconducting wires are used, which have the benefits of high electrical conductivity (superconducting) hence no Joule heating, and low thermal conductivity (also because they are superconducting). The biasing of the arrays onto their superconducting transitions causes some Joule heating of the 300 mK stage, while pulsing of the calibration sources results in Joule heating of the 1 K stage.

Tables 3.5, 3.6, 3.7, and 3.8 list the calculated loading on each of the four cold

Table 3.5 Load analysis on the 40K stage. The number in parenthesis is the number of elements. The area over the length (A/l) is for the total for all elements.

Conductive Load	Material	A/l	T_{high} (K)	Load (W)
G-10 cylinder	G-10	16.4 mm	300	2.6
Detector wires (1500)	Copper	58 µm	300	7.3
Housekeeping wires (200)	Manganin	9.7 µm	300	0.04
Radiative Load	emissivity	A (m^2)	T (K)	Load (W)
Vacuum Shell	0.0009	4.6	300	1.9
Windows and Filters (3)	0.01	0.02	300	0.3
			Total	**12.2W**

temperature stages. A series of hold time and load curve tests were performed to verify the thermal model predictions for the three sorption refrigerators. Each refrigerator was installed in a no-load configuration, with the only connections coming from wiring for a single heater and thermometer. Several known applied loads were placed on the refrigerator, and the temperature recorded (Figure 3.17). Then, after recycling, the parasitic load of each refrigerator was measured by allowing the refrigerator to expire its liquid helium naturally. For the ^{4}He refrigerators, the parasitic load is dominated by superfluid helium leakage through an aperture up the stainless steel tube connecting the helium pot to the charcoal enclosure [Lau et al., 2006a]. The capacity was measured by applying a high power load to exhaust the liquid helium in a short time period ($\sim$ 2 hours) so as not to be biased by the parasitic load. The load curve allows us to compare measured temperatures in MBAC to the total loading on a temperature stage. By knowing the capacity and load, the hold time can be predicted.

Table 3.6 Load analysis on the 4 K stage. The number in parenthesis is the number of elements. The area over the length (A/l) is for the total for all elements.

Conductive Load	Material	A/l	T_{high} (K)	Load (mW)
G-10 cylinder	G-10	12.4 mm	50	124.0
Detector wires (1500)	Constantin	117.8 µm	50	50.7
Housekeeping wires (200)	Manganin	19.3 µm	50	4.3
Radiative Load	emissivity	A (m^2)	T (K)	Load (mW)
40K shield	0.10	3.8	50	134.0
Filters (3)	0.01	0.1	50	34.5
			Total	**347.5 mW**

Table 3.7 Load analysis on the 1 K stage. The number in parenthesis is the number of elements. The area over the length (A/l) is for the total for all elements.

Conductive Load	Material	A/l	T_{high} (K)	Load (µW)
Optics Tube supports	G-10	2.0 mm	6	619.5
Detector cables-type 1 (852)	NbTi	18.6µm	6	40.0
Detector wire cladding-1 (852)	CuNi	8.9µm	6	51.3
Detector cables-type 2 (426)	NbTi	37.2µm	6	79.9
Detector wire cladding-2 (426)	CuNi	8.9µm	6	51.0
Housekeeping wires (102)	Manganin	0.66µm	6	1.4
Coldfinger support (3)	Kapton	596µm	6	77.1
Wire Heatsink Clamp support	Kapton	2.4 mm	6	316.5
Radiative Load	emissivity	A (mm^2)	T (K)	Load (µW)
Croperm Magnetic Shields (3)	0.10	583.8	6	9.3
Filters (3)	0.10	27.4	6	0.4
Parasitic Load				231
			Total	**1477.4 µW**

Table 3.8 Load analysis on the 300 mK stage. The number in parenthesis is the number of elements. The area over the length (A/l) is for the total for all elements.

Conductive Load	Material	A/l	T_{high} (K)	Load (µW)
Array Suspension	Kevlar	1.6 mm	1.1	1.5
Mechancial Heatswitch support	Kevlar	0.52 mm	5	1.6
Detector cables-type 1 (852)	NbTi	18.6 µm	1.8	2.1
Detector wire cladding-1 (852)	CuNi	8.9 µm	1.8	14.7
Detector cables-type 2 (426)	NbTi	37.2 µm	1.8	4.1
Detector wire cladding-2 (426)	CuNi	8.9 µm	1.1	14.7
Housekeeping wires (26)	Manganin	0.66 µm	5	0.9
Coldfinger support (3)	Kapton	1.04mm	6	1.1
Radiative Load	emissivity	A (mm^2)	T (K)	Load (µW)
Croperm Magnetic Shields (3)	0.10	116.9	6	2.6
Optics Tube Shields (3)	1	116.9	1.1	< 0.1
Filters (3)	0.10	18.2	1.1	< 0.1
Joule Power				Load (µW)
Array Bias Power (3)				6.0
Array Temperature Servo(3)				7.7
Parasitic Load				4.6
			Total	**58.8 µW**

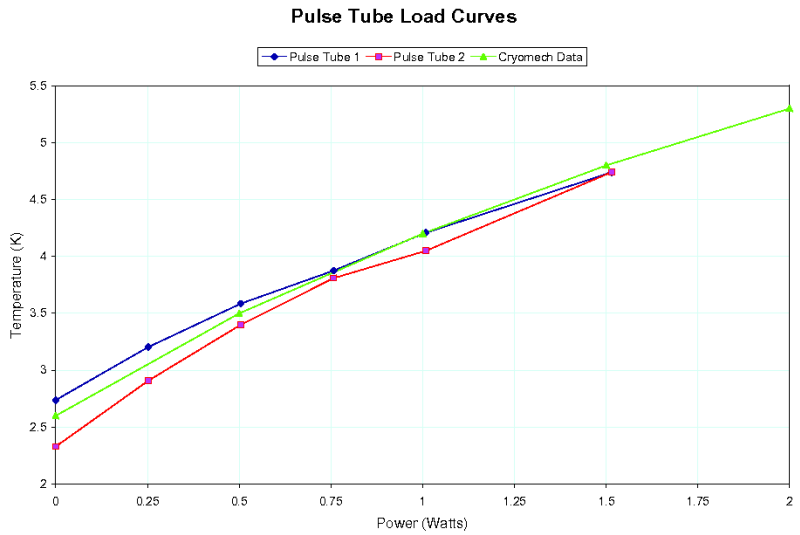

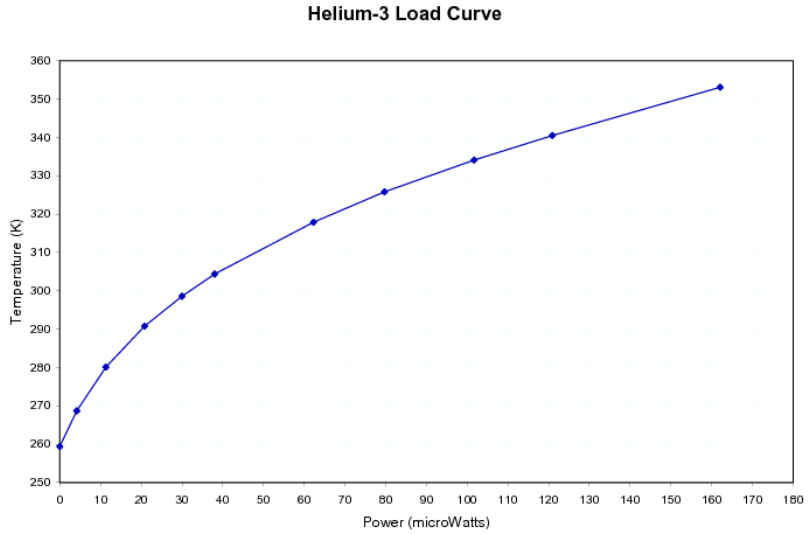

Figure 3.17 Load curves taken for the Pulse Tube 2nd stage (top) and ^{3}He sorption refrigerator (bottom).

3.5.2 Discussion and Performance

In the lab, we measured an 82 hour hold time for the ^{4}He optics refrigerator and a 48 hour hold time for the ^{3}He refrigerator with a single optics tube installed, which matched the thermal model prediction to 10%. Three things dominate the uncertainty of the thermal model: inexact measure of the upper temperature for conductance, poorly constrained thermal conductance numbers to cryogenic temperatures for certain materials, and estimates of emissivity for radiative loading. The 10% agreement gave confidence in the model parameters.

With MBAC on the telescope during the first observing season, a similar series of tests were performed to verify that the system was on track to meet the cryogenic needs with all three sets of optics installed. In the first observing season we did not heat sink the detector NbTi superconducting wires going to the array from the 4 K plate. It was discovered that the NbTi supreconducting wires could only be manufactured with a thin copper-nickel cladding. In the original thermal design budget, it was thought that these wires would be bare NbTi which has significantly less thermal conductivity than the copper-clad cable. The Cu-cladding of the wires now critically tied the loading on the 300 mK stage to the temperature of the 4 K base plate. The 4 K plate ran $\sim$ 1 K hotter on the telescope during the first season for reasons that are still not understood. The added load from these wires reduced the hold time of the ^{3}He refrigerator to $\approx$ 20 hours on the telescope. This did not affect the performance of the instrument during this first season, but posed a problem for operation with all three arrays.

Unfortunately, the length of the array cables are restricted to be no longer than 36 cm to prevent cable inductance from altering detector readout. To reduce the

load on the 0.3 K stage from these wires and decouple its dependence on the 4 K stage, we heat sank the NbTi detector cables. We also use smaller diameter wire for the cabling going to the second and third array (hence Detector cable type-1 and 2 in Tables 3.8 and 3.7). Heat sinking the wires at 1 K has improved the hold time of the 300 mK stage to greater than 18 hours with all three tubes installed. However, it has added a significant unplanned load on the 1 K stage that arises from the wires themselves and the retrofit mechanical structures needed to support the heat sink clamping mechanism. The ^{4}He optics refrigerator alone could no longer handle the additional load and remain cold for 12 hours. We therefore split the 1 K optics cooling between the two ^{4}He refrigerators: the optics refrigerator supporting the 145 and 220 GHz channels (both the 1 K optics and the heat sinking), and the ^{4}He backing refrigerator supporting the 280 GHz channel. In this configuration, we achieved a hold time longer than 14 hours. The ^{4}He optics-refrigerator now limits the hold time rather than the 300 mK stage[12]. Fourteen hours is sufficient to provide uninterrupted observations throughout a night's observations.

Pulse-tube coolers have their own limitations and disadvantages. The pulse tube pulses at a frequency of 1.4 Hz, resulting in an intrinsic 100 mK sine-wave temperature variation and an attendant mechanical vibration. Thermal oscillations associated with the pulse tube are not detectable at either the 1 K stage and 300 mK stage. The isolation is provided by the poor thermal connection between the 4 K stage and the evaporators of the refrigerator (by design to reduce parasitic loading). Furthermore, the connection between the copper towers and the 4K cold plate has a comparatively

[12]We define the hold time as the time from when the 300 mK stage reaches its operating point until any of the three sorption refrigerators exhausts its liquid helium supply. In the case when the ^{4}He refrigerator runs out first, the 1 K optics rise in temperature to the 4 K base plate temperature, as does the 300 mK stage from the added load through the Kevlar mounts. This induces a constant large thermal drift in the detector base temperature, preventing quality data from being acquired.

low thermal conductance while both the copper towers and the cold plate have very large thermal masses. Their combination acts as a low-pass filter on the temperature variations of the pulse tube as seen on the cold plate. Mechanical coupling at the pulse frequency is mitigated by using a compliant acoustically dead coupling consisting of several cords (~ 6 mm in diameter) of copper rope to attach the pulse-tube cryocoolers to the copper towers. We have not seen the pulse tube oscillations in any of the lens cell temperatures, nor in the detector data (i.e. no coupling through either conductance, radiation, or vibrations).

The pulse-tube coolers and He sorption refrigerators only operate at maximum capacity when they are close to vertical. ACT scans primarily at a constant elevation of 50.5°, but also looks at known sources such as planets for calibration and pointing purposes. We wanted the cryogenic system to perform through the entire range of telescope motion, 60° to 30.5° elevation, and so the refrigerators are mounted so that they are vertical when the telescope is pointed at 45° in elevation, near the middle of its range. Cryogenic tests have been performed with MBAC at both 60° and 30°. At these angles, there is little reduction in the performance of the pulse-tube coolers. We did measure a small (~ 0.1 mK/µW) reduction in the cooling ability of the ^{3}He refrigerator and a 8% reduction in total refrigerator capacity when the refrigerators are recycled at angles of 60° and 30°. These effects are relatively small and the MBAC is able to observe through the entire elevation range of ACT with minimal changes in the cryogenic performance.

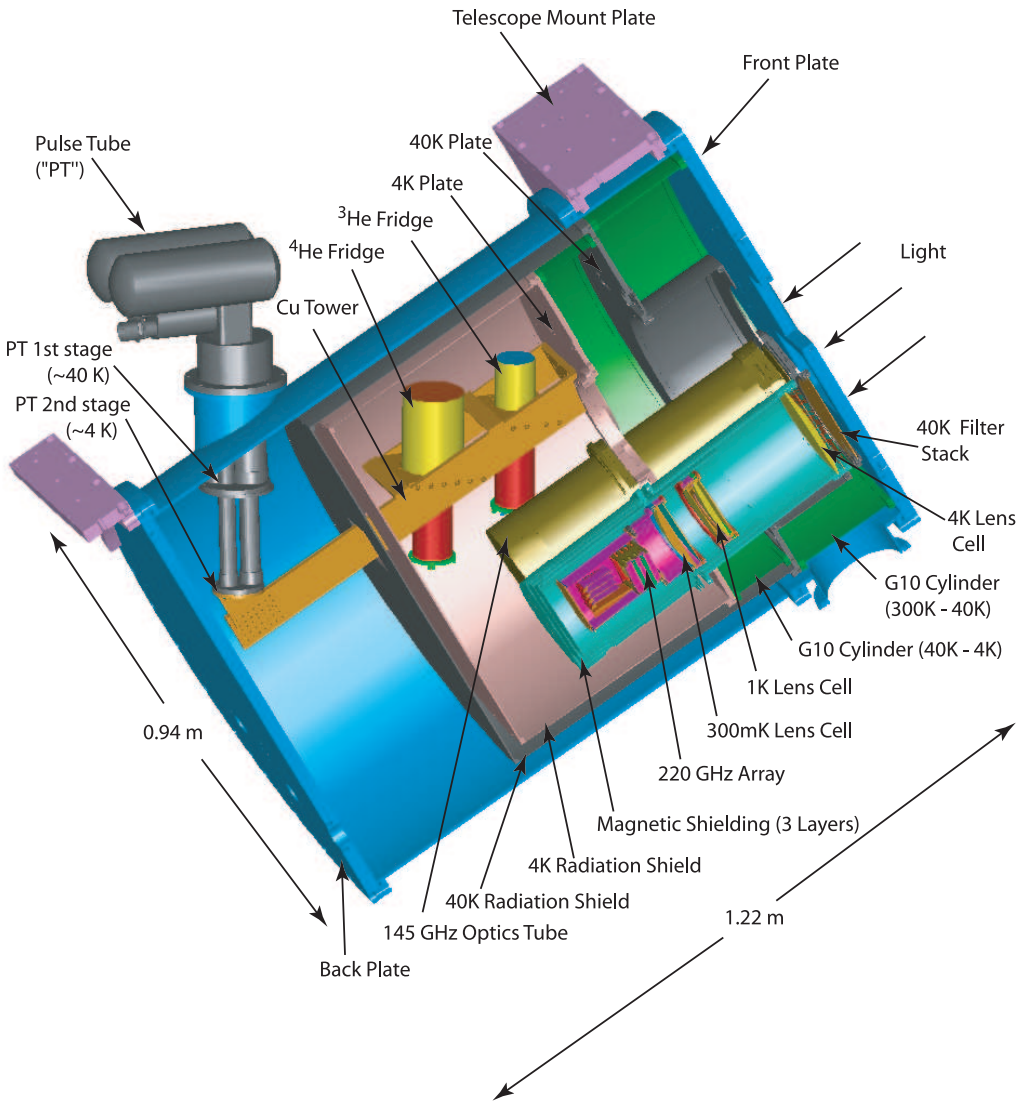

Figure 3.18 Cut away of the MBAC cryostat showing the location of the internal components. A cut away of the 220 GHz optics tube is also shown, giving the location of its lenses, filters, and array, which is similar for all three tubes. The 280 GHz optics tube mounts just above the 145 and 220 GHz optics tubes, but is removed for clarity. The connection of the first stage of the pulse tube and its radiation shielding to the 40 K plate is also omitted for clarity.

3.6 Cryostat Mechanical Design

The vacuum shell is a cylinder measuring 0.94 meters in diameter and 1.22 meters long made out of 6.35 mm (0.25 inch) thick aluminum. This shape was chosen because it is relatively easy to manufacture, fits in the allocated space, and has good strength to weight ratio. The shell diameter was dictated by the area of the focal plane, and the length by the cold optics that were needed to reimage the focus of the off-axis Gregorian ACT telescope. A cut away of the MBAC highlighting major internal components is shown in Figure 3.18. Due to the large size of the shell, we chose aluminum to keep the weight as low as possible. The front and back of the vacuum-shell cylinder are 25.4 mm (1 inch) thick aluminum plates. The front plate serves as the optical bench to which all of the cold optics are ultimately mounted. The front plate is also an integral part of the mounting of MBAC to ACT. This design allows all of the cold optics to be rigidly mounted to the telescope without relying on the rigidity of the cylindrical cryostat vacuum vessel.

Two additional aluminum plates are attached to the front plate via G-10 cylinders. The first plate ("40K plate") is cooled to $\sim$ 40 K. The second plate ("4K plate"), suspended from the 40K plate by G-10, is cooled to $\sim$ 4 K. A large radiation shield is attached to each plate. The shields are nested so that the outermost one (at 40 K) completely surrounds the inner one (at 4 K). The helium refrigerators and optics tubes are rigidly mounted to the 4K plate, and are located between the 4K plate and its corresponding radiation shield.

The vacuum shell is split about 200 mm back from the front plate. Removing the back tail of the cryostat decouples and removes the pulse-tube refrigerators from the optics and adsorption refrigerators, and allows easy access to the cold plates, optics,

and detectors (see Figure 3.19). All of the cabling for the thermometry, detectors, and the detector readout comes in through ports in the front vacuum shell section. These cables are heat sunk at both the 40K and at 4K plates. An advantage of this design is that it allows for access to all of the cabling, optics, and detectors without making or breaking any cable attachments.

3.6.1 Leak Rate

The cryogenic system needs to maintain a relatively high vacuum ($\lesssim$ 1 mPa ($\approx 10^{-5}$ torr)) in order to prevent gas conduction of heat between the various temperature stages. The system is initially evacuated, but over time, gas leaks in through the seals in the vacuum shell. The leak rate of gas through an O-ring seal can be approximated as

$$LR = 0.7FDPQ(1 - S)^2 \tag{3.7}$$

where LR is the leak rate in (std. cc/sec.), F is the permeability of the gas through the material at the operating temperature in (std. cc cm/cm^2 sec^{-1} bar^{-1}), D is the inner diameter of the O-ring in inches, P is the pressure differential across the seal in (lb/in^2), Q is a unitless factor that depends on the percent of the compression of the O-ring and whether a vacuum lubricant was used, and S is the ratio of the squeeze to the cross section of the O-ring [Parker O-Ring Handbook]. Equation 3.7 contains both metric and imperial units and the factor of 0.7 accounts for the mixed units. The equation is given in mixed units for convenience.

In MBAC, the leak rate is dominated by the three large 0.89 m-diameter O-rings which provide the seal at the front and back plates and the joint where the back tail attaches. The seals use 6.35 mm-diameter Buna-N O-rings with a small amount of

vacuum lubricant (GE silicone grease), an O-ring groove depth of 5.21 mm, a squeeze value S = 0.18, leading to a Q factor of ~ 0.73 for this amount of compression and a nitrogen gas[13] permeability at room temperature of 0.46 (std. cc cm/cm^2 sec^{-1}. bar^{-1}) [Parker O-Ring Handbook]. Using this value for Q, MBAC's leak rate is estimated to be $\mathrm{LR}_{estimate} = 3.5 \times 10^{-6}$ (std. cc/sec.). Several measurements with a helium-gas leak checker gave $\sim$ 2–9 $\times 10^{-6}$ (std. cc/sec.), in good agreement with the above approximation. Most of the gas that leaks in through the vacuum seals is not helium and freezes out on the cold surfaces at 40 K and 4 K. We also installed a charcoal getter on the 4 K stage containing activated carbon to trap gas that does not freeze out. From experience in the field, we have not seen any degradation in cryogenic performance from conduction due to gas leakage during the 6 months it was evacuated and cooled during the 2008 observing season.

3.6.2 Mechanical Alignment of MBAC to ACT

MBAC is mounted to ACT at the flange that joins the front plate to the vacuum cylinder providing an extremely rigid plane that can be precisely aligned with the optical axis of the telescope. This plane was used as the base for all optical elements inside MBAC, ensuring that the alignment was independent of variations in the cylindrical vacuum shell caused by pressure and temperature. The G-10 cylinders that connect 40 K and 4 K plates to the front plate are each pinned and bolted, creating a robust mechanical connection between the optics and front plate. The 25.4 mm thick front plate deforms slightly under vacuum and causes an offset in the location of the internal optics. The deflection as a function of radius of a clamped circular plate under a uniformly distributed load is given by

[13]Permeability of Buna-N for air was not available, so the permeability of nitrogen gas is used.

$$w(r) = \frac{Pr_0^4}{64D}\left(1 - (\frac{r}{r_0})^2\right)^2 \tag{3.8}$$

where P is the uniform loading, r_0 is the radius of the plate, and D is the bending of the plate defined as

$$D = \frac{Et^3}{12(1-\nu^2)} \tag{3.9}$$

where E is modulus of elasticity (Young's modulus or the ratio of the the stress to strain), ν is the Poisson's ratio (ratio of lateral strain to axial strain) of the plate material, and t is the thickness of the plate [Efunda Engineering Fundamentals]. Both Young's modulus and the Poission ratio are well know for 6061 wrought Al, and so it is straight forward to calculate the deflection of the MBAC front plate at the radius where the first G-10 cylinder bolts. For MBAC's front plate, we find a 150 µm shift of the the internal optics along the optical axis, well within the $\sim$ 5.1 mm tolerance requirement [Dicker, 2005].

Figure 3.20 shows the location of MBAC's front plate and telescope mounting plates in the primary mirror coordinate system, which translates the position of the internal cold optics to the rest of the telescope system. Figure 2.2 shows the mating of MBAC in the receiver cabin. The width of the receiver cabin is $\approx$ 4 meters. The MBAC enters though doors on the front of the receiver cabin (left side of Figure 2.2), and passes through the MBAC mounting structure whose width is $\approx$ 1 meter where it is then hoisted and bolted into place. Once the cryostat is bolted into the telescope receiver cabin, the laser tracker (Section 2.2) is used to locate the front plate in relation to the primary mirror. Table 3.9 lists the location of the window center and the three fiducial points used by the laser ranger to align MBAC. The cryostat is attached to the telescope receiver cabin on a mount that has adjustment

Table 3.9 Coordinates of the MBAC telescope mounts, cryostat window center, and fiducial points on the MBAC front plate in the ACT Gregorian coordinate system as shown in Figure 3.20. SMR (Spherically Mounted Retro-reflector) locations refer to the center of the 1.5 inch (38.1 mm) SMR when mounted on a pin-nest inserted in the fiducial's 0.250 inch (6.35 mm) hole drilled in the window plate mounted in the front flange. The pin-nest moves the center of the SMR and additional 0.25 inch (6.35 mm) perpendicular to the plane of the flange. The total distance of the point of reflection is 1 inch (25.4 mm) from the surface of the front plate. Numbers in the table are compensated for the angle between the front plate and the telescope's coordinate system. SMR location positions are used by the laser tracker when measuring in "uncompensated" mode.

	X	Y	Z
Telescope Mount Plate Front	$\pm$381.0 mm	519.0 mm	-1729.6 mm
Telescope Mount Plate Back	$\pm$381.0 mm	586.9 mm	-1686.9 mm
Cryostat Window Center	0.0 mm	-24.5 mm	-1729.6 mm
Fiducial 1	-206.5 mm	106.4 mm	1776.0 mm
SMR location	-206.5 mm	97.9 mm	1800.0 mm
Fiducial 2	206.5 mm	106.4 mm	1776.0 mm
SMR location	206.5 mm	97.9 mm	1800.0 mm
Fiducial 3	0.0 mm	-257.5 mm	1647.0 mm
SMR location	0.0 mm	-266.0 mm	1670.9 mm

in all three dimensions (though the adjustment screws do not move the receiver along the orthogonal directions). This system provides a way to accurately align the cold optics to the telescope and enables the optics to move in concert with the telescope as it scans.

3.7 Mechanical Tests of the Receiver

Prior to deployment, several mechanical tests on the MBAC receiver were performed. One of these tests measured the strength and stiffness of the system of stacked G-10 cylinders that provides support and thermal insulation of the 40 K, 4 K, 1 K and ultimately the 300 mK optics and their mechanical supports (Figure 3.18).

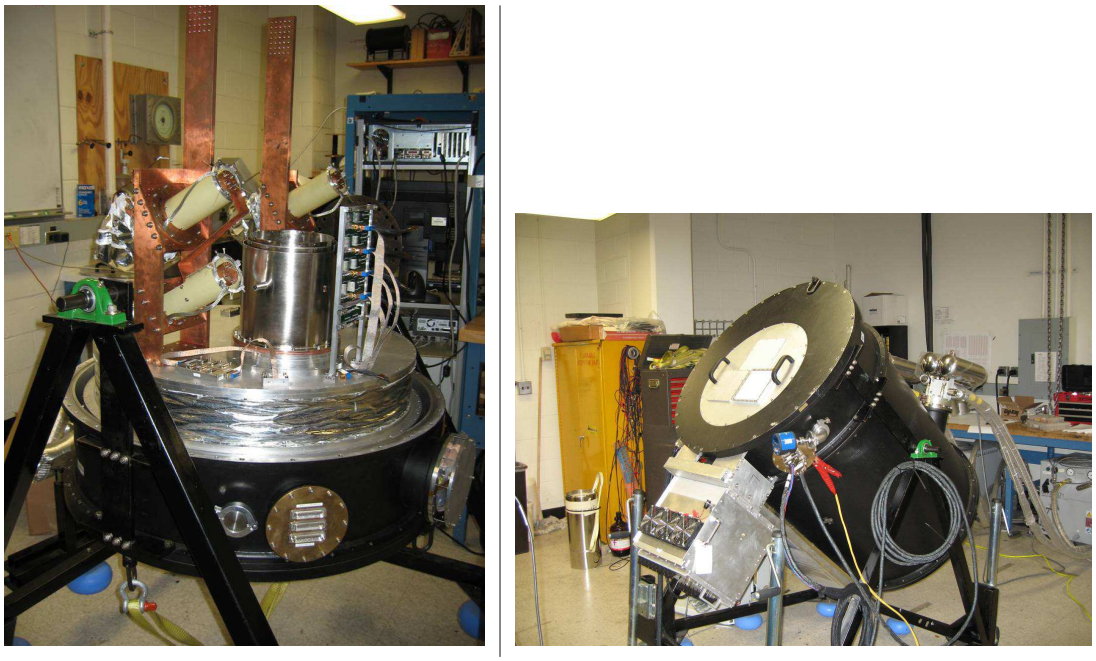

Figure 3.19 Left Panel: Picture of the MBAC open. The vacuum shell, pulse tubes and the two radiation shields have been removed, exposing the large (4600 cm^2) 4K plate. The three sorption refrigerators (G-10 cylinders inclined at $\sim 45°$) are mounted on the two vertical copper bars which in turn are attached to the 4K plate. The Cryoperm magnetic shield (silver vertical cylinder) surrounds the 145 GHz optics tube which is rigidly attached to the 4K plate. Right Panel: Picture of the MBAC closed. The receiver is shown at the approximate observing angle. The pulse tubes are mounted in the MBAC so that they are close to horizontal during normal operation. Light enters the cryostat through the three rectangular windows located between the handles that are removed during observations. The 145 GHz UHMWPE window is installed (lower-right window) (see Sec. 3.1.1). The total volume is 700 liters and the total mass is 530 kg. The MCE readout electronics (there are three, but only one is in place in this photo) are bolted to the vacuum shell through a mounting plate, forming a RF seal.

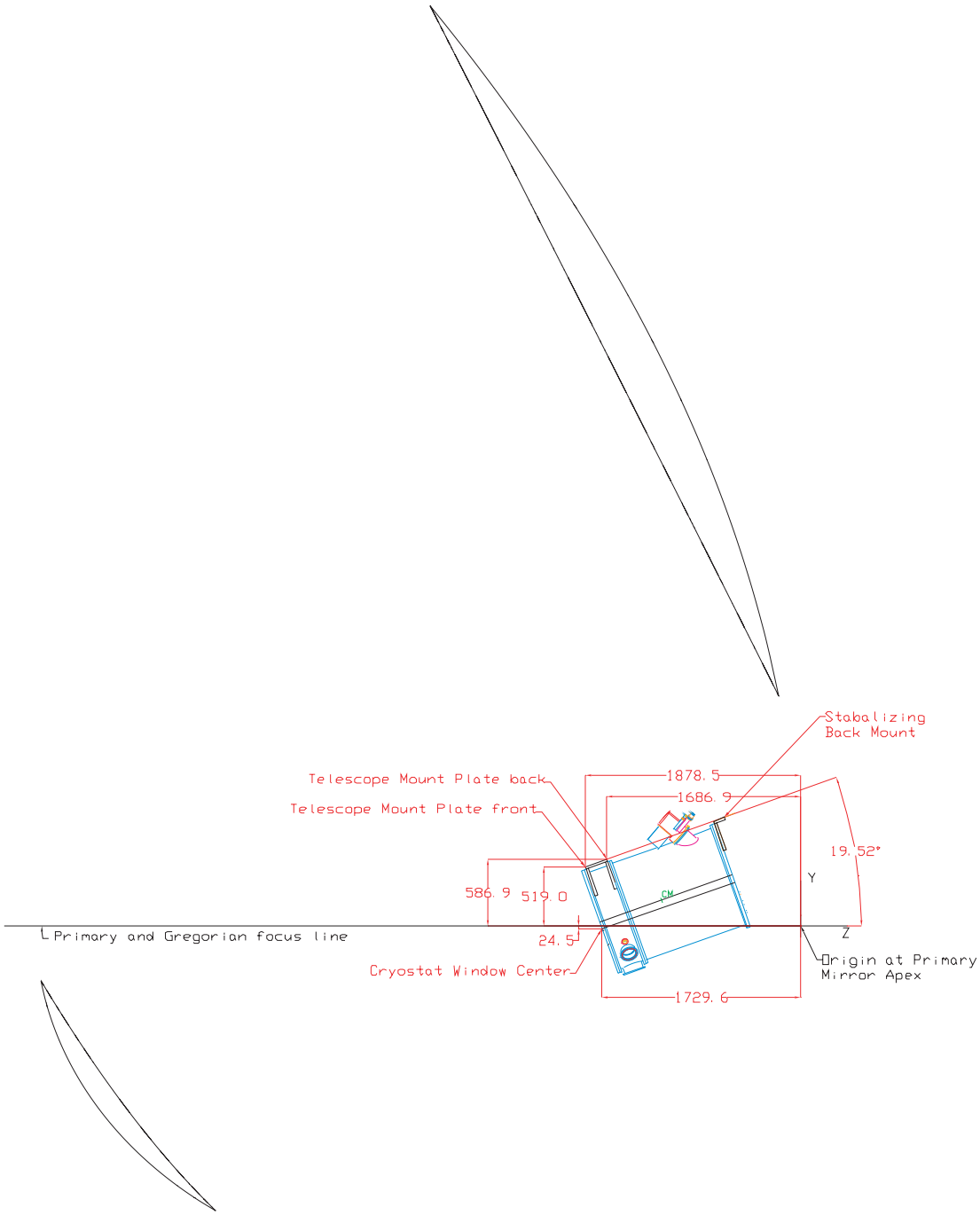

Figure 3.20 Placement of MBAC in the ACT Gregorian optics coordinate system. The location of the window center is measured with a laser ranger. Placing the front plate of MBAC's vacuum cylinder locates all the cold optics including the detectors in their fiducial positions.

We calculated the total mass connected to the 4K plate to be $\sim$ 120 kg providing 11 N-m torque at the center of mass and observing angle of the telescope. We estimated the telescope acceleration at 0.3 g, increasing the estimated torque on the system to 14 N-m. We hung 180 kg from the 4K plate at a moment arm to impart 22 N-m torque onto the two stacked G-10 cylinders. There was an initial deflection of 280 µm but no sign of buckling of the cylinders was observed. We left the mass connected and continued to monitor the deflection to test for creep. After two days, the deflection increased by 20 µm; longer periods resulted in no further deflections. We conclude that the stacked G-10 cylinders are strong enough to withstand the telescope scan motion and provide a very stable and rigid system for mounting the optics and helium sorption refrigerators.

Several mechanical tests on prototype subassemblies were conducted prior to mounting the final lenses and detectors. A major concern was that the 4 K to 1 K G-10 suspension would either not support or flex beyond optical tolerances under the weight of the attached 1K and 300 mK assemblies. We cantilevered a 9 kg mass (roughly twice the 300 mK mass) from a 0.38 mm thick prototype suspension. Under this load, the initial deflection was approximately 100 µm, and approached 130 µm after one week. For comparison, the decenter tolerance of the 1K lens is approximately 2 mm. The final suspension deflected less than 30 µm under the same load during the same time period.

Another mechanical concern was that the Kevlar suspension would not support the load of the 300 mK assembly. Tests of Kevlar of various thicknesses showed that 0.030 inch (0.75 mm) Kevlar works (and provides a factor of safety of about two). We questioned whether the suspension would sag or distort under cooling (Kevlar has a negative coefficient of thermal expansion). A flat mirror was mounted at the location

of the third lens which the reader will recall is mounted at the front of the 300 mK structure. A laser mounted on the front plate of the cryostat projected a beam through a temporary quartz window (also on the front plate of the cryostat), to the Kevlar suspension, where it reflected off the mirror and back outside of the cryostat onto a target. The long path length ($\sim$ 1.5 m) made the measurement sensitive to any deflection $\gtrsim$ 2.5 arcminute, considerably better than the $\approx 1.1^\circ$ tolerance requirement [Dicker, 2005]. There was no detectable movement of the Kevlar mount as it was cooled from ambient temperature to approximately 10 K, at which point the test was concluded.

Chapter 4

First Year Observations

The first observations with MBAC on ACT began in October 2007. The modular mechanical optics design (see Section 3.2) allowed for MBAC to be deployed in stages. For the first year, MBAC was deployed with only the 145 GHz bolometer array installed. MBAC arrived on site on 1 October 2007. Prior to shipping, the optics tube, pulse-tube cryocoolers, and 300 mK stage (including the bolometer array) were removed due to concerns over potential vibrational damage during shipping. Additional bracing and padding were also installed inside MBAC for protection during shipping. The pulse tubes and optics tubes were shipped in custom boxes and the 300 mK assembly was hand carried on a flight from North America. The receiver and all its internal components arrived undamaged.

The receiver reassembly is performed on site in the workshop container, and takes $\sim$ 10 days, at which point a complete electrical continuity check on the array is performed. The pulse-tube coolers are tested separately in a cryostat that is designed to be cooled rapidly by the pulse tubes in less than 1 day. Load curves are taken on each pulse tube to verify that they were not damaged in shipping. The completely

reassembled receiver is then evacuated, leak checked, and installed on the telescope. Evacuation takes about 2 days. Once installed, the detectors are cooled to $\sim 300\,\mathrm{mK}$, which takes another ~ 7 days. Figure 4.1 shows a picture of MBAC in the workshop container prior to installing and a picture of MBAC being installed in the telescope receiver cabin.

MBAC had first light on ACT on 22 October 2007 when the planet Venus was observed successfully. First light was followed by a commissioning period during which the receiver was characterized: detector time constants were measured with an optical chopper, the internal calibration source was setup and tested, the detector bias were optimized for telescope loading conditions, the performance of the cryogenic cooling systems were studied under different scanning conditions, and the final alignment of the primary and secondary mirrors was completed. Several targeted observations of planets were also carried out to determine the offset between the mm-wave beam on the sky and the telescope encoder readings. Dedicated CMB science observations began on 15 November 2007 when the final panel alignment was completed. Observations continued until an elevation motor broke on 14 December 2007, preventing telescope motion and ending observations. Fortunately, this was just about the scheduled time for when the receiver was to be brought back to North America for installation of the 220 and 280 GHz arrays, thus there was only minor shortening of the 2007 observing season that resulted from this failure.

During normal observations, all acquisition and control of the telescope is automated. A schedule file is generated daily to control data acquisition, telescope motion, and such housekeeping chores as recycling the fridges. Recycling of the fridges occurs during the day when heating of the telescope by the Sun causes the primary to lose its shape, preventing useful observations. Observations typically start at sunset and

Figure 4.1 Pictures of MBAC being installed on the telescope. *Left*: MBAC is reassembled in the workshop container upon arrival at site. Reassembly takes approximately 10 days. After reassembly, it is placed on a custom designed cart to allow installation in the telescope. The receiver and cart are lifted into the back of a pick-up truckbed by the yellow boom crane. The telescope outer ground shield is in the background on the left. *Right*: MBAC is driven through a door in the ground screen and hoisted a few feet manually with a chain fall attached to an I-beam before it is lifted the rest of the way by moving the telescope from 30.5° to 60° where the floor of the receiver cabin is level. MBAC and its cart are then rolled into the receiver cabin along rails before being lifted and bolted into the mounting structure using three come-alongs for lifting. In 2007, it took 3 weeks from MBAC's arrival on site to first light.

begin with setting the detector biases and tuning up the SQUID multiplexers. Slight changes in background loading, due either to atmospheric or to cryogenic causes, can change optimal biases and setpoints [Niemack, 2008]. Due to these effects, the detectors and their readout SQUIDs need to be rebiased and retuned daily after recycling. Biasing and tuning the detectors is relatively efficient and takes $\sim$ 15 minutes. The last step before starting observations entails moving the telescope through a large range of azimuth positions to warm up the motors and spread grease over the gears. Observations continued through sunrise. A typical observing period is 12 hours.

We observed two cross linked regions in 2007, a "Southern field" centered at a declination of $\sim$ -53° spanning right ascensions (RA) of approximately 70°–170°, and an "Equatorial field" centered at a declination of $\sim$ 0° spanning 25°-175°. All field observations were done at a constant elevation of 50.5°. The scan size was $\pm$ 2.5° with a speed of 1°/second. The ACT survey regions with overlapping data sets are shown in Figure 4.2. Observation-time weighted maps containing both rising and setting data for the fields are shown in Figure 4.3. The two extragalactic fields were chosen to minimize the time spent observing the Galaxy while maximizing overlap with existing data sets and cross linking. The Equatorial strip has poor coverage, due in part to telescope malfunctions during observations of this region. The Galaxy begins to contaminate the Southern field beginning at RA of 120° continuing through to 170°. We have focused our analysis on the $\sim$ 100 square-degree extragalactic region from RA of 75–120° in the Southern field. Initial analysis from planets indicates that the detectors sensitivity is $\sim 1\,\mathrm{mK}\,\sqrt{s}$. From this and the weight map, we expect to achieve $\sim$ 35–50 µK/map pixel in this 100 square degree field.

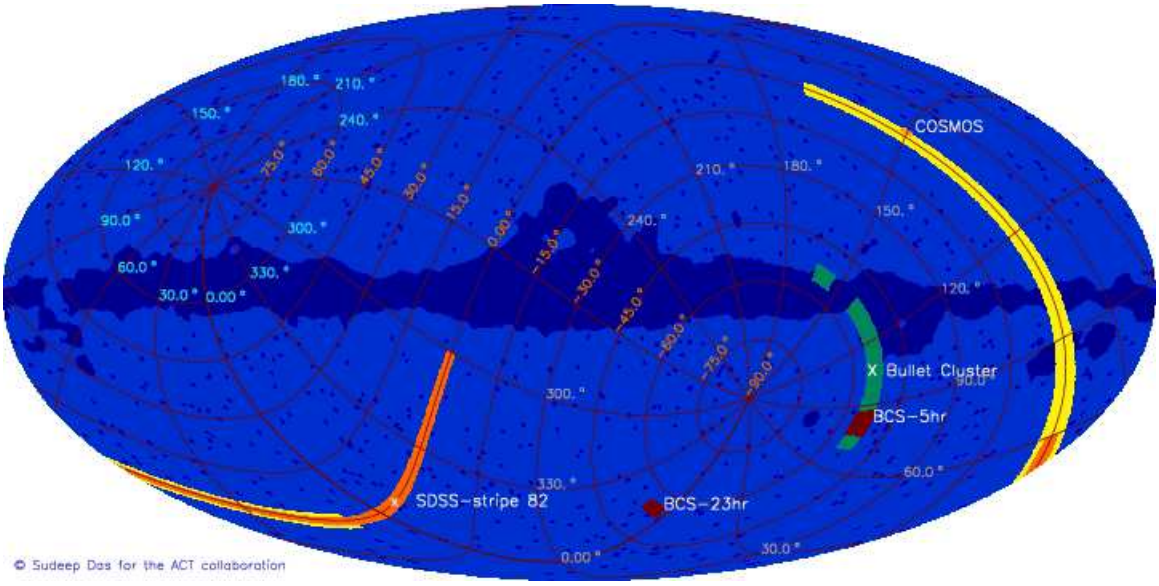

Figure 4.2 ACT sky coverage during the 2007 observing season, showing overlap with existing experiments. ACT scanned two cross-linked fields about the south celestial pole. The Southern field is shown in green and the Equatorial field in yellow. Also shown is overlap with Sloan Digital Sky Survey stripe 82 (SDSS in orange) and the Blanco Cosmology Field (BCS in red). These fields were chosen to minimize time spent in the Galaxy and maximize cross linking and overlap with existing datasets. Figure made in collaboration with S. Das.

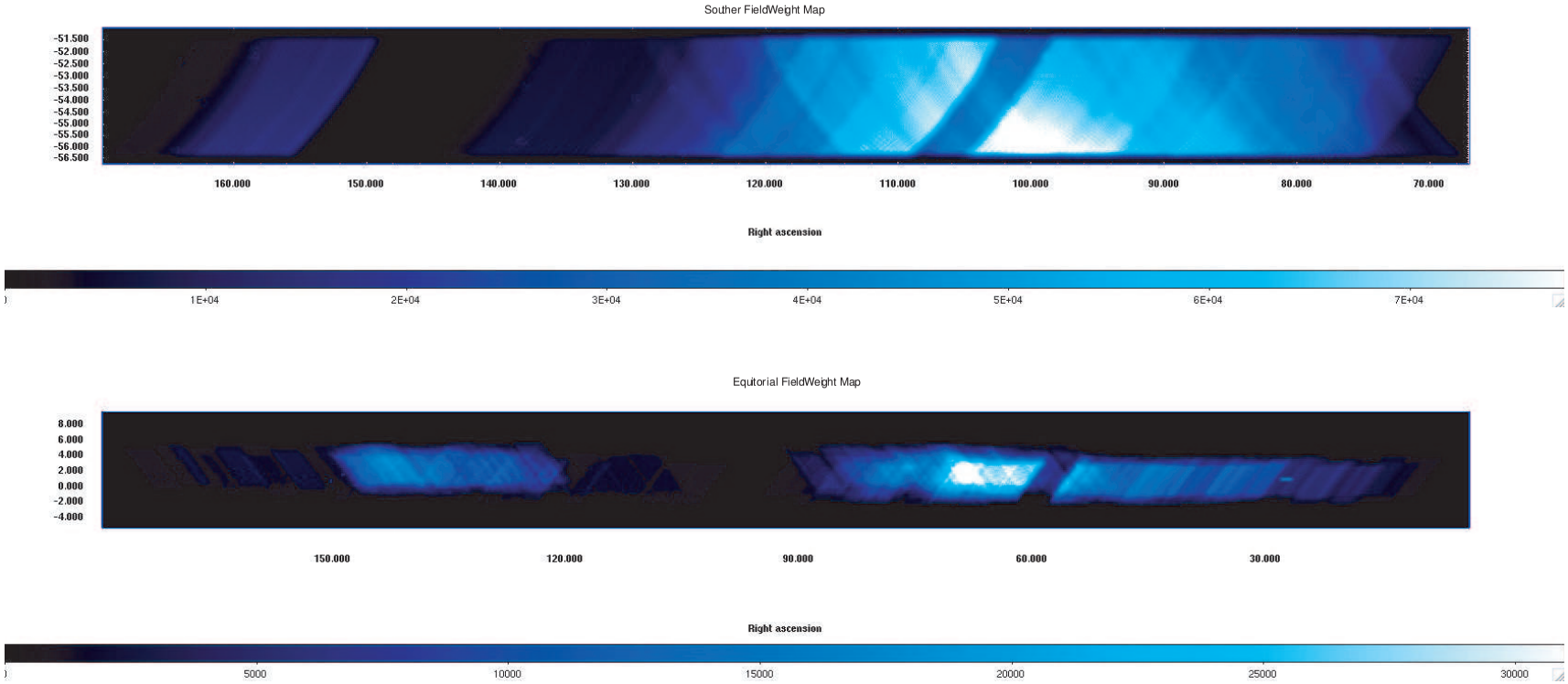

Figure 4.3 Sky coverage with pixel weight maps for the 2007 observing season. The x-axis is right ascension, the y-axis is declination, both in degrees. *Top*: Hit map and coverage for the Southern field. *Bottom*: Hit map and coverage for the Equatorial field. Figure courtesy of T. Marriage and S. Das.

Chapter 5

Data Analysis

One of the most time-consuming tasks of a scanning bolometer-based experiment such as ACT is to develop the data analysis pipeline. Significant analysis is required to transform the detector's time streams into maps suitable for scientific interpretation. At the time of this writing, the ACT analysis pipeline is still actively being worked on for the 2007 observing season, while simultaneously being built up to incorporate the 2008 data set. Here I present an overview of the analysis in its present form, including the storage and processing of the data, removal of unwanted detector artifacts, calibrating the detectors, and map production. Analysis of the 145 GHz beam from the 2007 observing season is also presented. Complete survey maps, cluster catalogs, and cosmological analysis will be presented in future publications.

5.1 Detector Cleaning and Cuts

The data time streams of each array consisting of 1024 individual bolometer channels sampled at $\approx 400\,\mathrm{Hz}$ are recorded on three dedicated computers, one per array. Each is stored in a file called a TOD-frame file. TOD stands for Time-Ordered Data,

and frame refers to the fact that the data from the detectors are recorded in the order they are read; data from an individual detector repeats every 4400 bytes. Housekeeping data such as the position of the telescope, temperatures of the primary and secondary, etc, and data related to the health of the cryostat (receiver) including cryogenic temperatures, cryogenic heater controls, etc, are stored on a fourth computer. A new file is created at the beginning of each observation and terminated after 15 minutes ($\sim$ 1.6 GB per array). At the end of each 15 minute interval, a new file is opened and the data writing is continued without interruption. Each file is named for the c-time when the observation started. The 15 minute segments are given sequence numbers that are appended to the filename as an extension. Segmenting the data into 15 minute chunks keeps the size of a single TOD file small enough that it can be quickly loaded onto a standard computer for quick analysis. Additionally, if a file is corrupted only a single 15 minute segment is lost.

In realtime, the data from all four computers (in the first season, we only had two computers, one for the 145 GHz array and one for the housekeeping) are merged on a fifth computer that stores the TODs as a collection of approximately 3500 files (one for each source: bolometer, thermometer, encoder, etc.) in a directory that is created each time an acquisition session is started or the telescope is repointed for another reason. The directory is named with the same c-time as the original TOD-frame files. Merging is kept synchronized by a frame word that is created by a synchronization box and is written into each of the time streams (three arrays and one housekeeping). Each of the merged TOD files contains data from a single source (bolometer, encoder, temperature sensor,etc.), but time synchronous data is located at the same position in each of the 3500 or so files. The data (both raw and merged) are stored locally at the site on hard drives housed in pressurized Al cases to prevent hard-drive failure at

altitude.

The data (both raw and merged) are transferred off the mountain via a microwave data link (Section 2.3) where they are stored on a RAID file system on a dedicated computer in our base in San Pedro. From there, the data are copied to transport disks that are subsequently hand carried to North America about every two weeks. The data rate of the final, merged product for one array is 70 GB/day[1]. We also keep the un-merged, raw data products for insurance, yielding around 140 GB/day total. After arrival in North America, the data are copied to a 16-processor RAID-array computer in Princeton, NJ which serves as the data pipeline host and main workstation. The original transport disks are kept as a backup of the original data set.

The cleaning and cuts pipeline involves several steps performed on the TOD prior to projecting into a map. The data from all detectors are processed simultaneously for each 15 minute long TOD file. Unless otherwise specified, a TOD below refers to a 15 minute TOD file. As many of the steps in the process are computationally intensive, the data are processed once and the results stored in a depot.

The first three steps remove the mean, a slope, and the effects of a low-pass electronic anti-aliasing filter from the TOD. The signal is modulated by scanning the telescope (including the detectors in MBAC) at 1° per second in azimuth with a peak-to-peak amplitude of 5°. At our observing angle of 50.5° a diffraction-limited beam at 280 GHz ($\approx$ 0.8 arcseconds) is on a region of sky for $\approx$ 0.02 seconds or 50 Hz. We remove the DC level by subtracting the mean from the detector. The DC level is

[1]In the second observing season, a lossless compression routine has been implemented which reduces the data rate to $\sim$ 30–35 GB per array per day for the un-merged TOD, and equivalent size for the merged TOD, 4 GB per day for the Housekeeping data for a total of about $\sim$ 210 GB per day for everything.

determined only by the arbitrary biasing point of the SQUID readout (described in Section 3.3); removing it does not affect the cosmological signal. Next, the data are detrended by removing a line running between an average of 1000 samples at each end of the 15 minute file. We believe the major cause of this trend is atmospheric variation. Removal of the trend has a negligible effect on the cosmological signal that has a period much shorter than 15 minutes. During data acquisition, a low-pass electronic Butterworth filter (f_{3dB} of $\approx 120\,\mathrm{Hz}$) is applied in the readout electronics to prevent aliasing of high-frequency noise into the time stream. The downside is the Butterworth gives a pointing offset whose sign is dependent on scan direction. Deconvolving the Butterworth with the TOD removes the pointing offset without significantly adding to the noise. After deconvolution, we recover signal to a frequency of 200 Hz, well beyond the source crossing time (effectively 50 Hz) of a beam.

Several detectors show no response to sky signal. During TES fabrication and assembly some detector failure is expected. Typically, these detectors were known to be dead from prior measurements. These constant-signal detectors are therefore removed from the data. During the first season, there were ~ 125 dead detectors. The next steps in the pipeline remove detectors which fall outside of certain cut limits.

The individual detector time constants were measured using an optical chopping wheel, where the time constant is defined as the detector f_{3dB} point from a single-pole filter fit to the Fourier transform of the chopping data. The average detector time constants were $\sim 90\,\mathrm{Hz}$. The detector time constant acts as a low-pass filter on the sky signal during scanning. A study done by Niemack [2008] found that detectors with time constants $\leq 50\,\mathrm{Hz}$ would reduce the detector response to a point source by more than 4% given the ACT scan speed of $1^\circ/\mathrm{s}$. Ideally, this time constant filter function could be deconvolved from the data as is done with to the electronic

filter. Unfortunately, the time constants of TES bolometers change under different loading conditions [Niemack, 2008]. Two avenues are currently being explored to measure the bolometer time constants repeatedly during the course of observations. The first involves measuring the shift in the peak response to planets in left-going and right-going scans. The second involves measuring the roll-off to an electrical impulse. These procedures are still being developed and checked with the optically-measured data. Therefore, detectors with optical time constant less than 50 Hz are cut from the data; this cut removes ≈ 50 detectors.

Three bias lines are used to bias the whole array of detectors onto their superconducting to normal transition. The high-uniformity of the physical properties of the detectors in the array, combined with negative electro-thermal feedback, mean that most detectors can be properly biased using as few as three biases. Obviously, detectors with too high a bias value are normal and too low a bias value remain superconducting. These detectors are not sensitive thermistors. Furthermore, detectors biased low or high on their transition can have nonlinear responsivities and are often unstable. Lab tests indicate that detectors with $R_{TES}/R_n \leq 0.2$ or $R_{TES}/R_n \geq 0.8$, where R_n is the normal device resistance when above the superconducting transition, are both linear and stable. Detectors which fall outside this range are cut from the data. Detectors with a $1/f$ cut-off knee or white noise level amplitude twice the array average are also cut. Typically, detectors with abnormally high noise levels are the result of an improper biasing of the readout multiplexing SOUIDs. After all cuts, approximately 600–700 detectors remain for a given TOD time segment. In principle, the only detectors which cannot be regained are the ~ 125 dead detectors. Time constant deconvolution and proper cut levels are being studied as ways to potentially include some of the cut detectors.

An internal calibration source is pulsed regularly during scanning (described in Section 5.2). These pulses are sent by the control computer. Data affected by these pulses are flagged and removed from the time streams to make maps. Similarly, cosmic rays and other electrical glitches are flagged and removed. The resulting data gaps are filled in with white noise estimated from the local background. Any 15 minute TOD file with more than 1000 glitches is completely removed. Approximately 2% of the data is cut for having cosmic-ray events, calibration bolometer activity, or otherwise displaying an abnormally large numbers of glitches.

5.2 Calibration

Calibrating the response of an array of bolometers is a three-step process. 1) the response of each bolometer to a given signal must be determined. Once determined, the response of each bolometer can be normalized to an average; the process is known as"flat-fielding" the array. 2) the relative calibration of each bolometer must be monitored in time. 3) an absolute calibration must be determined that translates data acquisition (DAQ) units into CMB temperature. A detailed description of the calibration methods are given in Switzer [2008], a brief summary is given below.

Each detector will have a different response to sky signal. When comparing one detector to another, variations in responsivity can result from: variations in detector properties resulting from fabrication, variations in forward gain and beam shape across the focal plane, alignment of the array to the optics, and variations in optimal bias points and readout from shared lines affecting response. The response of each detector to sky signal must therefore be measured. Two methods are currently used to flat-field the array. Before the start of each observing night, a load curve is

taken on each detector channel. The first order DC-responsivity can then be derived from this measurement [Irwin and Hilton, 2005]. The major drawback to this method is that knowledge of R_{shunt} is required (Figure 3.11). Their low values ($\sim 0.7\,\mathrm{m}\Omega$) make accurate measure difficult, and the values are only known to $\sim 20\%$[2]. Another draw back is that this method measures the electrical response only, and contains no information about optical coupling. While this calibration method is limited, it does allow for immediate calibration for a given night's measurements and is useful for monitoring field performance. The second method involves measuring the relative response to the changing atmospheric signal. Typically, atmospheric drift produces an approximately 300 mK variable signal over the course of a couple of minutes. This method is ideal because the atmosphere presents a common signal across all detectors, completely filling their beams. To prevent scan-synchronous signal from biasing the calibration, telescope scanning was stopped on several nights for ~ 5 minutes. A template was fit to these "stare" data and the relative calibration between detectors was determined. The atmosphere calibration method is accurate to $\sim 1\%$ in the 2007 data and is limited by the variability of the atmospheric signal (which provides the signal modulation during stare data) and the accuracy of the template fitting.

The relative calibration of the detectors changes in time because of variations in atmospheric and thermal loading. To monitor these changes, two calibration sources ("calbol") were mounted on the edge of each Lyot stop (Section 3.2.3). These calbols consist of a NiCr thin film deposited on a thin sapphire chip, suspended within a metal ring via nylon fibers [Beeman and Haller]. During operation, only one calbol is used, the other serves as a backup. They have acceptable time constants and minimal power dissipation ($\approx 40\,\mathrm{mW}$ per pulse); they are not seen by thermometers on the 300 mK

[2]The values of R_{shunt} are measured prior to array assembly

stage. Current is supplied by a commercial digital function generator (a Tektronix AFG 3021B). The source was pulsed every 500 s for a duration of 800 ms at 3.6 V, providing a fixed signal that could be used to track changes in detector response. The Lyot stop was chosen as the location of the calbol so that its signal illuminated the entire array, but this location had the disadvantage of being located on the 1 K stage. A sample pulse and lens cell response are shown in Figure 5.1. Limits were set on the amplitude and frequency of the pulse by the thermal conductance between the ^{4}He fridge and the calbol location (on the 1 K lens cell). The pulse caused a $\sim$ 300 mK rise on the 1 K lens cell. The maximum frequency of the pulses (i.e. time between pulses) was set by the requirement that the temperature of the 1 K lens cell return to its initial value before another pulse could be given. Once the amplitude and frequency were determined, the pulse duration (width) was set to minimize loading on the ^{4}He fridges so as not to compromise their hold times (and therefore observing time). Unfortunately, the signal reaching the detector was attenuated by the bandpass filter (located at 300 mK), so the resulting signal to noise is $\sim$ 7 at the detectors. Despite the low signal to noise, the calbol was still useful for monitoring detector gain drift. A season-long template was compiled for all pulses, and a functional form fitted to the template pulse shape. The individual pulses for each detector are fitted and scaled relative to the template. Atmospheric drift during the duration of the pulse affects the pulse shape. A smooth baseline drift is removed by subtracting from the pulse a straight-line interpolation of the noise value connecting the value before and after the pulse. This approach works best on nights with low PWV and potentially could be improved with more sophisticated atmospheric drift removal. However, even with this simple approach, the relative gain was found to be stable to $\sim$ 2% in the 2007 observing season.

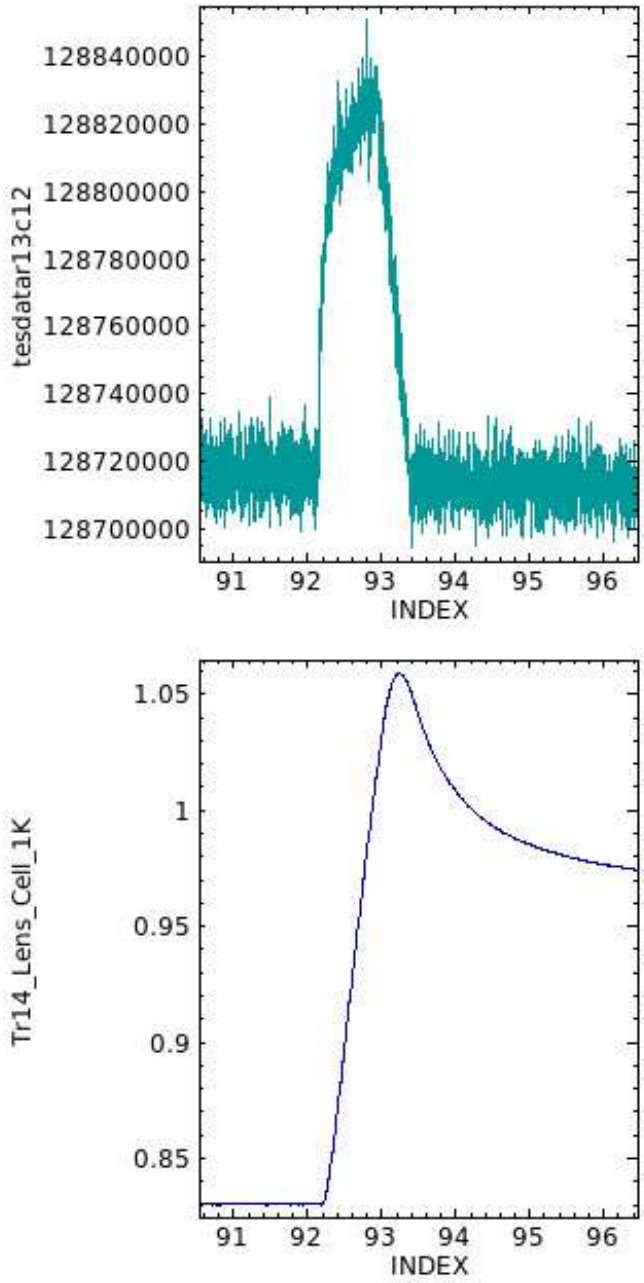

Figure 5.1 Detector signal and thermal response to a pulse from the calibration source. The top plot shows a typical detector response and the bottom plot shows the 1 K lens cell temperature where the calbol is located. The x-axes of both plots are in seconds. The y-axis for the detector is in digital acquisition units, and the lens cell is in Kelvin. The calbol heats the lens cell by $\approx 300\,\mathrm{mK}$. This heating and subsequent cooling via thermal conduction between the ^{4}He fridge limits the amplitude and frequency of the pulse. Bolometers have an average response with a signal to noise of 7.

A second relative calibration monitor is being developed where the detector bias point is rapidly stepped and returned to the original operating point. This method was originally developed to measure the electrical time constants. If the applied bias step size remains constant over time, the relative response of the detector measures the responsivity drift. In effect, this is a two point load curve. This approach has several benefits. The measurement only take a few seconds and does not increase the load (or reduce the hold time) on any of the cold stages. Also, while this is similar to a load curve, only the relative gain for a given detector is being measured, so knowledge of R_{shunt} is not required. During the 2007 observing season, bias steps were performed a few times per night. Analysis is underway to verify their agreement with the calbol.

The final calibration into CMB temperature will most likely come from cross correlation to the WMAP data. Calibrating with WMAP requires retaining sky map data on large (for us) angular scales to overlap with WMAP. Difficulties with atmospheric removal (discussed in Sections 5.3 and 5.4.1) have currently prevented us from using this method. A calibration has also been developed based on the measurement of planets, since disk averaged planet temperatures are relatively well known. Using planets as calibrators is difficult as it requires knowledge of several parameters, including: the expected emission from the source, the solid angle of the source, the solid angle of the detector beams, and the frequency response defined by the bandpass filter. Changing atmospheric opacity, which diminishes the source temperature, must also be accounted for. Since the planet source has a different spectrum than the CMB, the calibration must be scaled to CMB temperature units. Despite these difficulties, our current calibration is based on measurements of Saturn. Switzer [2008] provides a detailed description of the methods used in the global calibration and their associated

errors. It is estimated that the current calibration is good to $\sim 9\%$ at 1-σ, and is dominated by systematic errors in planet temperature estimation and detector solid-angle variation across the array. Using this calibration, the average CMB sensitivity per detector was $950\,\mu\mathrm{K}\sqrt{s}$ during the 2007 observing season.

5.3 Map-making

Once the detector time streams are cleaned and unwanted data removed, they are combined using the pointing reconstruction (discussed in Chapter 6) to produce a map of the sky. The maps assume that the detector TOD is a linear combination of the sky signal and noise. This model is written as

$$\boldsymbol{d} = M\boldsymbol{x} + \boldsymbol{n} \tag{5.1}$$

where $\boldsymbol{d}$ is the detector time-ordered data vector of length N_{TOD} time samples, $\boldsymbol{x}$ is the desired sky map containing N_{pix} pixels, $\boldsymbol{n}$ is the time-ordered noise vector of length N_{TOD}. The pointing matrix M encodes where the detector was pointed in time and has dimensions $(N_{TOD} \times N_{pix})$. The model can be thought of in terms of projection operators. Since $\boldsymbol{d}$ is the TOD, $M^T\boldsymbol{d}$ is the TOD projected onto the sky, and $M\boldsymbol{x}$ is the map projected back into the TOD. A Bayesian approach is used to solve for the estimated sky map $\hat{\boldsymbol{x}}$ given the data $\boldsymbol{d}$. The maximum likelihood solution for $\hat{\boldsymbol{x}}$ is then given by (see e.g., Lupton [1993])

$$\hat{\boldsymbol{x}} = (M^T N^{-1} M)^{-1} M^T N^{-1} \boldsymbol{d} \tag{5.2}$$

with noise covariance $N \equiv \langle \boldsymbol{n} \cdot \boldsymbol{n}^T \rangle$. Inverting these matrices is computationally difficult for large data sets. This system is more conveniently solved by rewriting Equation 5.2 in the form of $A\boldsymbol{x} = \boldsymbol{b}$ as

$$M^T N^{-1} M \hat{\boldsymbol{x}} = M^T N^{-1} \boldsymbol{d} \tag{5.3}$$

and solving the maximization problem using a preconditioned conjugate gradient (PCG) solver [Press et al., 1992].

In order to obtain a maximum likelihood solution to Equation 5.2, we must know the true noise covariance. An iterative method is used to determine an estimate of the noise. The first step is to choose a model that represents the noise: we usually take it to be the covariance of the TOD. We then obtain our first map estimation $\hat{\boldsymbol{x}}_0$. This first map estimation is sub-optimal because the data covariance is not the true noise covariance N. This map is projected back into the time domain as a model TOD: $M\hat{\boldsymbol{x}}_0$. The noise is then estimated by subtracting off the model TOD from the raw TOD as $\boldsymbol{n}_1 = (\boldsymbol{d} - M\hat{\boldsymbol{x}}_0)$, which should be a better estimate of the noise component of the TOD. The map is reestimated with the PCG solver, using noise covariance $N_1 = \langle \boldsymbol{n}_1 \cdot \boldsymbol{n}_1^T \rangle$. In this way, successive iterations should continue to remove sky signal from the noise estimate, thereby allowing the map estimator to properly deweight components of the data that are not consistent with sky signal, leading to an optimal map estimation.

Atmospheric sky signal dominates the TOD signal. The atmospheric signal varies by $\sim 300\,\mathrm{mK}$ (and can be as high as $1\,\mathrm{K}$) on the time scale of minutes and is correlated across the array. However, the atmospheric signal is not correlated between different observations of the same region of sky (either from night to night or cross link region to

cross link region). In this case, the rms atmospheric signal to noise will average down with multiple observations $\propto 1/\sqrt{N_{sample,i}}$ where $N_{sample,i}$ is the number of times on the sky pixel i is sampled. $N_{sample,i}$ is approximated by $N_{nights}N_{obs/night}N_{sample,i/obs}$ where N_{nights} are the number of observing nights, $N_{obs/night}$ are the number observations of the patch of sky per night and $N_{sample,i/obs}$ are the number of times pixel i is sampled by the array as the telescope scans and the sky rotates[3]. We can estimate $N_{sample,i/obs} \sim \frac{A}{RT}$ where A is the instantaneously imaged size of the array on the sky, R is the sky rotation, and T is the time it takes the telescope to return to a patch of sky $\approx$ scan size/scan speed. For 2007, the scan size was 5° at 1°/sec and the array images $\approx 0.3^\circ$, so $N_{sample,i/obs} \approx 14$. With 30 observing nights, and 2 cross linked observations per night, $N_{sample,i} \approx 840$. We therefore expect the rms atmospheric signal to be $\sim 10\,\mathrm{mK}$, clearly dominant over the CMB anisotropy of $\sim 100\,\mu\mathrm{K}$.

The diffuse atmosphere appears as a common mode signal across all detectors and can be removed prior to the map-making, by either applying a high-pass filter to the data or fitting a common mode signal across all detectors and subtracting it off. Either method will remove some amount of sky signal which cannot be recovered and potentially add correlated noise to the data. The extent that pre-processing affects the signal can be determined through simulations. However, it is better to treat the correlated noise within the map estimation. This can be done either through proper deweighting of the common mode noise covariance, or as a separate noise or atmospheric model simultaneously solved for in addition to the sky model. For ACT, this is especially important because subtracting the common mode and/or filtering will remove the correlated large-scale CMB anisotropy on scales of the array size

[3]A detailed calculation of $N_{sample,i}$ involves the telescope scan, cross-linking angle, and sky rotation. However, this approximation is useful to get an order of magnitude estimate of the residual atmospheric signal in the map.

and larger. This implies we will not be able to probe below $l \sim 600$, preventing calibration with WMAP if we simply remove the common mode. Modeling of the atmosphere and optimal atmospheric common-mode removal from the sky maps is the subject of ongoing work by the ACT map-making team. We are proceeding with high-pass filtered maps while the atmospheric models are being developed and tested on simulations. These filtered maps can be used to search for galaxy clusters and point sources that can be calibrated from planet measurements. However, the effects of the filtering still needs to be quantified using simulations before fluxes can be derived.

5.4 The Beam

The ACT maps are smoothed based on the profile of the beam, where the measured signal is convolved with the response of the beam. If the absolute calibration is based on a measurement of the flux from sources such as planets, a precise measure of the beam solid angle is required. Additionally, in Fourier space, the beam shape is the window transfer function, where the measured power spectrum is the true power spectrum multiplied by the window function.

Typically, bolometric detectors incorporate feed horns which define the shape of the beam. The ACT detector design utilizes a close-packed free-space detector design (Section 3.3) to maximize the number of detectors in the focal plane. The pixel size is $\sim 1\,\mathrm{mm}$ and is smaller than the wavelength of the incident radiation ($\sim 2\,\mathrm{mm}$). The ACT optics are diffraction-limited with nearly uniform illumination of the primary mirror and an approximately circularly symmetric pupil stop. With this geometry, we expect the beam shape to be approximated by a first order Bessel function, which

is known as the Airy pattern [Rohlfs and Wilson, 1996]. In reality, the beam will be averaged over the transmission through the bandpass filter and the actual illumination pattern depends on the optical coupling of each detector and its location in the focal plane. The beam shape is further complicated by the fact that the detector size is on the order of the size of the incident radiation and the detector pixel shape is a square. This makes an exact model of the beam complicated. A preliminary beam model has been developed in which a square pixel is convolved with a band-averaged Airy disk [Niemack, 2008]. In this simple case, we expect the ACT 145 GHz beam to have a full width at half maximum (FWHM) of 1.38 arcminutes, with the sidelobes of the Airy disk slightly damped due to the band averaging and square pixel convolution.

A map of a point source will exactly reproduce the beam on the sky. To map the beam shape we scanned several planets throughout the season. During planet scans, the telescope moves back and forth in azimuth at constant elevation while the planet either rises or sets through the array. Planets maps have high signal to noise[4] and planets are typically small compared to the size of the beam. During 2007, we observed Saturn, Mars, Uranus, Neptune, and Venus. Beam analysis has concentrated on the Saturn observations, because Saturn was scanned most nights at the survey observation elevation of 50.5°. Determining beam profiles using sources near the elevations used for observing science objectives minimizes potential elevation-dependent optical effects and allows for better characterization of the beam in the

[4]One concern with using high signal sources such as planets is whether the detector gain remains linear and that the detectors are not driven to the normal part of their superconducting to normal transition. To check this, we plotted the peak response of the detectors to the planet signal versus the fraction of detector bias along the transition, R_{TES}/R_n. We expect the peak response of the detectors to be similar in value for all bias values if the detectors remain in the linear regime. Similar peak responses for all bias values are observed for all planets except Jupiter. For Jupiter, we find that the response decreases sharply for detectors biased above 60% of their superconducting to normal transition, indicating that the large signal from Jupiter is causing these detectors biased above 60% on their transition to go nonlinear.

survey maps. Saturn's size varied from 17.6–18.5 arcseconds during the 2007 observing season and was on average approximately 20% of the beam size. To determine how the finite angular size of Saturn affects the beam measurements, we created a simulated beam represented as a sinc^2 function and convolved it with a circular disk (a 2-D top hat) with diameter of 18 arcseconds to represent the planet. The convolved beam was then compared to the simulated beam. We found that the integrated beam area increased by $\approx 5\%$. Therefore, a proper deconvolution of the planet disk with the beam should be included in the final derived window function.

5.4.1 Beam Pipeline and Mapping

We developed a modified cleaning and cuts pipeline for the beam analysis. This was required because planets have a high signal in the TOD, causing the standard cleaning and cuts pipeline to remove most detectors. The main modification was that for each planet observation, we fit a local pointing solution after deconvolving the Butterworth filter. This local pointing solution was used to remove the approximate section of the TOD which contained the main planet signal. The standard cuts (see Section 5.1) were then performed on the planet-removed TOD and the results stored. After the cuts were performed, we calculated the common mode signal across the array and stored that as well. The planet signal was then restored by reloading the TOD, and the stored cuts from the modified TOD were applied and common mode removed. The pointing was then recalculated on the common mode-removed TOD so the pointing result would not be biased by the atmospheric signal. We then did a cut on detectors which had pointing offsets that fell outside the maximum offset range possible based on the physical geometry of the array, which was typically only

a few detectors. The final cuts and pointing results were then stored.

The goal of the map-making was to remove as much of the atmospheric background as possible while preserving the planet signal. The beams overlap on the sky, so care must be taken to preserve the side-lobe features. We tested several techniques, including high-pass filtering the data prior to mapping and polynomial fitting to the common mode signal and subtracting it out. These methods removed significant planet signal and induced unwanted artifacts in the maps. Our final approach was to remove a filtered common mode signal prior to map-making, and then iterate on the map estimations in a way similar to the noise reestimation described in Section 5.3.

The first step was to apply the relative calibration and flat-field the array. Then, a common mode signal, $\boldsymbol{CM}(\boldsymbol{d})$, was calculated as the mean signal for all uncut detectors at each data point in time, so $\boldsymbol{CM}$ has length N_{TOD}. A 5 Hz low-pass filter was applied to the common mode signal before subtracting it from the individual detector TOD before mapping. The filter was necessary to preserve some signal in the lowest-order modes. A zero-power mode cannot be constrained in the map estimation. We found that maps without this filtering step would not converge. We then solved for the sky map with the PCG solver using $\boldsymbol{d}_0 = (\boldsymbol{d} - F_{lp}[\boldsymbol{CM}(\boldsymbol{d})])$, where $\boldsymbol{d}_0$ is the time-ordered data vector used in the map estimation (replacing $\boldsymbol{d}$ in Equation 5.2), $F_{lp}[\boldsymbol{CM}]$ is the low pass filtered common mode, where the common mode was estimated on the data $\boldsymbol{d}$. The common mode subtraction removes some of the planet signal because some amount of planet signal is common across detectors as the beams overlap on the sky. To regain the planet signal, we project the map estimation $\boldsymbol{x}_0$ back into a model TOD and subtract the raw TOD from the data TOD; $\boldsymbol{n}_{cm1} = (\boldsymbol{d} - M\boldsymbol{x}_0)$, where $\boldsymbol{n}_{cm1}$ is the first estimate of the common mode noise but still contains some sky signal. We then reestimate the common mode signal

using $\boldsymbol{n}_{cm1}$ and apply the low pass filter to the new common mode estimate and again subtract from the data: $\boldsymbol{d}_1 = (\boldsymbol{d} - F_{lp}[\boldsymbol{CM}(\boldsymbol{n}_{cm1})])$. A new map estimation $\boldsymbol{x}_1$ is found using the new estimate of planet-only signal, $\boldsymbol{d}_1$, and the process is then repeated. Successive iterations continue to separate out the planet signal from the atmospheric common mode signal.

To test the loss in planet signal from this mapping algorithm, we generated a simulated beam as described above, along with an atmospheric sky noise model, and projected them both into a model TOD. This simulated TOD was then run through the mapping algorithm. Figure 5.2 shows the results for one simulation. In general, we found that we recovered the peak signal and lost between 3–6% of the solid angle, depending on the size of the input beam simulation. Furthermore, the map estimations converged with successive iterations, suggesting the mapping algorithm is stable. This mapping routine was used to produce all the planet maps described below, with a map pixelization of 0.125 arcminutes. Here, we do not attempt to correct for the missing solid angle. A more sophisticated beam model and simulation is required to fully assess the mapping artifacts on the beam solid angle. This will be the subject of future work. However, the above mapping routine appears to work well and we expect similarly small amplitude effects on the resultant real-data beam maps.

5.4.2 Beam Asymmetry

The ACT survey maps are made by coadding data from detectors which are physically separated in the focal plane and data acquired throughout the observing season. In principle, each detector will have a different beam on the sky. In practice, we

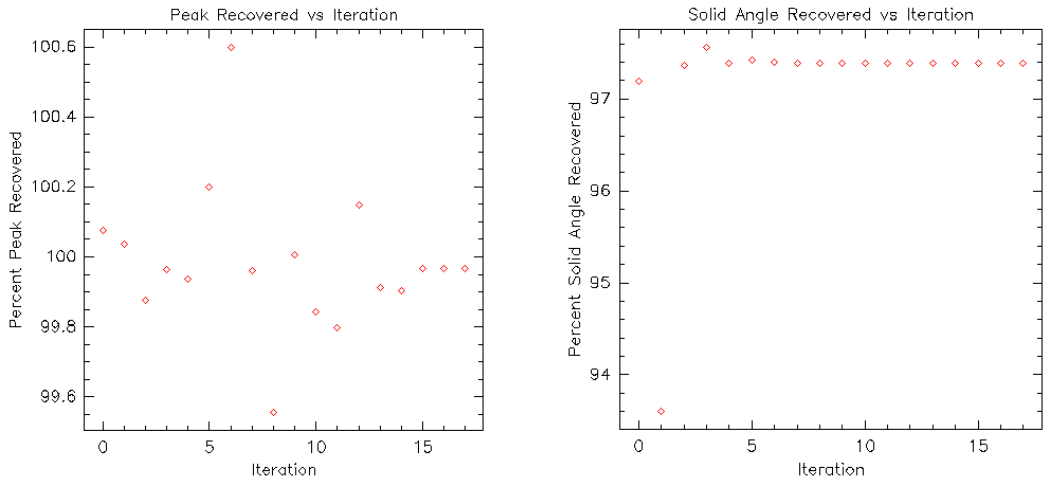

Figure 5.2 Plots showing the percentage of the recovered peak (left) and solid angle (right) for a simulation containing a beam and atmospheric model for 17 successive map estimations through the beam map-making pipeline. The new common mode is calculated for each map estimation, helping to recover the lost beam signal.

expect all detectors to have similar beams because of the high Strehl ratio across the focal plane and the near uniform illumination of the primary mirror, with any variation to be similar for detectors clustered near one another, as they will have the most similar optical paths. Ideally, an individual beam map would be made for each detector from the planet scans. However, this is not possible due to the large array size, planet motion, and the telescope scanning capabilities; a single detector beam is not fully sampled during a planet scan. In fact, even coadding all data for a single detector for all Saturn observations does not produce a fully sampled beam. To test for beam variation across the array, we instead made maps using nine subsections of the array. The array is composed of 32 stacked columns with each column containing 32 detectors, forming a 32×32 array of detectors (Sections 3.3). We naturally label each detector by its row and column location, noting that the columns are arranged horizontally on the focal plane. For each submap, we grouped the detectors in a 3×3

grid across the array; submap one contained detectors (row 00–10, col 00–10), submap two contained detectors (row 00–10, col 11–21) etcetera forming nine submaps each containing roughly 120 detectors, 70–80 of which typically survive the cuts and are suitable for including in the map. This was sufficient to produce a fully sampled beam for a single planet scan. Figure 5.3 shows the nine submaps for a single Saturn scan with the detector groups arranged on the focal plane as they see the sky.

We analyzed these nine submaps for six Saturn scans taken throughout the 2007 observing season (54 maps total). For each submap, we fit a 2-D Gaussian to a 2 arcminute $\times$ 2 arcminute square region around the peak in the map. The peak of our beam is well approximated by a Gaussian, and fitting to a small section around the peak insures proper fitting unbiased by either atmospheric contamination or beam sidelobes. The fitting function was allowed to rotate to produce the best fit. For each map we acquired a peak location, peak height, beam rotation angle, FWHM along the semimajor axis, FWHM along the semiminor axis, and an aspect ratio to measure beam symmetry defined as FWHM_x:FWHM_y, where x and y are along the major and minor axes of the beam shape. After the Gaussian fit is performed, the submaps are processed prior to calculating the solid angle. We masked a 15 arcminute region around the planet and fit a low-order polynomial in the map-pixel-coordinate plane to the remaining background. The polynomial was removed from the map, which helped reduce any residual atmospheric contamination. The processed map was then normalized using the peak value from the Gaussian fit for that submap before being integrated so the resultant solid angle is measured in steradians.

Table 5.1 shows the results and Figures 5.3 and 5.4 each show the nine submaps for two different Saturn scans. In all cases, the errors in Table 5.1 are the 1-σ standard deviation for the set of measurements. There is a clear asymmetry in the beam in

different subsections of the array, with a maximum aspect ratio of 1.15 and minimum ratio of 1.03. This asymmetry is repeatable from observation to observation (compare submaps in Figures 5.3 and 5.4), as evidenced by the low standard deviation of the 6 measurements. The beam orientations vary slightly in angle across the array, but are approximately aligned with each other. We also find varying peak response and beam size but with a different pattern across the array than the asymmetry. The center of the focal plane, hence the center of the array, is expected to have slightly larger ($\sim$ 4%, [Dicker, 2005]) illumination, with correspondingly smaller beam sizes, and slightly higher ($\sim$ 2%, [Fowler et al., 2007]) Strehl ratio's. This matches the pattern we see, with measured peak response approximately 4–7% larger in the central submap compared to the four corner submaps. Beam asymmetry in the corners of the array was also expected, but the central pixels (and those forming a cross through the center of the array) were expected to be symmetric (see Figure 5.5), in contrast to the pattern we observe.

There is a known detector offset pointing error on the ~ 5 arcsecond level (Section 6.2). This offset is expected to be constant across the array during a planet scan. To verify that this systematic pointing offset does not induce an apparent ellipticity in the beam, we produced single detector maps by coadding 17 Saturn observations. Single detector maps are not biased by any relative detector to detector pointing offset, and have no knowledge of relative detector spacing. A coadded map was created for detector [r05 c29], in the highly asymmetric region with aspect ratio 1.15 (lower left map in Figure 5.3), and detector [r05, c03] in the symmetric region with aspect ratio 1.03 (top left region in Figure 5.3), where rxx is row location and cxx is column location. The result is shown in Figure 5.6. While these single detector maps do not fully sample the beam, it is clear that the asymmetry pattern is preserved in

the single detector maps and similar to the asymmetry in the submap section they were chosen from. Because the beam asymmetry can be characterized by groups of detectors near each other in the focal plane, and not along rows or columns, it is most likely caused by a misalignment along the optical path and not misalignment during the folding or stacking of individual detector columns in array assembly. The phase space for potential positional and angle misalignments of the three lenses is large. It should be noted that the design tolerances were specified to maximize Strehl ratio only; it is therefore not surprising we see beam asymmetries. These asymmetries are likely not important for ACT results (Section 5.4.3). However, beam asymmetries will be important for potential future upgrades to measure CMB polarization [Hu et al., 2003]. Preliminary work has shown that optical misalignments can reproduce beam asymmetries similar to the observed patterns (see Figure 5.7).

5.4.3 Beam Asymmetry Effects on the Window Function

CMB experiments have often used a symmetrized beam, where an azimuthally symmetric beam pattern is assumed [Netterfield et al., 1997, Page et al., 2003, Jarosik et al., 2007]. To estimate the error from azimuthally averaging over an asymmetric beam, we computed beam window transfer functions for a simulated Airy beam pattern in the flat sky approximation. For ACT, the beam for rising and setting maps are rotated by the cross link angle. Cross linking helps to symmetrize the beam. We first computed the transfer function for a symmetric Airy pattern with FWHM of 1.4 arcminutes. We then rotated and sheared the Airy pattern by the numbers given in Table 5.1. A new beam transfer function is computed taking an azimuthal average over the now asymmetric beam. The ratio of the unsheared to sheared transfer func-

Table 5.1 Beam Parameters for subsections of the array, The table is arranged as the subsections are oriented on the sky, the same as in Figure 5.3. SA = solid angle and AR = aspect ratio ≡ FWHM_x:FWHM_y.

	Row 00–10	Row 11–21	Row 22–32
Col 00–10	Peak: 6.37 ±0.17 K FWHM_y: 1.32′ ±0.02′ FWHM_x: 1.35′ ±0.02′ SA: 219 ±7 nsr AR: 1.02 ±0.004 Angle: 35° ±6°	Peak: 6.49 ±0.16 K FWHM_y: 1.27′ ±0.01′ FWHM_x: 1.38′ ±0.01′ SA: 211 ±7 nsr AR: 1.09 ±0.004 Angle: 34° ±4°	Peak: 6.26 ±0.17 K FWHM_y: 1.25′ ±0.01′ FWHM_x: 1.42′ ±0.01′ SA: 216 ±12 nsr AR: 1.14 ±0.01 Angle: 41° ±4°
Col 11–21	Peak: 6.41 ±0.18 K FWHM_y: 1.26′ ±0.01′ FWHM_x: 1.39′ ±0.01′ SA: 222 ±11 nsr AR: 1.10 ±0.01 Angle: 47° ±5°	Peak: 6.62 ±0.19 K FWHM_y: 1.25′ ±0.004′ FWHM_x: 1.37′ ±0.01′ SA: 213 ±5 nsr AR: 1.10 ±0.01 Angle: 47° ±5°	Peak: 6.51 ±0.15 K FWHM_y: 1.25′ ±0.01′ FWHM_x: 1.39′ ±0.02′ SA: 211 ±10 nsr AR: 1.12 ±0.02 Angle: 51° ±4°
Col 22–31	Peak: 6.17 ±0.19 K FWHM_y: 1.25′ ±0.01′ FWHM_x: 1.44′ ±0.02′ SA: 218 ±6 nsr AR: 1.15 ±0.01 Angle: 49° ±2°	Peak: 6.31 ±0.17 K FWHM_y: 1.25′ ±0.01′ FWHM_x: 1.42′ ±0.01′ SA: 218 ±7 nsr AR: 1.13 ±0.02 Angle: 43° ±3°	Peak: 6.18 ±0.21 K FWHM_y: 1.29′ ±0.01′ FWHM_x: 1.39′ ±0.01′ SA: 220 ±7 nsr AR: 1.08 ±0.01 Angle: 53° ±4°

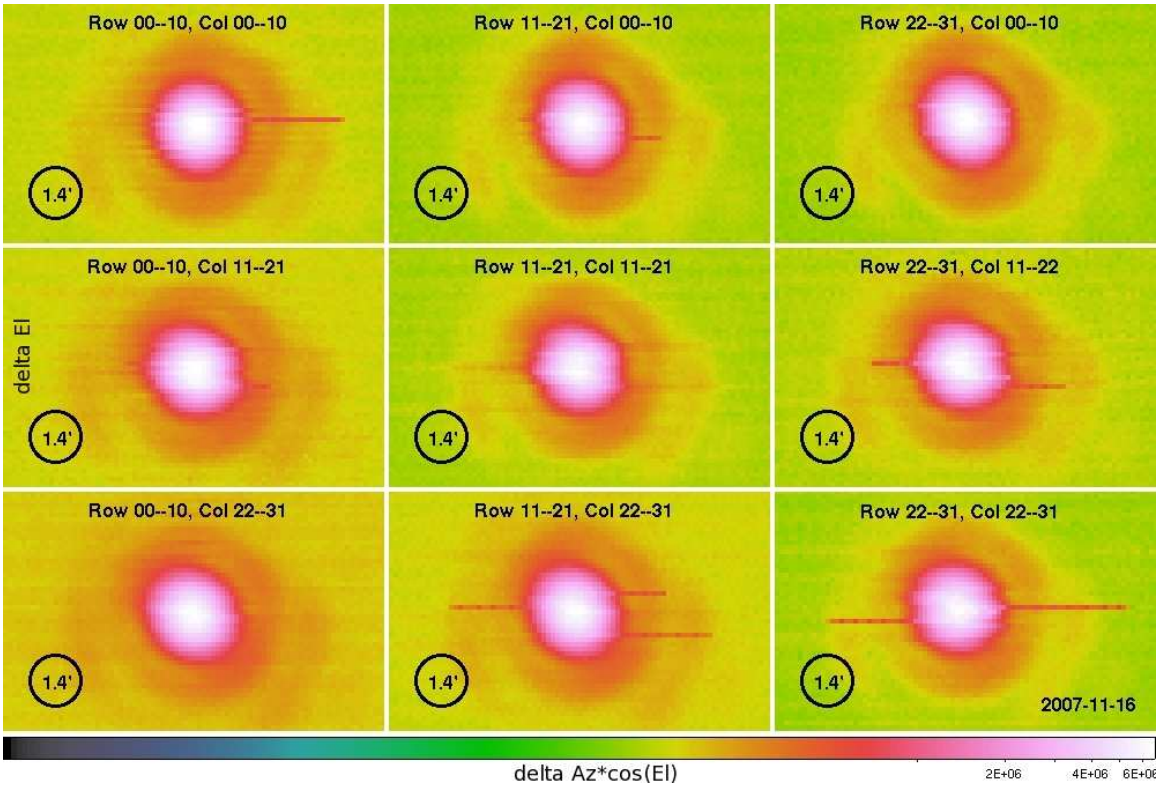

Figure 5.3 Beam maps made from nine subsections of the array for a Saturn observation on 2007-11-16. The array is broken into a 3 × 3 grid; each submap contains ∼ 100 detectors, enough to fully sample the map. The submaps are arranged to represent how that focal plane subsection images the sky. The maps show a varying beam asymmetry across the focal plane. A 1.4 arcminute circle is inserted in the lower left of the map to show the approximate FWHM.

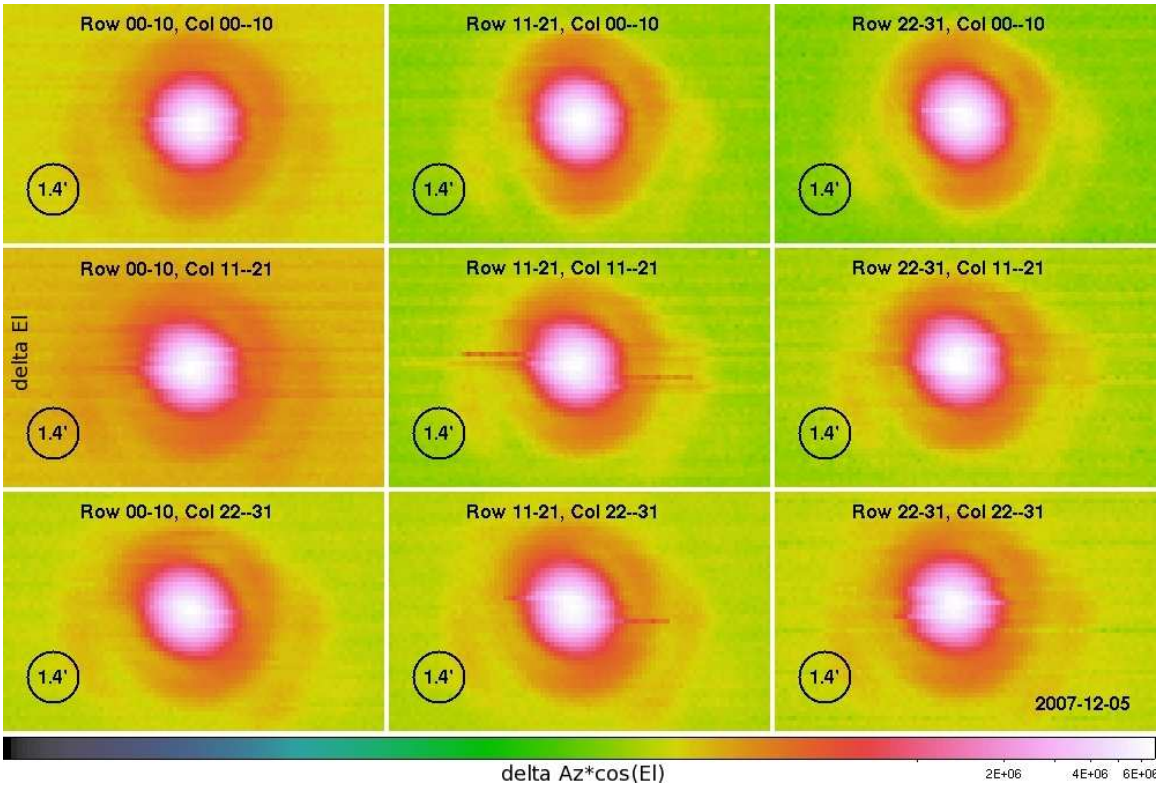

Figure 5.4 Beam maps made from nine subsections of the array for a Saturn observation on 2007-12-05. The array is broken into a 3×3 grid; each submap containing $\sim$ 100 detectors, enough to fully sample the map. The submaps are arranged to represent how that focal plane subsection images the sky. The maps show a varying beam asymmetry across the focal plane. A 1.4 arcminute circle is inserted in the lower left of the map to show the approximate FWHM.

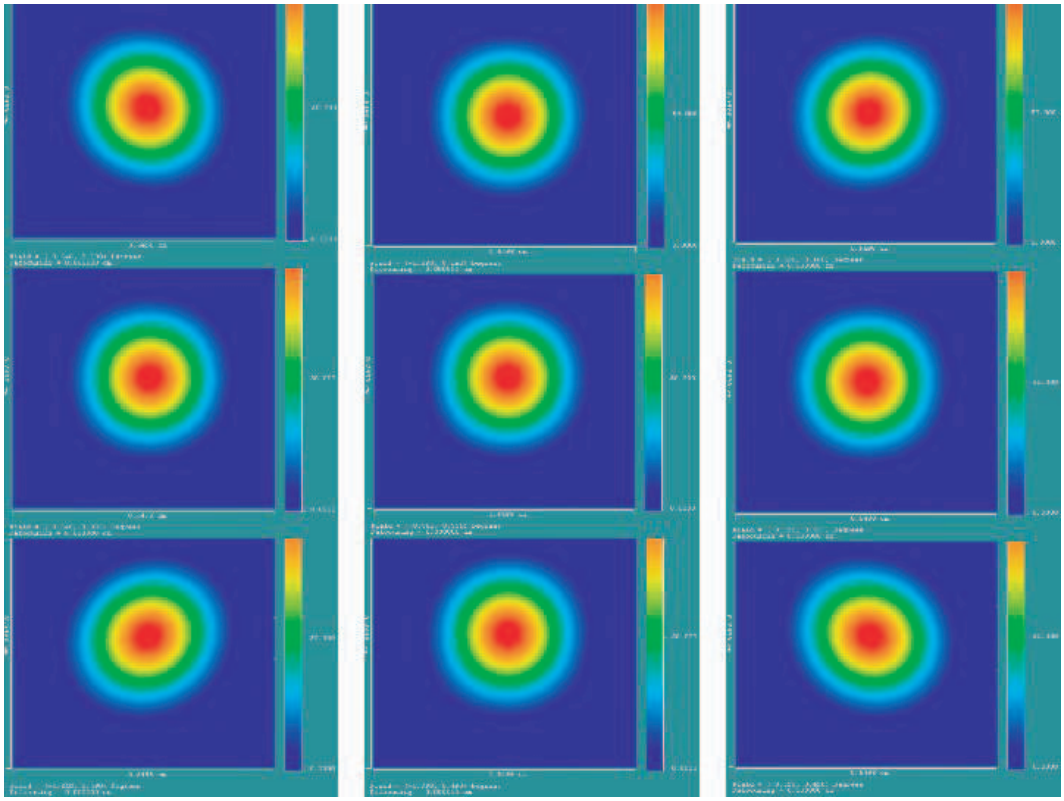

Figure 5.5 Simulated beams for detectors in each of the 9 subsections using the optical model, with all optical elements correctly placed. The submaps are arranged in the same way as in Figure 5.3. The color scale is linear and goes from 0–100. Even with perfect alignment, some beam asymmetry is expected. The expected beam asymmetry is aligned radially towards the center of the array. Figure courtesy of M. Niemack.

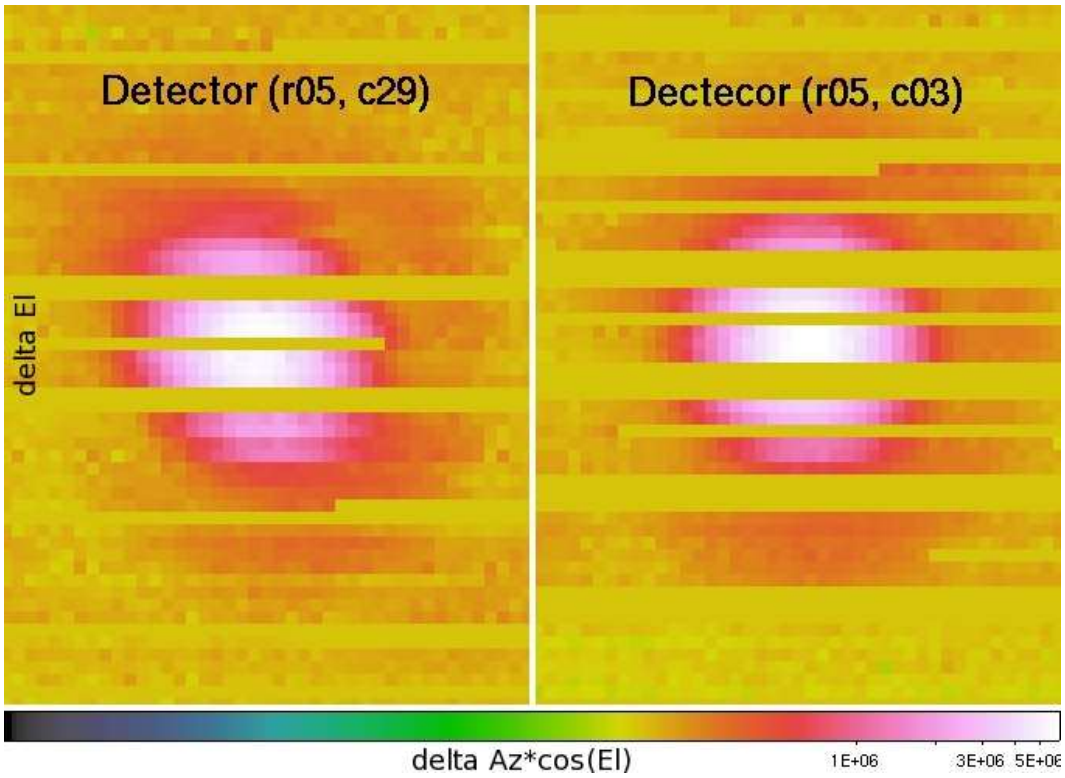

Figure 5.6 Single detector maps from coadding 17 Saturn observations. The map on the left was made using a single detector from the most asymmetric focal plane region (lower left of Figure 5.3) and the map on the right for a detector from the most symmetric focal plane region (top left of Figure 5.3). Individual detector maps are not fully sampled, but clearly reproduce an asymmetric pattern similar to the subsection maps made out of the ~ 100 locally grouped detectors. These maps demonstrate that the observed beam asymmetries are not caused by relative detector pointing errors.

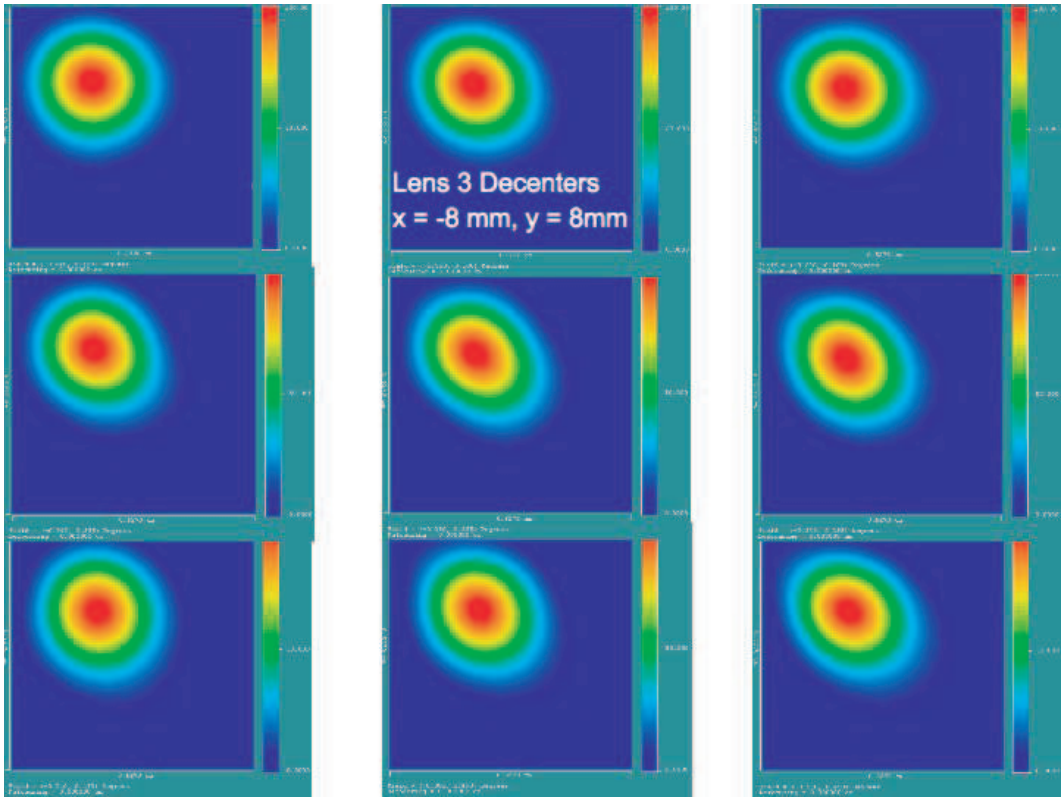

Figure 5.7 Simulated beams for detectors in each of the 9 subsections with misalignment in the optical model. The submaps are arranged in the same way as in Figure 5.3. The color scale is linear and goes from 0–100. In this model, the final lens (300 mK lens) has been decentered from the rest of the optical elements by 8 mm in x and y directions from the optical z-axis. This offset approximately reproduces the measured asymmetric pattern, but the decentering used here is larger than is physically possible in MBAC. However, this exercise demonstrates that optical misalignments can generate beam asymmetries similar to what is observed. Figure courtesy of M. Niemack.

tions is an estimate of the error from an incorrect beam deconvolution from using a symmetrized beam.

We computed a worst case asymmetry with aspect ratio 1.15 and our best estimate of the ACT beam. For our best estimate, we created nine shear maps following the results given in Table 5.1, and then coadded the maps before calculating the transfer function. This is similar to calculating a single beam from a planet map which used all detectors in the array to produce the map. Figure 5.8 shows a plot of the ratio of transfer functions, with and with out cross linking (we did both because not all regions of sky will be cross linked). The results indicate that the error induced by assuming a symmetrized beam will be negligible at low l and remain less than 1% out to l of 10,000 for a beam aspect ratio up to 1.15. For our estimated cross linked ACT beam (our current best estimate for the beam in the survey map region), the effect is below approximately 0.1%. Our errors at high l will most likely be be dominated by the beam resolution, calibration error, point source subtraction errors, and other foreground contamination, at levels much higher than this. It is therefore acceptable to use a symmetrized beam for the ACT analysis.

5.4.4 Beam Stability

Any variability in the beam shape will propagate as an error in the window function and calibration. Large variation would indicate that the telescope optics are not stable. In this case, coadding data from separate observations would be difficult. To measure the stability of the beam, we made maps of Saturn taken on 17 different observing nights in the 2007 season. To provide the highest signal to noise, these maps were made using all the detectors in the array which survived the cuts. We

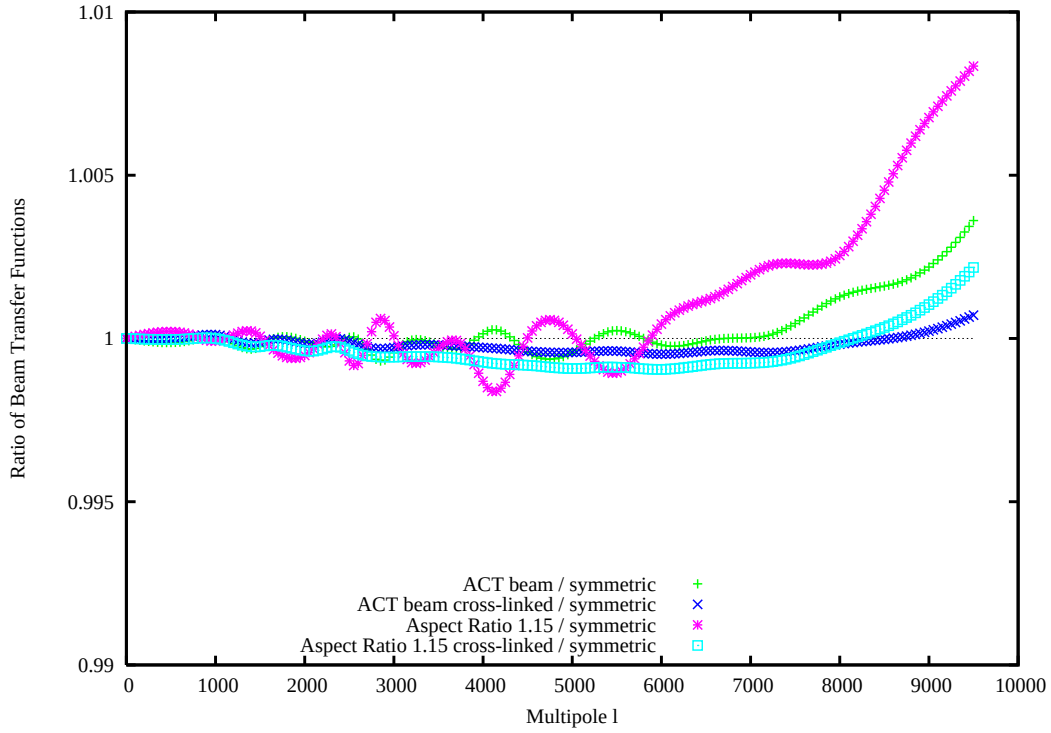

Figure 5.8 Beam asymmetry effects on the window function. Plotted is the ratio of window transfer functions computed for symmetrized asymmetric beams over a true symmetric beam. Symmetrizing the ACT asymmetric beam will have minimal effect on the window function.

estimate the variability by measuring the FWHM in the azimuth and elevation direction. We chose to fit for the FWHM in the telescope scanning coordinates of azimuth and elevation, because these provide sensitivity to potential beam variation induced by telescope motion. For instance, if the FHWM in the azimuthal direction showed large variation, while the FWHM in the elevation direction was stable, this would indicate that the variation was being induced by the scanning motion. We chose to use FWHM as the stability measure because it provided a relatively stable high signal measure. The solid angle suffers from variations in background subtraction uncertainty in the mapmaking step. The peak response is also a high signal measure, but can be affected by changes in Saturn's emission temperature and atmospheric absorption. Saturn's temperature is expected to vary by $\sim 10\,\%$ due to its motion relative to Earth. This positional change can be accounted for, but Saturn's emission temperature will vary due to changing ring inclination and emission from its satellites [Switzer, 2008].

Figure 5.9 shows the measured FWHM for the 17 observations over the course of the 2007 observing season. We find that the $\mathrm{FWHM}_{az} = 1.379 \pm 0.005$ arcminutes and $\mathrm{FWHM}_{el} = 1.360 \pm 0.006$ arcminutes. For a Gaussian beam, this measured error in FWHM implies a $\lesssim$ 1% 1-σ uncertainty in the measured solid angle. Therefore, we expect the beam error to be dominated by uncertainty in the atmospheric subtraction mapping algorithm, not from beam variability from observation to observation.

Given the stability of the beam and the negligible effects of symmetrization, the 17 individual maps were coadded together to produce our highest signal map. Prior to coadding each map was peak normalized and recentered to the location of the Gaussian peak to reduce blurring from pointing error (Section 6.3). The final coadded map of 17 Saturn observations is shown in Figure 5.10. The residual stripes in the

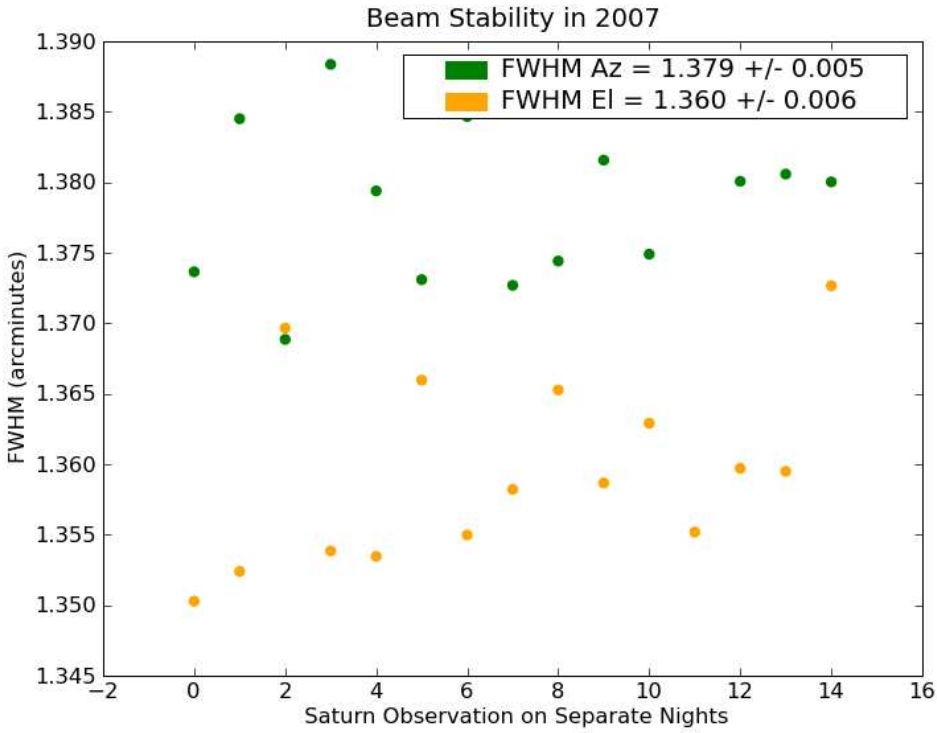

Figure 5.9 Beam stability over the 2007 observing season. The plot shows the measured FWHM in the azimuth and elevation direction for 17 Saturn observations over the course of the 2007 observing season.

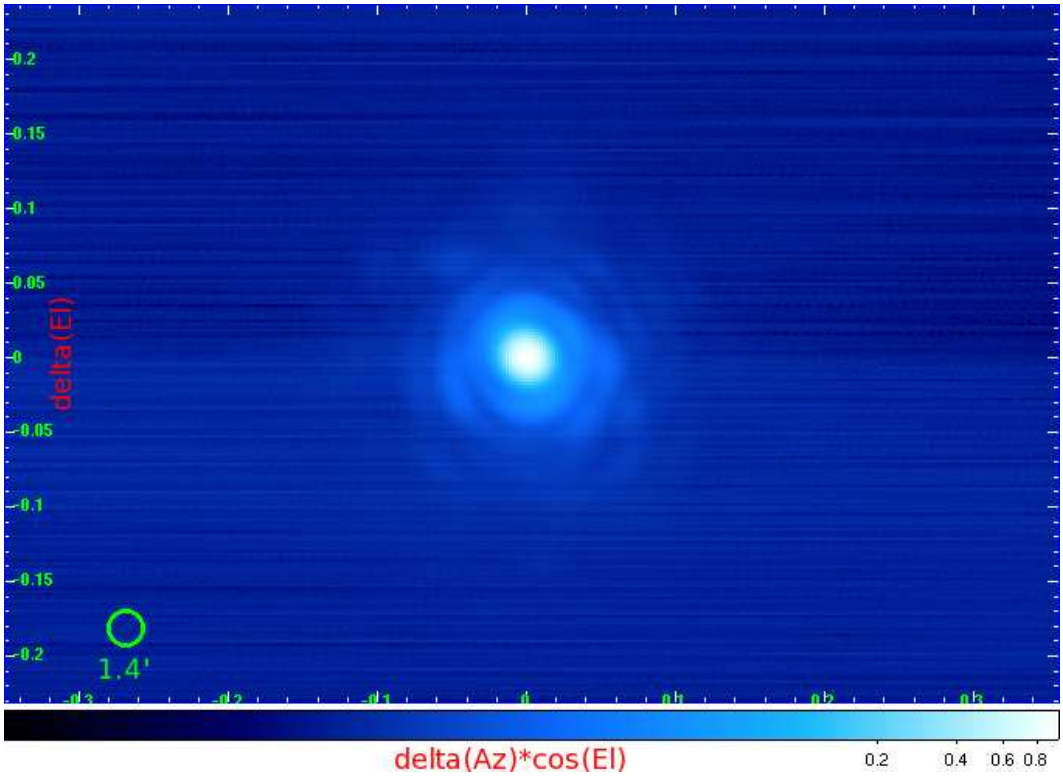

Figure 5.10 Beam map from coadding 17 Saturn observations using all uncut detectors. The color scale is in log. The first sidelobe is at a radius of approximately 2 arcminutes and is down $\sim$ -15 to -17 dB from the peak of the main lobe. A second sidelobe appears at approximately 3.2 arcmin and is down $\sim$ -20 to -24 dB. The measured beam properties for the coadded map are: FWHM_{az} = 1.38 arcmin, FWHM_{el} = 1.36; solid angle = 224 nsr.

map are likely caused by calibration errors. With this high signal map, the expected sidelobe features are visible above the noise.

Chapter 6

Telescope Pointing

One of the goals during the commissioning period was to verify the telescope could point to the desired accuracy of 6 arcseconds rms. Furthermore, we wanted to understand pointing systematics and develop a pointing model to correct for these effects. Knowing where the telescope is pointed as accurately as possible is critical for several reasons. To make a season-long survey map, ACT scans the same patch of sky night to night throughout the observing season. Nightly maps are made and then coadded. An error in the pointing reduces the peak amplitudes of point sources and clusters, and broadens the apparent size of the objects on the sky. An error in pointing also changes the window function; knowing the window function is critical to parameter estimation using the power spectrum. Finally, the absolute pointing accuracy determines the precision to which we can match sources in our maps to sources from other surveys.

6.1 Telescope Scan Performance

To modulate the bolometer signal on the sky, the upper telescope structure (including MBAC and the detectors) is rotated back and forth in azimuth while maintaining constant elevation. The scan is done at a constant velocity between turnarounds and the amplitude is 5° peak-to-peak in azimuth. Rapid turnarounds at the end points of the scan minimize time spent not scanning, which maximizes the sky overlap of the three separate arrays as discussed in Section 3.1 (see Figure 3.2). The telescope is designed to produce a maximum scan speed of 2°/s with a turnaround time of less than 400 ms ($10°/s^2$) while maintaining a pointing error of 6 arcseconds rms from the commanded position in both azimuth and elevation. The rapid turnarounds combined with the 40 metric ton scanning component of the telescope made the pointing stability during scanning a considerable challenge.

The telescope motion systems were designed by KUKA, a robotics systems company[1]. The telescope position is recorded using a pair of 27-bit Heidenhain absolute encoders on the azimuth and elevation axes. The KUKA controller uses an identical pair of encoders mounted next to these, and their readout and control loops are completely independent. Inclimometers are mounted on the telescope base and the rotating structure to measure tilt, and accelerometers are mounted at four positions along the center of the primary mirror and one near the secondary mirror. The readout of these devices is synchronized to within 5 µs of the detector data [Switzer et al., 2008]. The elevation encoder readings are well within the pointing requirements during the constant-velocity portion of the scan. During the turnarounds, the telescope experiences a jitter in the elevation axis. The size of this jitter is approximately ± 3.5

[1]Internet URL:http://www.kuka.com

arcseconds, within the 6 arcsecond rms pointing requirement. The azimuth axis also experiences an overshoot at the turnaround of scans. This overshoot exceeds the 6 arcsecond tolerance, but is damped out by the controller within 300 ms and thus is not a significant concern. Figure 6.1 shows the azimuth encoder readings and residuals during a scan with the maximum speed and turnaround acceleration.

During the 2007 observing season, the scan speed was reduced to $1^\circ/\mathrm{s}$ because of the optical time constants of the detectors. At these scan speeds, the residuals of the azimuth overshoot are less than 2 arcseconds. As a result of this performance, the detector data acquired during turnaround was included in the 2007 map-making.

6.2 Detector Offsets

Because map-making involves the coadding of signal from every detector each time it crosses a given section of sky, a complete pointing solution is required. Individual pointing solutions for each detector are required because each detector sees a slightly different patch of sky (Figure 3.2). These offsets are determined by scanning over several bright point sources—in our case, these sources were planets. The telescope is not capable of tracking a source, instead we scan back and forth in azimuth at constant elevation as the source either rises or sets through the detector array. To find the offsets, Gaussians are fit to the peaks in the TOD. A mapping is then made between the individual detector peak locations and the encoder's azimuth and elevation reading at that time. This gives a per-TOD, per-detector offset. Several planet scans were carried out and the resultant TOD offsets were then averaged together to give a detector offset look-up table. This look-up table is fed into the map-maker, so that the relative position on the sky is known for each detector at a given telescope

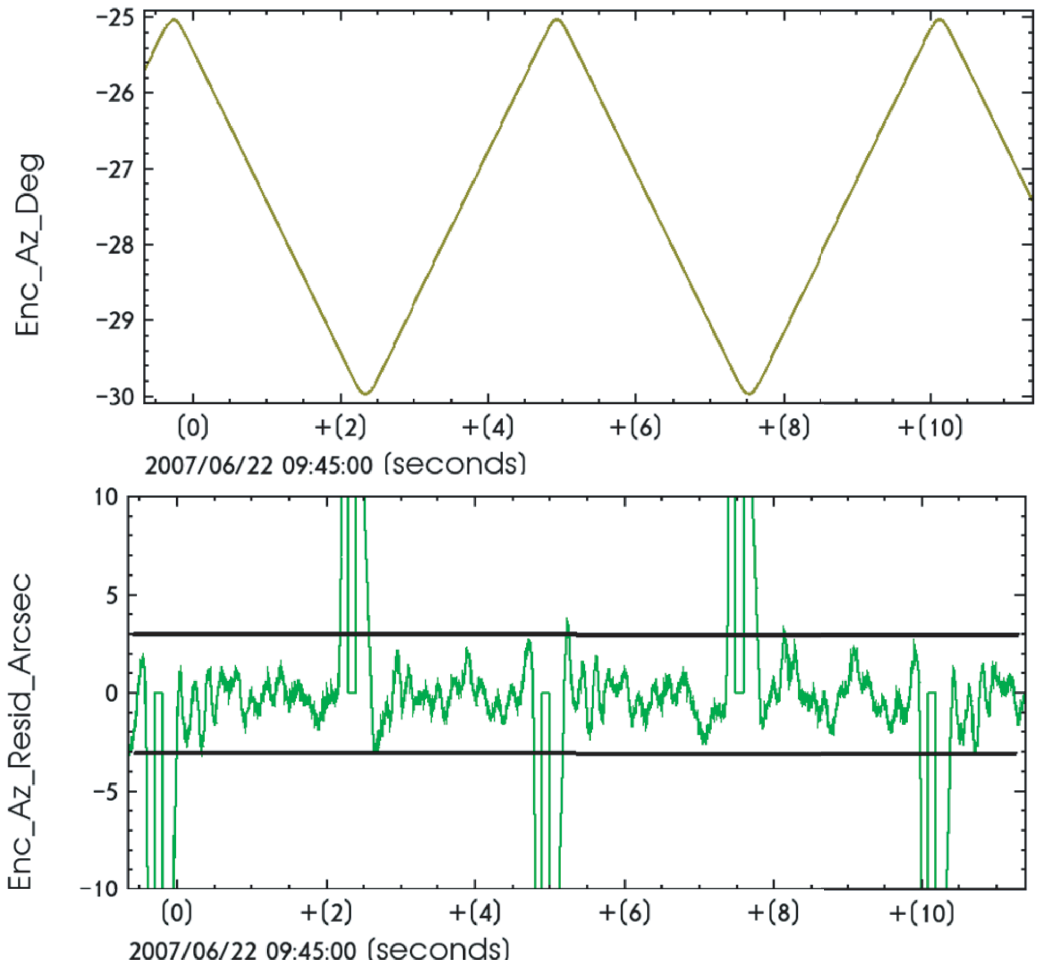

Figure 6.1 Telescope scan performance for 2°/s azimuthal scans, the maximum scan speed. *Top:* Azimuth encoder readings. *Bottom:* Residuals of the azimuth position. The residuals are from fitting a straight line to the azimuth data. Figure courtesy of M. Devlin and J. Klein

azimuth and elevation.

To test the accuracy of the detector offset look-up table, nine subarray maps were made for scans of Saturn (as described in Section 5.4). Each of these subarray maps should produce a map with the planet peak in the same location with random scatter about the center. The size of the scatter should reflect the accuracy of the offset look-up table. Figure 6.2 shows the resultant maps for each of the subarray sections. A coordinate grid that has the same absolute coordinates is overplotted in each map.

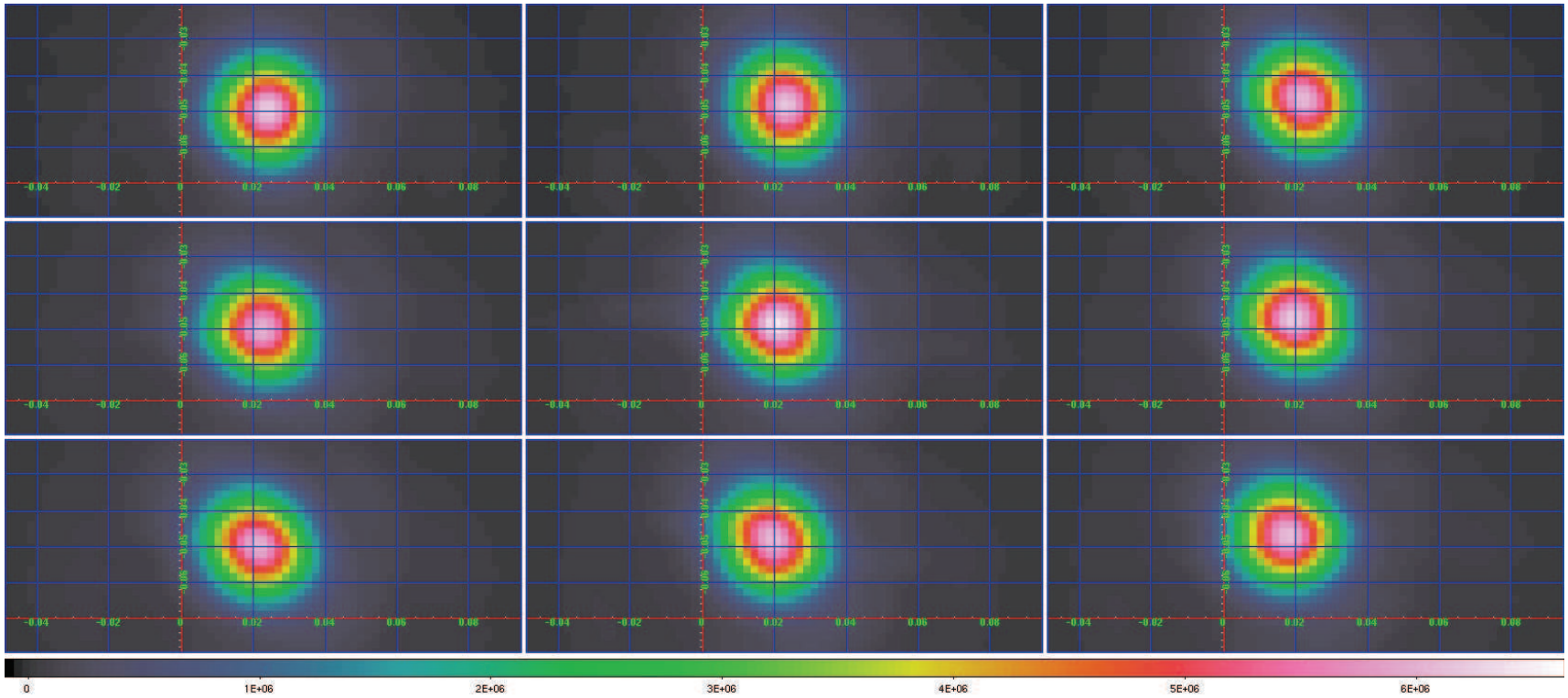

Figure 6.2 Nine maps of Saturn for different subsections of the array. The grid axes are in degrees. The grids across each map have identical coordinates. The position of Saturn changes in the different submaps.

The peak location of Saturn shifts approximately ± 10 arcseconds in both azimuth and elevation. To check whether this offset is random scatter, the subarray maps were made for six scans of Saturn. The centroid of the planet is found for each map by fitting a 2D Gaussian to a 2 arcminute region around the brightest pixel in the map. Fitting to a small section around the peak ensures that the beamshape is still well approximated by a Gaussian and the center location is not biased by the sidelobes or any residual atmosphere left in the maps.

Figure 6.3 shows the elevation offset and azimuth offset for the nine subarray sections for each of the six Saturn scans. The relative sectional offsets are repeatable from night to night indicating that the pointing error is not random. Instead, a systematic effect is introduced somewhere in the process of obtaining the individual detector offsets from the TOD, to applying those relative offsets during map-making. The exact cause of this systematic offset is still unclear. Figure 6.4 shows the azimuth and elevation systematic offsets for the different subsections. The systematic offsets are distributed in a pattern emanating from the center of the array, with an elevation offset that tracks the rows, and offsets in both azimuth and elevation that track the columns. Using this, we can correct for the relative detector pointing while a new pointing offset code is being developed.

6.3 Absolute Pointing Stability

The absolute pointing of the telescope is determined by scanning over several planets, and comparing the azimuth and elevation encoder readings to the known planet locations from an ephemeris. Multiple scans over planets at several telescope locations were used to develop a global pointing model that depends on physical

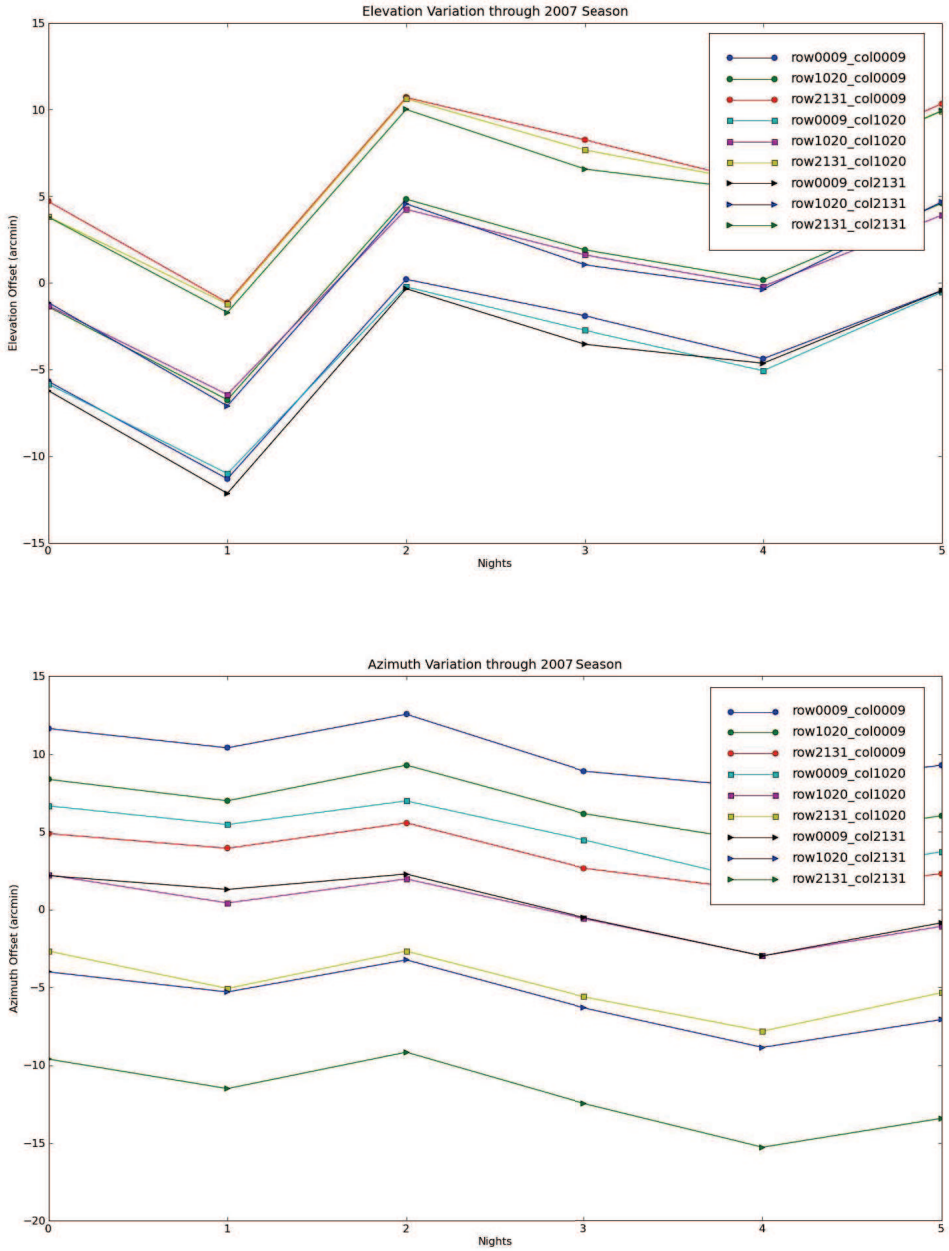

Figure 6.3 Systematic offsets in elevation (top) and azimuth (bottom) for the nine detector subsections for six Saturn scans. The scans were randomly chosen from six nights in the 2007 season (indicated by "Nights" on the x-axis). The measured offsets on the y-axis are plotted relative to the expected position of Saturn. The pointing offsets from night to night are repeatable (distance between the nine points), indicating that the error is not due to random pointing error but a systematic error in going from detector offset to map space.

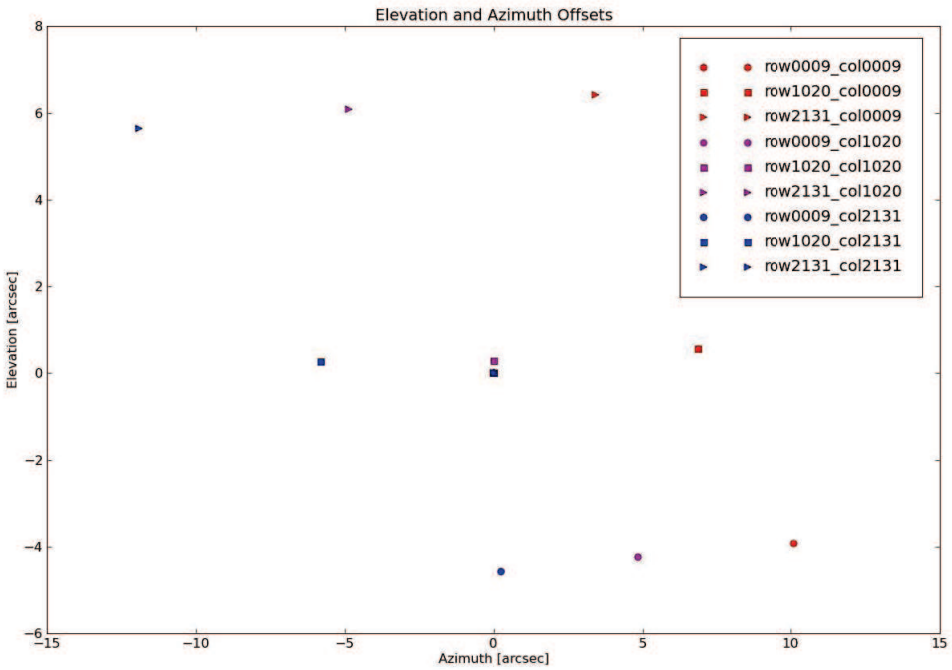

Figure 6.4 The systematic pointing error in the relative detector offsets. The azimuth and elevation positions were fit to the nine subarray maps for six Saturn scans. Subarray maps that share the same detector columns have the same color; subarray maps with the same detector rows have the same symbol. There is a pattern to the offset, emanating from the center of the array. There is primarily an elevation offset that follows the rows, and azimuth and elevation offsets in the columns.

parameters of the telescope. To interrupt normal observing as little as possible, most of these planet observations used in the model were taken during dedicated planet observing nights, with only one or two planets observed on most normal observing nights. The season-long survey maps are made by coadding maps made from the individual TODs from night to night. Temporal changes in the mechanical structure of the telescope between observations will alter the absolute pointing of the camera. These changes will not be represented in the encoder readings or the pointing model. This varying absolute pointing reduces the peak signal and broadens the beam in the final coadded maps. Therefore, to coadd the detector data, the telescope absolute pointing must be repeatable in the survey region from observation to observation over the course of the season.

To evaluate the absolute pointing accuracy, the measured peak location of Saturn was compared in several maps throughout the month-long 2007 observing season. Ideally, bright point sources in the survey region would be used, but the sources are not bright enough to give reliable centroids in a single observation. Saturn observations at the same elevation as the survey region of 50.5° were therefore chosen, making for a more direct comparison to the survey region. Furthermore, these Saturn observations spanned only 0.7° in telescope azimuth. Thus, observed pointing offsets are the result of variation in the night to night absolute pointing of the telescope, and not offsets induced from changes in azimuth and elevation, which are known to give additional pointing offsets (see Section 6.4). The maps are made using locally flat telescope coordinates of $\Delta Az * \cos(El)$ and ΔEl, where Az is the telescope azimuth and El is the telescope elevation, around the known source location. Variation in the peak locations measures the accuracy of the absolute pointing stability between observations. Figure 6.5 shows the absolute pointing offset in both azimuth and

elevation from thirteen Saturn observations taken throughout the 2007 observing season. In azimuth, the pointing is highly reproducible, with a pointing error of $\approx \pm 2$ arcseconds. The elevation pointing error is larger, $\approx \pm 8$ arcseconds. In both cases, the error is the 1-σ standard deviation of the measurements.

The large deviation in elevation pointing is likely caused by diurnal thermal heating and cooling of the telescope structure. During the day, when the Sun hits the telescope BUS, differential heating causes the primary and secondary mirrors to change their relative positions to each other by up to 4 arcminutes [Hincks et al., 2008]. Attempts were made to try to correlate the measured elevation offset to temperature sensors mounted on the BUS and the back of the primary mirror panels themselves. Unfortunately, there was little correlation between the measured telescope temperatures and the observed pointing offsets. The reason for the lack of correlation is probably because the final settling position of the telescope, which is setting the elevation pointing offset, is dependent on the exact heating and cooling dynamics on that day.

Despite the lack of correlation to BUS temperature, the absolute pointing recovered, as shown in Figure 6.5, is still remarkable. The repeatability of the Saturn measurements implies that over the course of the 2007 observing season, the telescope settled back to the same position every night to within 8 arcseconds despite the large daily heating of the structure and other non-quantified variables which affect the absolute pointing. We can further correct the elevation pointing offset by applying a measured planet offset to the survey region.

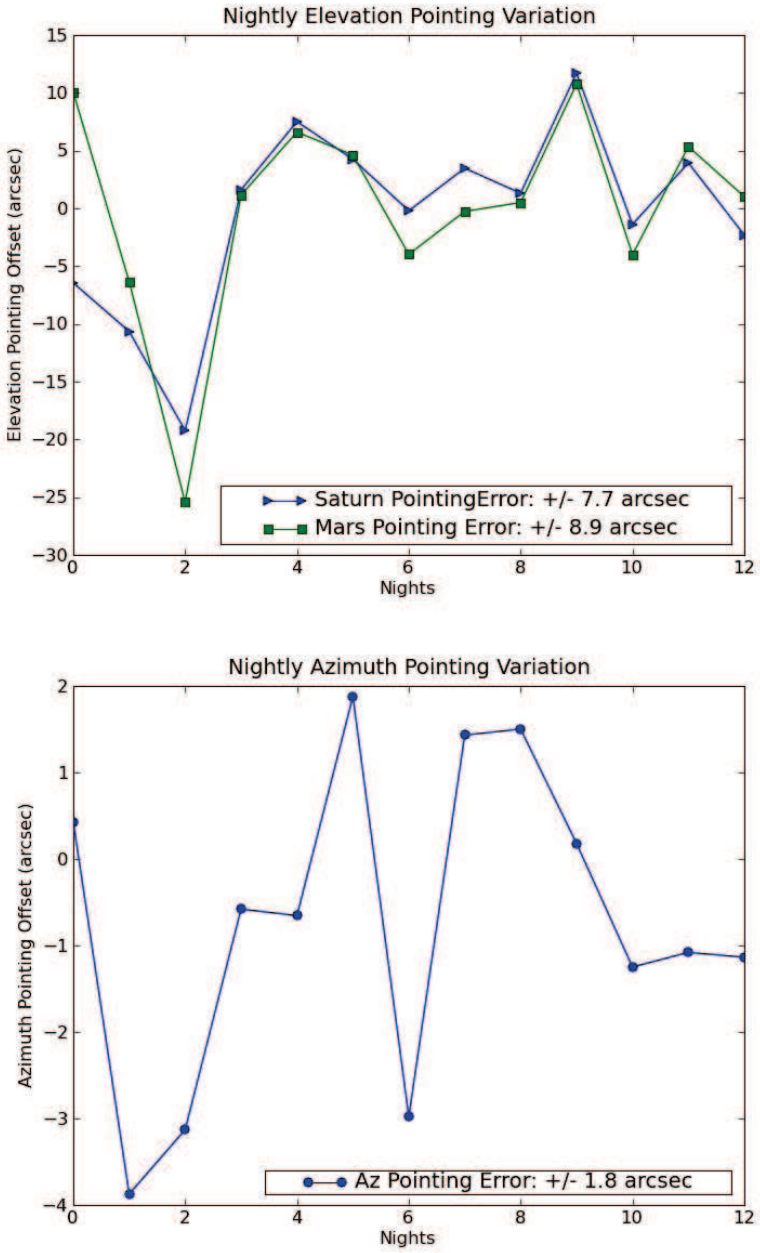

Figure 6.5 Telescope absolute pointing variation in elevation (top) and azimuth (bottom) over the 2007 observing season. The pointing offset is found by comparing the location of the planet peak in maps from several nights. The azimuth absolute pointing from night to night is stable. The elevation pointing has a large variation. In elevation, pointing offsets for both Mars and Saturn are similar for a given night. Section 6.3.1 describes a method to correct the elevation absolute pointing. The pointing error is the standard deviation of the measurements.

6.3.1 Night-by-Night Corrected Pointing Model

In order to improve the absolute elevation pointing to better than 8 arcseconds, a night-by-night corrected pointing model was developed. We measured the elevation offset for a given night from a centroid measure of a planet. A new offset was measured for each night. This adds a slight elevation correction to the global absolute pointing model for each night.

To assess how stable the measured pointing offset is from sky region to sky region, we compared offsets from Mars and Saturn observations taken on the same night. It is necessary to check this, because the model requires measuring the centroid of a planet in a different position than the survey region. The Saturn observations were taken at an azimuth of $\approx 37°$ and elevation of $50.5°$, while the Mars observations spanned telescope azimuths of $4°$–$28°$ and elevations of $37°$–$42°$. The resultant offsets for each planet are shown in Figure 6.5 for the thirteen nights they were both observed. There is clearly a correlation in the pointing offsets observed, but not perfect agreement. To accurately compare the two offsets, we must further account for the telescope pointing offsets induced from the changing azimuth and elevation over the different Mars observations (see Section 6.4). The elevation offsets were simultaneously fit as a function of telescope azimuth and elevation for the Mars observations and these telescope location pointing trends were removed. The elevation offset was then calculated from the Saturn observation and subtracted off of the detrended Mars elevation offset for each of the overlapping nights. The result is shown in Figure 6.6. The night-by-night corrected pointing in elevation gives an offset error of ± 2.5 arcseconds, a factor of 3 improvement over the random pointing variation.

This result confirms that the elevation offset is maintained as the telescope moves

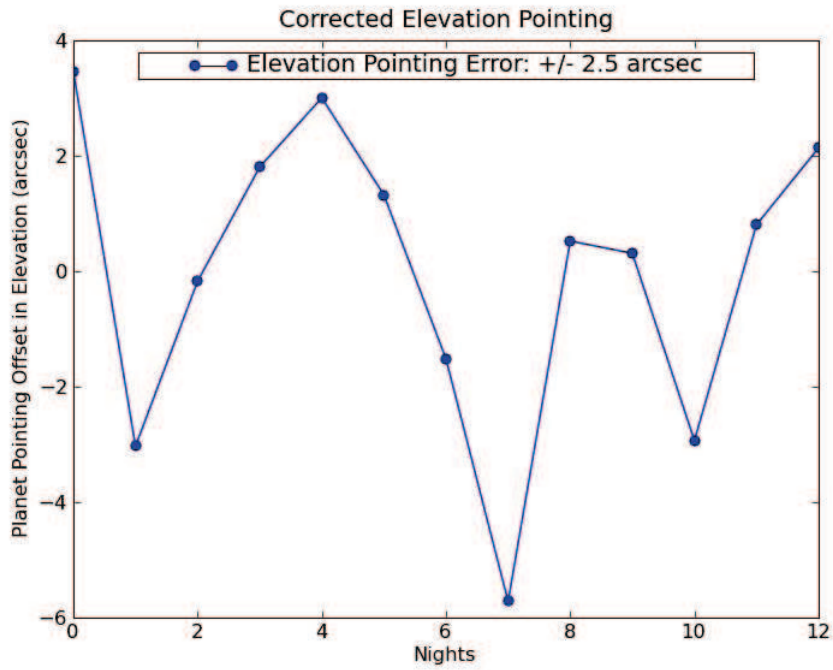

Figure 6.6 Night-by-night corrected elevation pointing for 13 nights over the course of the 2007 observing season. The pointing offset in elevation is measured from Saturn and used to correct the elevation offset for a scan of Mars on the same night.

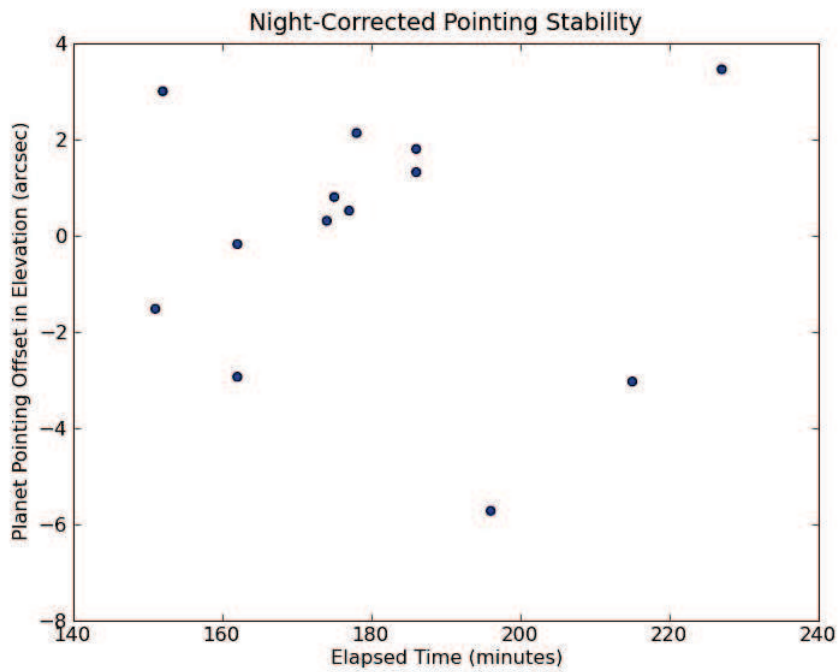

Figure 6.7 Night-by-night corrected stability in time. Elapsed time is between the Saturn and Mars observations. The Saturn observation was used to measure the elevation correction. Over four hours elapsed between when the pointing correction was measured and applied. There is not trend indicating that the pointing correction is degrading with time, indicating that the elevation offset stable throughout a night.

to different scan locations. The time difference between the two planet scans as a function of Mars corrected elevation pointing is shown in Figure 6.7. The two planet observations spanned a time difference of up to four hours. There is no indication that the pointing correction is worsening as the time between observations increases. This indicates that the absolute telescope elevation offset, while changing from night to night, is stable throughout the nightly observations. Therefore, we can use a single observation of a planet to correct the relative elevation offset on a nightly basis to improve the elevation pointing to $\lesssim$ 3 arcseconds.

6.3.2 Pointing Effects on the Window Function

To check the effects of pointing error on the window function, we computed beam window transfer functions over a symmetrized Airy beam pattern as described in Sections 5.4.3. We calculated the transfer function for our best estimate of the simulated ACT beam, which we estimate by convolving 9 Airy disks with the shear and rotation as given in Table 5.1 and cross linked these 9 Airy disks. We then created a beam including pointing errors. This beam is made by combining two best estimates of the ACT beams with an offset in azimuth and elevation between them when coadding and calculated the resulting transfer function. We did not put any pointing error in the cross linking. We take the ratio of these two models with a symmetric beam with no pointing error. This ratio is an estimate of how the pointing error will affect the power spectrum results. Figure 6.8 shows these ratios for our base pointing rms error of 1.8 arcseconds in azimuth and 8.9 arcseconds in elevation, and for the night-corrected pointing with 2.5 arcseconds error in elevation pointing. The pointing error will produce a $\sim 2\%$ error in the recovered transfer function for the non-corrected pointing model. If we improve the pointing error to ~ 2 arcseconds using the night-corrected model, we will reduce the error in the recovered power spectrum to less than 0.5% across all l out to multipole 10,000.

6.4 Telescope Position-Dependent Offsets

Changes in the telescope structure as the telescope moves in azimuth and elevation induce systematic errors in the absolute pointing. The causes of some of these structure deformations are understood, while others are not. A slight tilt in the telescope pedestal has been measured using inclinometers to be ≈ 20 arcseconds. This

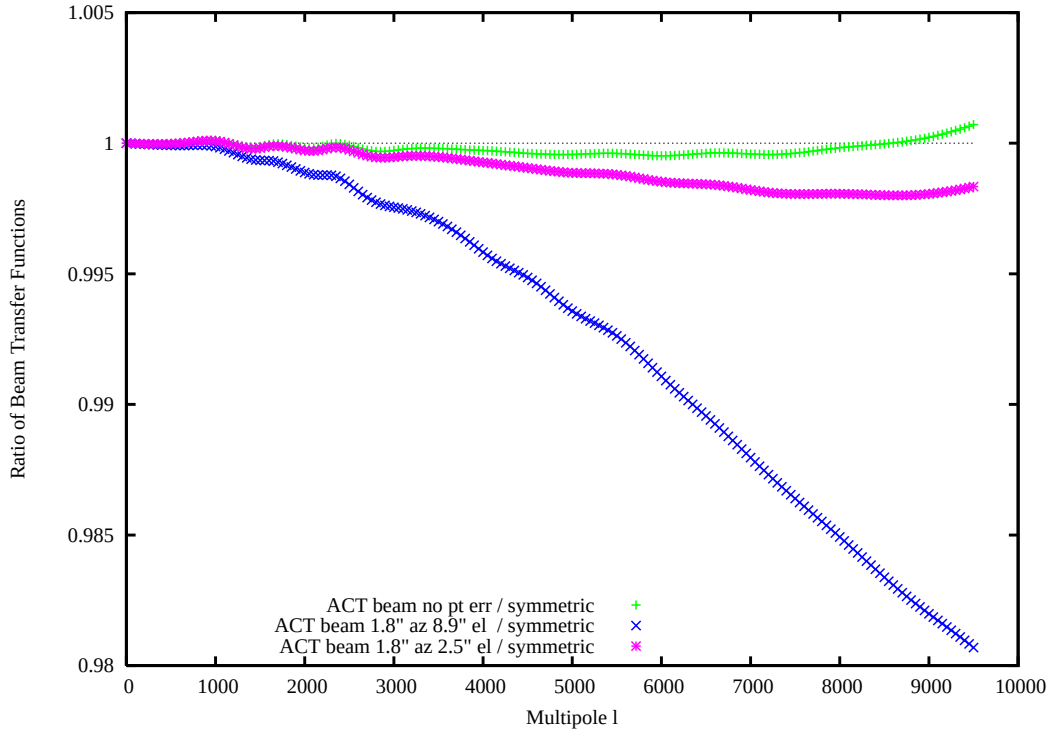

Figure 6.8 Ratio of beam window transfer functions with pointing error. Plotted are three estimates of our ACT beam compared to a symmetric beam. The green crosses have no pointing error, the magenta stars are for the night-corrected 1-σ pointing error, and the blue crosses are with the nominal 1-σ pointing error. The ratios are computed to a symmetric Airy disk with no pointing offset.

tilt changes the absolute pointing of the telescope elevation for different azimuths, in effect inducing an elevation offset as a function of telescope azimuth. This offset has been confirmed by measurements of planets at different telescope azimuths (top plot in Figure 6.9). A separate offset in elevation is induced when the telescope elevation is changed. To point the telescope to higher elevations the primary mirror and BUS are tilted back towards the ground. As this happens, the telescope center of mass is displaced, causing the telescope lower structure to tilt on the azimuth bearing. The primary is then pointed to a higher position on the sky than reported by the elevation encoder and the locations of measured sources are lower than otherwise expected. The bottom plot in Figure 6.9 shows the measured elevation pointing displacement of Mars as the telescope elevation is changed. This lifting causes ~ 3 arcseconds per degree elevation displacement in the absolute elevation pointing.

We have also measured offsets from the encoder azimuths as a function of both the telescope azimuth and elevation (Figure 6.10). The cause of these azimuthal offsets with telescope position are not known. One possible cause could be if the telescope elevation structure is not sitting flat on the telescope base. As the telescope center of mass changes, the BUS could shift slightly on the base, causing a telescope cant in azimuth.

The offsets with changing telescope elevation are important for determining a global pointing model, but are not critical to produce season-long survey maps because we map our survey region at the same elevation throughout the season. The offsets with changing telescope azimuth induce a global offset between the rising and setting maps in the survey region. To account for this, we make separate rising and setting maps and align the brightest point sources in each map to its known catalog sky positions, thus correcting for the azimuthal offsets and setting the global coordinates

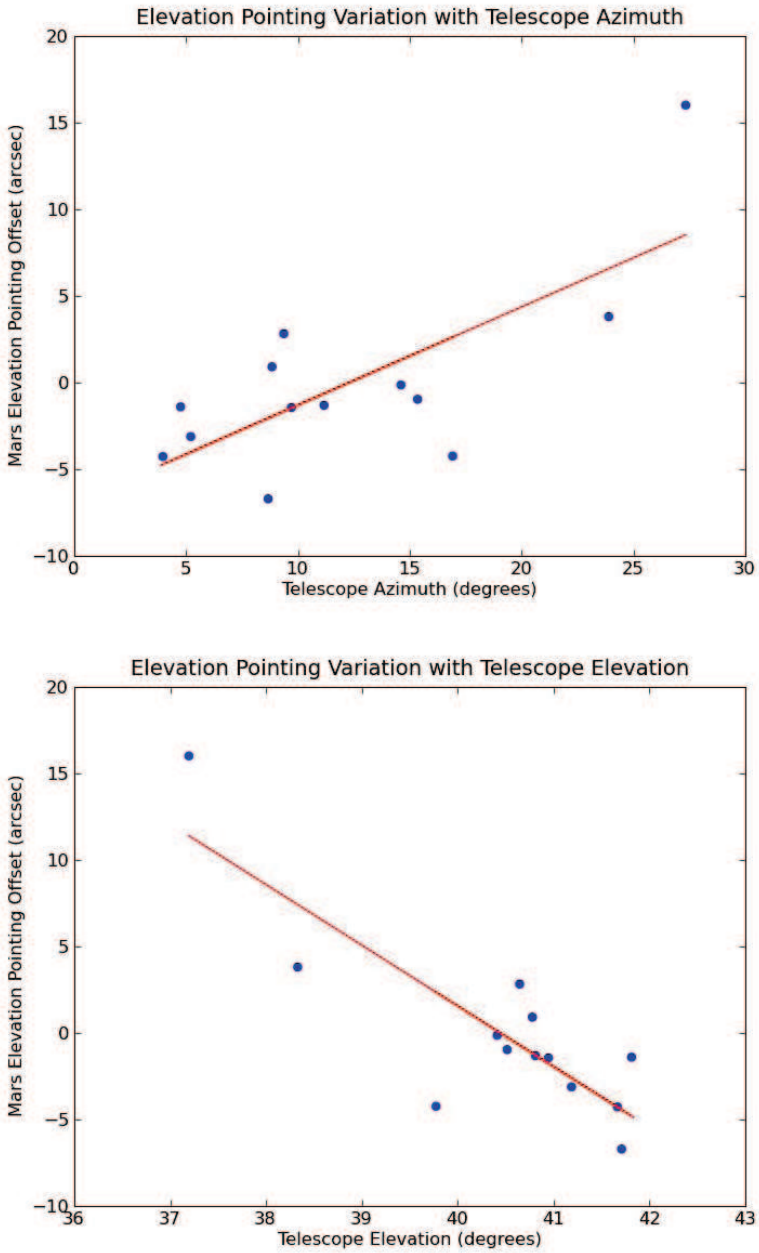

Figure 6.9 Absolute elevation pointing offsets dependent on telescope azimuth and elevation. *Top*: Change in Mars measured elevation with varying telescope azimuth. *Bottom*: Change in Mars measured elevation with changing telescope elevation. In both plots, the red line is a linear least-squares fit found by simultaneously fitting to both the telescope azimuth and elevation. By taking into account the temporal elevation dependence of the telescope (Section 6.3.1), the residuals to the fit give a 2.5 arcsecond 1-σ error in the elevation position of Mars.

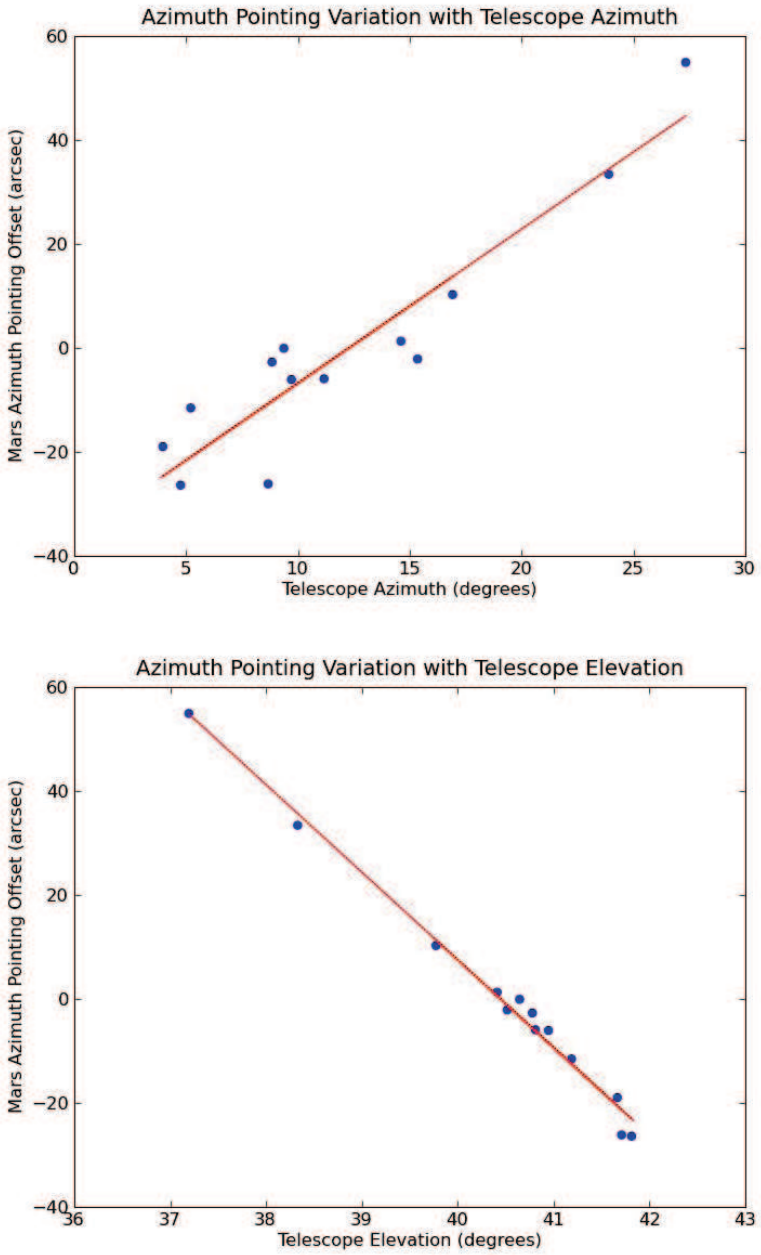

Figure 6.10 Absolute azimuth pointing offsets dependent on telescope azimuth and elevation. *Top*: Change in Mars measured azimuth with varying telescope azimuth. *Bottom*: Change in Mars measured azimuth with changing telescope elevation. In both plots, the red line is a linear least-squares fit found by simultaneously fitting to both the telescope azimuth and elevation. The residuals to the fit give a 1.9 arcsecond 1-σ error in the azimuth position of Mars.

in the survey maps. Furthermore, despite the fact that we do not know the cause of the azimuth variation, we have shown that if the telescope is returned to the same azimuth, the positional offset is small (Figure 6.5). To produce our survey maps, the telescope is scanned at constant elevation about the same azimuthal position from night to night, so this effect is not critical in this case.

Chapter 7

Current Status and Plans

The study of cosmology has developed rapidly over the last century. It has evolved from a field with few observations and vague theoretical conjecture, to a quantitative physical science where high-precision data and detailed theoretical empirical models have been used to develop a standard model of cosmology: the ΛCDM model. This model has been highly successful at constraining cosmological parameters by combining current observations from a broad range of experiments. The results from these data and the cosmological standard model lead to the startling conclusion that the Universe is expanding at an accelerating rate and much of the substance of the Universe is in an unknown form of energy known as dark energy. Fundamental questions remain, however, about the nature of the dark energy and the values of the cosmological parameters that govern the evolution of the Universe.

In this thesis, I have described a new experiment whose goals are to address these open questions by mapping the sky at millimeter wavelengths to measure the power spectrum of the CMB on angular scales that have previously never been measured and to detect galaxy clusters through their SZ signatures. The majority of the work

presented here is on the design, development, testing, and preliminary observations necessary for ACT to meet these challenging goals. The analysis from the commissioning in 2007 with a single array of detectors has allowed us to verify that the telescope and MBAC are working close to their design specifications. While the data reduction is not yet finalized, we have confirmed the detection of galaxy clusters through their tSZ signal. Figure 7.1 shows two maps of known clusters that were observed in the 100-square-degree Southern field during the first season.

A second observing season concluded recently in which a fully populated MBAC (three arrays simultaneously observing at 145, 220, and 280 GHz) observed approximately 500 square degrees for over 5 months from August to December 2008. Preliminary analysis suggests that there are approximately 800 hours of blind CMB science observations split roughly evenly in the Southern and Equatorial fields. Using detector sensitivity and data cut estimates from the 2007 season, we expect to achieve $\approx$ 25–30 µK per arcminute sensitivity in these regions at 145 GHz. Currently, an intense effort is underway to analyze these data. While much work remains, progress is advancing rapidly because of the data analysis pipeline development for the 2007 season's data. An example power spectrum for the 145 GHz map, using our sensitivity and sky coverage estimates for the 2007 season, is shown in Figure 7.2. We are also preparing for a third observing season to begin in May 2009. With the demonstrated success of the first two observing seasons, we expect to obtain another 7 months of CMB science observations. Currently, we plan to continue our observations in the Southern and Equatorial fields. With another 7 months of data, we will approach $\sim$ 15–20 µK sensitivity levels in our CMB maps. From these maps at multiple frequencies, we will produce a galaxy cluster catalog and a foreground-cleaned CMB map and power spectrum. These data products will be made public. The analysis of

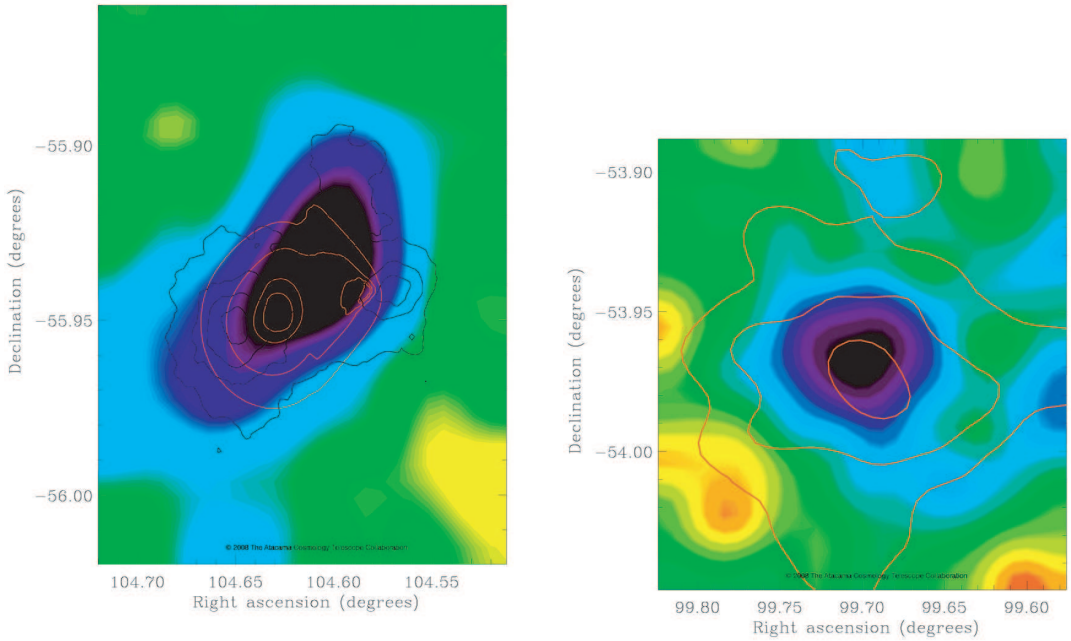

Figure 7.1 Preliminary galaxy cluster maps at 145 GHz. The color scale is intentionally omitted, as our calibration and map-making are under development. Each color indicates a 1-σ step in uncertainty. The maps have been smoothed with a 1.6 arcminute Gaussian. The plot on the left is the cluster 1E0656, the "Bullet Cluster", which is at a redshift of z $\approx$ 0.30. Over-plotted in red are X-ray surface density contours from the Chandra data and in black are weak lensing shear contours [Clowe et al., 2006]. The weak lensing and X-ray data are publicly available from the 1E0657 Official Project Page. The plot on the right is the cluster AS0952 at a redshift of $\approx$ 0.23 [Böhringer et al., 2004]. Overplotted are X-ray data from the publicly available ROSAT All Sky Survey. These clusters were not targeted; they were observed during our normal "blind" CMB science observations. They are meant to demonstrate the functionality of the telescope and receiver. Figure by the ACT Collaboration.

these data sets, especially when combined with follow-up observations, will improve our understanding of the fundamental nature of the Universe.

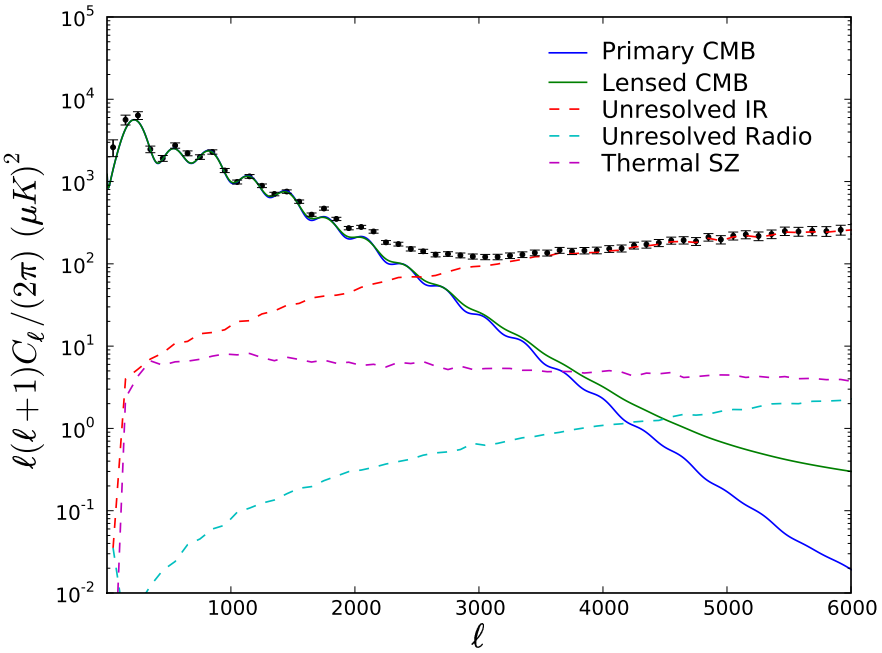

Figure 7.2 Estimated power spectrum for the 145 GHz-only map based on current sensitivity estimates and sky coverage for the 2008 observing season. The power spectrum is made from a simulation containing: a) CMB estimates with WMAP 3-year parameters, b) thermal SZ based on a model from Sehgal et al. [2007], c) radio sources based on a model from Y.T Lin, d) Infrared sources based on calculations by C. Hernandez-Monteagudo, e) lensed CMB estimates from Das and Bode [2008]. The solid curve for lensed and unlensed CMB are generated by the publicly available Code for Anisotropies in the Microwave Background (CAMB) [Lewis et al., 2000, CAMB] with WMAP 3-year parameter estimates. The dashed lines are estimated from respective simulations. A mask has been applied to block out the brightest radio and Infrared point sources. The error bars assume: 800 observation hours, 700 working detectors, sky coverage of 500 square degrees, detector sensitivity of 1 mK $\sqrt{s}$, estimated map sensitivity of 29 µK per arcminute in each 1.4 arcminute beam. The power spectrum is binned with bin-widths of 100. Figure made in collaboration with S. Das and T. Marriage.

Bibliography

1E0657 Official Project Page. http://flamingos.astro.ufl.edu/1e0657/public.html.

P.A.R. Ade, G. Pisano, C. Tucker, and S. Weaver. A review of metal mesh filters. volume 6275, pages 62750 – 1, USA, 2006.

A. Albrecht, G. Bernstein, R. Cahn, W. L. Freedman, J. Hewitt, W. Hu, J. Huth, M. Kamionkowski, E. W. Kolb, L. Knox, J. C. Mather, S. Staggs, and N. B. Suntzeff. Report of the Dark Energy Task Force. *ArXiv Astrophysics e-prints*, September 2006.

R.A. Alpher, H. Bethe, and G. Gamow. The origin of chemical elements. *Physical Review*, 73:803 – 804, 1948.

M. Arnaud and A. E. Evrard. The L_X-T relation and intracluster gas fractions of X-ray clusters. *MNRAS*, 305:631–640, May 1999.

D. Barbosa, J. G. Bartlett, and A. Blanchard. Constraining Ω_0 with Sunyaev-Zel'dovich Observations. *Astrophysics and Space Science*, 261:277, 1998.

E. S. Battistelli, M. Amiri, B. Burger, M. J. Devlin, S. R. Dicker, W. B. Doriese, R. D"unner, R. P. Fisher, J. W. Fowler, M. Halpern, M. Hasselfield, G. C. Hilton, A. D. Hincks, K. D. Irwin, M. Kaul, J. Klein, S. Knotek, J. M. Lau, M. Limon,

T. A. Marriage, M. D. Niemack, L. Page, C. D. Reintsema, S. T. Staggs, D. S. Swetz, E. R. Switzer, R. J. Thornton, and Y. Zhao. Automated SQUID tuning procedure for kilopixel arrays of TES bolometers on ACT. *Millimeter and Submillimeter Detectors and Instrumentation for Astronomy IV. Edited by William D. Duncan, Wayne S. Holland, Stafford Withington, Jonas Zmuidzinas. Proceedings of the SPIE*, 7020:702028, 2008b.

E. S. Battistelli, M. Amiri, B. Burger, M. Halpern, S. Knotek, M. Ellis, X. Gao, D. Kelly, M. MacIntosh, K. Irwin, and C. Reintsema. Functional description of read-out electronics for time-domain multiplexed bolometers for millimeter and sub-millimeter astronomy. *J. Low Temp. Phys.*, 151(3-4):908–914, 2008a.

J. W. Beeman and E.E. Haller. Far-infrared calibration sources for use in cryogenic telescopes. *Proc. SPIE*, 4486:209–218.

C.L. Bennett, M. Halpern, G. Hinshaw, N. Jarosik, A. Kogut, M. Limon, S.S. Meyer, L. Page, D.N. Spergel, G.S. Tucker, E. Wollack, E.L. Wright, C. Barnes, M.R. Greason, R.S. Hill, E. Komatsu, M.R. Nolta, N. Odegard, H.V. Peiris, L. Verde, and J.L. Weiland. First-year Wilkinson Microwave Anisotropy Probe (WMAP) observations: preliminary maps and basic results. *Astrophysical Journal Supplement Series*, 148(1):1 – 27, 2003. ISSN 0067-0049.

B. A. Benson, S. E. Church, P. A. R. Ade, J. J. Bock, K. M. Ganga, J. R. Hinderks, P. D. Mauskopf, B. Philhour, M. C. Runyan, and K. L. Thompson. Peculiar Velocity Limits from Measurements of the Spectrum of the Sunyaev-Zeldovich Effect in Six Clusters of Galaxies. *ApJ*, 592:674–691, August 2003. doi: 10.1086/375864.

B. A. Benson, S. E. Church, P. A. R. Ade, J. J. Bock, K. M. Ganga, C. N. Henson,

and K. L. Thompson. Measurements of Sunyaev-Zel'dovich Effect Scaling Relations for Clusters of Galaxies. *ApJ*, 617:829–846, December 2004. doi: 10.1086/425677.

M. Birkinshaw, J. P. Hughes, and K. A. Arnaud. A measurement of the value of the Hubble constant from the X-ray properties and the Sunyaev-Zel'dovich effect of Abell 665. *ApJ*, 379:466–481, October 1991. doi: 10.1086/170522.

J. J. Bock. *Rocket-borne observation of singly ionized carbon 158 micron emission from the diffuse interstellar medium*. PhD thesis, University of California at Berkeley, 1994.

H. Böhringer, P. Schuecker, L. Guzzo, C. A. Collins, W. Voges, R. G. Cruddace, A. Ortiz-Gil, G. Chincarini, S. De Grandi, A. C. Edge, H. T. MacGillivray, D. M. Neumann, S. Schindler, and P. Shaver. The ROSAT-ESO Flux Limited X-ray (REFLEX) Galaxy cluster survey. V. The cluster catalogue. *A&A*, 425:367–383, October 2004. doi: 10.1051/0004-6361:20034484.

J.R. Bond, S. Cole, G. Efstathiou, and N. Kaiser. Excursion set mass functions for hierarchical Gaussian fluctuations. *Astrophysical Journal*, 379(2):440 – 60, 1991. ISSN 0004-637X.

M. Born and E. Wolf. *Principles of Optics*. Cambridge University Press, 7th edition, 1999.

CAMB. http://camb.info/.

J. E. Carlstrom, M. Joy, and L. Grego. Interferometric Imaging of the Sunyaev-Zeldovich Effect at 30 GHz. *ApJ*, 456:L75+, January 1996. doi: 10.1086/309866.

J. E. Carlstrom, M. K. Joy, L. Grego, G. P. Holder, W. L. Holzapfel, J. J. Mohr, S. Patel, and E. D. Reese. Imaging the Sunyaev-Zel'dovich Effect. *Physica Scripta Volume T*, 85:148–+, 2000. doi: 10.1238/Physica.Topical.085a00148.

J. E. Carlstrom, G. P. Holder, and E. D. Reese. Cosmology with the Sunyaev-Zel'dovich Effect. *Ann. Rev. Astrophys.*, 40:643–680, 2002.

Sean .M. Carroll. *An Introduction to General Relativity, Spacetime and Geometry.* Addison Wesley Publishing Company, 2003.

J.A. Chervanek, K.D. Irwin, E.N. Grossman, J.M. Martinins, C.D. Reintsema, and M.E. Huber. Superconducting multiplexer for arrays of transition edge sensors. *Applied Physics Letters*, 74(26):4043 – 5, 1999. ISSN 0003-6951.

D. Clowe, M. Bradač, A. H. Gonzalez, M. Markevitch, S. W. Randall, C. Jones, and D. Zaritsky. A Direct Empirical Proof of the Existence of Dark Matter. *ApJ*, 648: L109–L113, September 2006. doi: 10.1086/508162.

L. Danese and R.B. Partridge. Atmospheric emission models: confrontation between observational data and predictions in the 2.5-300 GHz frequency range. *Astrophysical Journal*, 342(1):604 – 15, 1989. ISSN 0004-637X.

S. Das and P. Bode. A Large Sky Simulation of the Gravitational Lensing of the Cosmic Microwave Background. *ApJ*, 682:1–13, July 2008.

A. De Oliveira-Costa, M. Tegmark, D.P. Finkbeiner, R.D. Davies, C.M. Gutierrez, L.M. Haffner, A.W. Jones, A.N. Lasenby, R. Rebolo, R.J. Reynolds, S.L. Tufte, and R.A. Watson. A new spin on Galactic dust. *Astrophysical Journal*, 567(1):363 – 9, 2002. ISSN 0004-637X.

M. J. Devlin, S. R. Dicker, J. Klein, and M. P. Supanich. A high capacity completely closed-cycle 250 mk ^{3}He refrigeration system based on a pulse tube cooler. *Cryogenics*, 44:611–616, 2004.

Simon Dicker. Act cold optics–v26, 2005. Internal ACT Memo.

Scott. Dodelson. *Modern Cosmology*. Academic Press, 2003.

J. Dunkley, E. Komatsu, M. R. Nolta, D. N. Spergel, D. Larson, G. Hinshaw, L. Page, C. L. Bennett, B. Gold, N. Jarosik, J. L. Weiland, M. Halpern, R. S. Hill, A. Kogut, M. Limon, S. S. Meyer, G. S. Tucker, E. Wollack, and E. L. Wright. Five-Year Wilkinson Microwave Anisotropy Probe Observations: Likelihoods and Parameters from the WMAP Data. *ApJS*, 180:306–329, February 2009.

Efunda Engineering Fundamentals. http://www.efunda.com.

J. W. Fowler, M. D. Niemack, S. R. Dicker, A. M. Aboobaker, P. A. R. Ade, E. S. Battistelli, M. J. Devlin, R. P. Fisher, M. Halpern, P. C. Hargrave, A. D. Hincks, M. Kaul, J. Klein, J. M. Lau, M. Limon, T. A. Marriage, P. D. Mauskopf, L. Page, S. T. Staggs, D. S. Swetz, E. R. Switzer, R. J. Thornton, and C. E. Tucker. Optical design of the Atacama Cosmology Telescope and the Millimeter Bolometric Array Camera. *Appl. Opt.*, 46(17):3444–3454, 2007.

J. Glenn, P. A. R. Ade, M. Amarie, J. J. Bock, S. F. Edgington, A. Goldin, S. Golwala, D. Haig, A. E. Lange, G. Laurent, P. D. Mauskopf, M. Yun, and H. Nguyen. Current status of Bolocam: a large-format millimeter-wave bolometer camera. In T. G. Phillips and J. Zmuidzinas, editors, *Society of Photo-Optical Instrumentation Engineers (SPIE) Conference Series*, volume 4855 of *Society of Photo-Optical*

Instrumentation Engineers (SPIE) Conference Series, pages 30–40, February 2003. doi: 10.1117/12.459369.

T. Herbig, C. R. Lawrence, A. C. S. Readhead, and S. Gulkis. A Measurement of the Sunyaev-Zel'dovich Effect in the Coma Cluster of Galaxies. *ApJ*, 449:L5+, August 1995. doi: 10.1086/309616.

Carlos Hernandez-Monteagudo, Licia Verde, Raul Jimenez, and David N. Spergel. Correlation properties of the kinematic Sunyaev-Zel'dovich effect and implications for dark energy. *The Astrophysical Journal*, 643(2):598–615, 2006.

A. D. Hincks, P. A. R. Ade, C. Allen, M. Amiri, J. W. Appel, E. S. Battistelli ANDB. Burger, J. A. Chervenak, A. J. Dahlen, S. Denny, M. J. Devlin, S. R. Dicker, W. B. Doriese, R. Dünner, T. Essinger-Hileman, R. P. Fisher, J. W. Fowler, M. Halpern, P. C.Hargrave, M. Hasselfield, G. C. Hilton, K. D. Irwin, N. Jarosik, M. Kaul, J. Klein, J. M. Lau, M. Limon, R. H. Lupton, T. A. Marriage, K. L. Martocci, P. Mauskopf, S. H. Moseley, C. B. Netterfield, M. D. Niemack, M. R. Nolta, L. Page, L. P. Parker, A. J. Sederberg, S. T. Staggs, O. R. Stryzak, D. S. Swetz, E. R. Switzer, R. J. Thornton, C. Tucker, E. J. Wollack, and Y. Zhao. The effects of the mechanical performance and alignment of the Atacama Cosmology Telescope on the sensitivity of microwave observations. *Millimeter and Submillimeter Detectors and Instrumentation for Astronomy IV. Edited by William D. Duncan, Wayne S. Holland, Stafford Withington, Jonas Zmuidzinas. Proceedings of the SPIE*, 7020: 70201P, 2008.

G. Holder, Z. Haiman, and J. J. Mohr. Constraints on Ω_m, Ω_Λ, and σ_8 from

Galaxy Cluster Redshift Distributions. *ApJ*, 560:L111–L114, October 2001. doi: 10.1086/324309.

W. L. Holzapfel, T. M. Wilbanks, P. A. R. Ade, S. E. Church, M. L. Fischer, P. D. Mauskopf, D. E. Osgood, and A. E. Lange. The Sunyaev-Zeldovich Infrared Experiment: A Millimeter-Wave Receiver for Cluster Cosmology. *ApJ*, 479:17–+, April 1997. doi: 10.1086/303840.

W. Hu, M. M. Hedman, and M. Zaldarriaga. Benchmark parameters for CMB polarization experiments. *Phys. Rev. D*, 67(4):043004–+, February 2003.

E. Hubble. Distance and radial velocity among extra-galactic nebulae;. *Proceedings of the National Academy of Sciences of the United States of America*, 15:168 – 173, 1929.

K. D. Irwin. An application of electrothermal feedback for high resolution cryogenic particle detection. *Applied Physics Letters*, 66(15):1998–2000, 1995.

K.D. Irwin. Thermodynamics of nonlinear bolometers near equilibrium. *Nuclear Instruments & Methods in Physics Research, Section A (Accelerators, Spectrometers, Detectors and Associated Equipment)*, 559(2):718 – 20, 2006. ISSN 0168-9002.

K.D. Irwin and G.C. Hilton. *Cryogenic Particle Detection*. Springer–Verlag, Berlin, Germany, 2005.

N. Itoh, Y. Kohyama, and S. Nozawa. Relativistic corrections to the Sunyaev-Zeldovich effect for clusters of galaxies. *Astrophysical Journal*, 502(1):7 – 15, 1998. ISSN 0004-637X.

N. Jarosik, C. Barnes, M. R. Greason, R. S. Hill, M. R. Nolta, N. Odegard, J. L. Weiland, R. Bean, C. L. Bennett, O. Doré, M. Halpern, G. Hinshaw, A. Kogut, E. Komatsu, M. Limon, S. S. Meyer, L. Page, D. N. Spergel, G. S. Tucker, E. Wollack, and E. L. Wright. Three-Year Wilkinson Microwave Anisotropy Probe (WMAP) Observations: Beam Profiles, Data Processing, Radiometer Characterization, and Systematic Error Limits. *ApJS*, 170:263–287, June 2007.

M. Jones, R. Saunders, P. Alexander, M. Birkinshaw, N. Dilon, K. Grainge, S. Hancock, A. Lasenby, D. Lefebvre, and G. Pooley. An image of the Sunyaev-Zel'dovich effect. *Nature*, 365:320–323, September 1993. doi: 10.1038/365320a0.

A. R. Kerr, N. J. Bailey, D. E. Boyd, and N. Horner. A Study of Materials for a Broadband Millimeter-Wave Quasi-Optical Vacuum Window, 1992. Natioinal Radio Astronomy Observatory MMA Memorandum # 90.

E. Komatsu, J. Dunkley, M. R. Nolta, C. L. Bennett, B. Gold, G. Hinshaw, N. Jarosik, D. Larson, M. Limon, L. Page, D. N. Spergel, M. Halpern, R. S. Hill, A. Kogut, S. S. Meyer, G. S. Tucker, J. L. Weiland, E. Wollack, and E. L. Wright. Five-Year Wilkinson Microwave Anisotropy Probe Observations: Cosmological Interpretation. *ApJS*, 180:330–376, February 2009.

A. Kosowsky. The Atacama Cosmology Telescope. *New Astronomy Review*, 47:939–943, December 2003. doi: 10.1016/S1387-6473(03)00214-8.

J.W. Lamb. Miscellaneous data on materials for millimetre and submillimetre optics. *International Journal of Infrared and Millimeter Waves*, 17(12):1997 – 2034, 1996. ISSN 0195-9271.

J. Lau, M. Benna, M. Devlin, S. Dicker, and L. Page. Experimental tests and modeling of the optimal orifice size for a closed cycle ^{4}He sorption refridgerator. *Cryogenics*, 46:809–814, 2006a.

J. Lau, J. Fowler, T. Marriage, L. Page, J. Leong, E. Wishnow, R. Henry, E. Wollack, M. Halpern, D. Marsden, and G. Marsden. Millimeter-wave antireflection coating for cryogenic silicon lenses. *Appl. Opt.*, 45:3746–3751, 2006b.

Judy Lau. *CCAM: A Novel Millimeter-Wave Instrument Using a Close-Packed TES Bolometer Array.* PhD thesis, Princeton University, 2006.

Antony Lewis, Anthony Challinor, and Anthony Lasenby. Efficient computation of CMB anisotropies in closed FRW models. *Astrophys. J.*, 538:473–476, 2000.

M. J. Li, C. A. Allen, S. A. Gordon, J. L. Kuhn, D. B. Mott, C. K. Stahle, and L. L. Wang. Fabrication of pop-up detector arrays on Si wafers. In J. H. Smith and J.-M. Karam, editors, *Society of Photo-Optical Instrumentation Engineers (SPIE) Conference Series*, volume 3874 of *Society of Photo-Optical Instrumentation Engineers (SPIE) Conference Series*, pages 422–431, August 1999.

M. Lima and W. Hu. Self-calibration of cluster dark energy studies: Observable-mass distribution. *Phys. Rev. D*, 72(4):043006–+, August 2005. doi: 10.1103/PhysRevD.72.043006.

R.H. Lupton. *Statistics in Theory and Practice.* Princeton University Press, 1993.

T. A. Marriage, J. A. Chervenak, and W. B. Doriese. Testing and assembly of the detectors for the Millimeter Bolometric Array Camera on ACT. *Nuc Inst & Meth. in Phys Res A*, 559:551–553, 2006.

Tobias Andrew Marriage. Radiation loading for an act bolometer, 2004. Internal ACT Memo.

Tobias Andrew Marriage. *Detectors for the Atacama Cosmology Telescope*. PhD thesis, Princeton University, 2006.

B. S. Mason, S. T. Myers, and A. C. S. Readhead. A Measurement of H_0 from the Sunyaev-Zeldovich Effect. *ApJ*, 555:L11–L15, July 2001. doi: 10.1086/321737.

J.C. Mather, E.S. Cheng, Jr. Eplee, R.E., R.B. Isaacman, S.S. Meyer, R.A. Shafer, R. Weiss, E.L. Wright, C.L. Bennett, N.W. Boggess, E. Dwek, S. Gulkis, M.G. Hauser, M. Janssen, T. Kelsall, P.M. Lubin, Jr. Moseley, S.H., T.L. Murdock, R.F. Silverberg, G.F. Smoot, and D.T. Wilkinson. A preliminary measurement of the cosmic microwave background spectrum by the Cosmic Background Explorer (COBE) satellite. *Astrophysical Journal, Letters*, 354(2):37 – 40, 1990.

S.H. Moseley, J.C. Mather, and D. McCammon. Thermal detectors as X-ray spectrometers. *Journal of Applied Physics*, 56(5):1257 – 62, 1984. ISSN 0021-8979.

S. T. Myers, J. E. Baker, A. C. S. Readhead, E. M. Leitch, and T. Herbig. Measurements of the Sunyaev-Zeldovich Effect in the Nearby Clusters A478, A2142, and A2256. *ApJ*, 485:1–+, August 1997. doi: 10.1086/304389.

C.B. Netterfield, M.J. Devlin, N. Jarosik, L. Page, and E.J. Wollack. A measurement of the angular power spectrum of the anisotropy in the Cosmic Microwave Background. *Astrophysical Journal*, 474(1):47 – 66, 1997. ISSN 0004-637X.

M. D. Niemack, Y. Zhao, E. Wollack, R. Thornton, E. R. Switzer, D. S. Swetz, S. T. Staggs, L. Page, O. Stryzak, H. Moseley, T. A. Marriage, M. Limon, J. M. Lau,

J. Klein, M. Kaul, N. Jarosik, K. D. Irwin, A. D. Hincks, G. C. Hilton, M. Halpern, J. W. Fowler, R. P. Fisher, R. Dünner, W. B. Doriese, S. R. Dicker, M. J. Devlin, J. Chervenak, B. Burger, E. S. Battistelli, J. Appel, M. Amiri, C. Allen, and A. M. Aboobaker. A kilopixel array of TES bolometers for ACT: Development, testing, and first light. *J. Low Temp. Phys.*, 151(3-4):690–696, 2008.

Michael D. Niemack. *Towards Dark Energy: Design, Development, and Preliminary Data from ACT*. PhD thesis, Princeton University, 2008.

M. R. Nolta, J. Dunkley, R. S. Hill, G. Hinshaw, E. Komatsu, D. Larson, L. Page, D. N. Spergel, C. L. Bennett, B. Gold, N. Jarosik, N. Odegard, J. L. Weiland, E. Wollack, M. Halpern, A. Kogut, M. Limon, S. S. Meyer, G. S. Tucker, and E. L. Wright. Five-Year Wilkinson Microwave Anisotropy Probe Observations: Angular Power Spectra. *ApJS*, 180:296–305, February 2009.

F. Pace, M. Maturi, M. Bartelmann, N. Cappelluti, K. Dolag, M. Meneghetti, and L. Moscardini. Statistical properties of SZ and X-ray cluster detections. *A&A*, 483: 389–400, May 2008.

L. Page, C. Barnes, G. Hinshaw, D.N. Spergel, J.L. Weiland, E. Wollack, C.L. Bennett, M. Halpern, N. Jarosik, N. Kogut, M. Limon, S.S. Meyer, G.S. Tucker, and E.L. Wright. First-year Wilkinson Microwave Anisotropy Probe (WMAP) observations: beam profiles and window functions. *Astrophysical Journal Supplement Series*, 148(1):39 – 50, 2003. ISSN 0067-0049.

J.R. Pardo, J. Cernicharo, and E. Serabyn. Atmospheric transmission at microwaves (ATM): an improved model for millimeter/submillimeter applications. *IEEE Transactions on Antennas and Propagation*, 49(12):1683 – 94, 2001. ISSN 0018-926X.

Parker O-Ring Handbook. http://www.parker.com/literature.

A.A. Penzias and R.W. Wilson. A measurement of excess antenna temperature at 4080 Mc/s. *Astrophysical Journal*, 142(1):419 – 421, 1965.

W. H. Press, S. A. Teukolsky, W. T. Vetterling, and B. P. Flannery. *Numerical Recipes: the Art of Scientific Computing*. Cambridge University Press, 1992.

W.H. Press and P. Schechter. Formation of galaxies and clusters of galaxies by self-similar gravitational condensation. *Astrophysical Journal*, 187(3):425 – 38, 1974. ISSN 0004-637X.

S. J. E. Radford. Site characterizations for mm/submm astronomy. *ASP Conference Series*, (266):148, 2002.

S. J. E. Radford, B. J. Butler, S. Sakamoto, and K. Kohno. Atmospheric transparency at chajnantor and pampa la bola. *ALMA Memo 384*, 2001.

E. D. Reese, J. E. Carlstrom, M. Joy, J. J. Mohr, L. Grego, and W. L. Holzapfel. Determining the Cosmic Distance Scale from Interferometric Measurements of the Sunyaev-Zeldovich Effect. *ApJ*, 581:53–85, December 2002. doi: 10.1086/344137.

P. L. Richards. Bolometers for infrared and millimeter waves. *Journal of Applied Physics*, 76:1–24, July 1994. doi: 10.1063/1.357128.

K Rohlfs and T.L. Wilson. *Tools of Radio Astronomy*. Springer-Verlag, 1996.

ROSAT All Sky Survey. http://www.xray.mpe.mpg.de/cgi-bin/rosat/rosat-survey.

J. Ruhl, P. A. R. Ade, J. E. Carlstrom, H.-M. Cho, T. Crawford, M. Dobbs, C. H. Greer, N. w. Halverson, W. L. Holzapfel, T. M. Lanting, A. T. Lee, E. M. Leitch,

J. Leong, W. Lu, M. Lueker, J. Mehl, S. S. Meyer, J. J. Mohr, S. Padin, T. Plagge, C. Pryke, M. C. Runyan, D. Schwan, M. K. Sharp, H. Spieler, Z. Staniszewski, and A. A. Stark. The South Pole Telescope. In C. M. Bradford, P. A. R. Ade, J. E. Aguirre, J. J. Bock, M. Dragovan, L. Duband, L. Earle, J. Glenn, H. Matsuhara, B. J. Naylor, H. T. Nguyen, M. Yun, and J. Zmuidzinas, editors, *Society of Photo-Optical Instrumentation Engineers (SPIE) Conference Series*, volume 5498 of *Society of Photo-Optical Instrumentation Engineers (SPIE) Conference Series*, pages 11–29, October 2004. doi: 10.1117/12.552473.

M. C. Runyan, P. A. R. Ade, R. S. Bhatia, J. J. Bock, M. D. Daub, J. H. Goldstein, C. V. Haynes, W. L. Holzapfel, C. L. Kuo, A. E. Lange, J. Leong, M. Lueker, M. Newcomb, J. B. Peterson, C. Reichardt, J. Ruhl, G. Sirbi, E. Torbet, C. Tucker, A. D. Turner, and D. Woolsey. ACBAR: The Arcminute Cosmology Bolometer Array Receiver. *ApJS*, 149:265–287, December 2003. doi: 10.1086/379099.

J. Ruze. Antenna tolerance theory – a review. *Proc. IEEE*, 54:633–640, 1966.

D. Schroeder. *Astronomical Optics*. Academic Press, 2nd edition, 2000.

N. Sehgal. Forecasts for SZ Clusters for ACT, 2008. ACT "Back to School" Meeting.

N. Sehgal, Hy Trac, K. Huffenberger, and P. Bode. Microwave sky simulations and projections for galaxy cluster detection with the Atacama Cosmology Telescope. *Astrophysical Journal*, 664(1):149 – 61, 2007. ISSN 0004-637X.

J. Silk. Cosmic black-body radiation and galaxy formation. *Astrophysical Journal*, 151(2):459 – 472, 1968.

Z. Staniszewski, P. A. R. Ade, K. A. Aird, B. A. Benson, L. E. Bleem, J. E. Carlstrom,

C. L. Chang, H. . Cho, T. M. Crawford, A. T. Crites, T. de Haan, M. A. Dobbs, N. W. Halverson, G. P. Holder, W. L. Holzapfel, J. D. Hrubes, M. Joy, R. Keisler, T. M. Lanting, A. T. Lee, E. M. Leitch, A. Loehr, M. Lueker, J. J. McMahon, J. Mehl, S. S. Meyer, J. J. Mohr, T. E. Montroy, C. . Ngeow, S. Padin, T. Plagge, C. Pryke, C. L. Reichardt, J. E. Ruhl, K. K. Schaffer, L. Shaw, E. Shirokoff, H. G. Spieler, B. Stalder, A. A. Stark, K. Vanderlinde, J. D. Vieira, O. Zahn, and A. Zenteno. Galaxy clusters discovered with a Sunyaev-Zel'dovich effect survey. *ArXiv e-prints*, October 2008.

R.A. Sunyaev and Ya.B. Zeldovich. The observation of relic radiation as a test of the nature of X-ray radiation from the clusters of galaxies. *Comments on Astrophysics and Space Physics*, 4(6):173 – 8, 1972. ISSN 0010-2679.

E. R. Switzer, C. Allen, M. Amiri, J. Appel, E. S. Battistelli, B. Burger, J. Chervenak, A. Dahlen, S. Das, M. J. Devlin, S. R. Dicker, W. B. Doriese, R. Dünner, T. Essinger-Hileman, R. P. Fisher, J. W. Fowler X. Gao, M. Halpern, M. Hasselfield, G. C. Hilton, A. D. Hincks, K. D. Irwin, N. Jarosik, M. Kaul, S. Knotek, J. Klein, J. M. Lau, M. Limon, R. Lupton, T. A. Marriage, K. Martocci, H. Moseley, B. Netterfield, M. D. Niemack, M. Nolta, L. Page, L. Parker, B. Reid, C. D. Reintsema, A. Sederberg, J. Sievers, D. Spergel, S. T. Staggs, O. Stryzak, D. S. Swetz, R. Thornton, E. Wollack, and Y. Zhao. System and control software for the Atacama Cosmology Telescope. *Millimeter and Submillimeter Detectors and Instrumentation for Astronomy IV. Edited by William D. Duncan, Wayne S. Holland, Stafford Withington, Jonas Zmuidzinas. Proceedings of the SPIE*, 7019:70192L, 2008.

Eric R. Switzer. *Small-Scale Anisotropies of the Cosmic Microwave Background:*

Experimental and Theoretical Perspectives. PhD thesis, Princeton University, 2008.

M. Tegmark. CMB mapping experiments: a designer's guide. *Physical Review D*, 56 (8):4514 – 29, 1997. ISSN 0556-2821.

M. Tegmark, D.J. Eisenstein, W. Hu, and A. de Oliveira-Costa. Foregrounds and forecasts for the Cosmic Microwave Background. *Astrophysical Journal*, 530(1):133 – 65, 2000. ISSN 0004-637X.

R. J. Thornton, P. A. R. Ade, C. Allen, M. Amiri, J. Appel, E. S. Battistelli, B. Burger, J. Chervenak, M. J. Devlin, S. R. Dicker, W. B. Doriese, T. Essinger-Hileman, R. P. Fisher, J. W. Fowler, M. Halpern, P. C Hargrave, M. Hasselfield, G. C. Hilton, A. D. Hincks, K. D. Irwin, N. Jarosik, M. Kaul, J. Klein, J. M. Lau, M. Limon, T. A. Marriage, K. Martocci, P. Mauskopf, H. Moseley, M. D. Niemack, L. Page, L. P. Parker, J. Reidel, C. D. Reintsema, S. T. Staggs, O. R. Stryzak, D. S. Swetz, E. R. Switzer, C. Tucker, E. J. Wollack, and Y. Zhao. Optomechanical design and performance of a compact three-frequency camera for the MBAC receiver on the Atacama Cosmology Telescope. *Millimeter and Submillimeter Detectors and Instrumentation for Astronomy IV. Edited by William D. Duncan, Wayne S. Holland, Stafford Withington, Jonas Zmuidzinas. Proceedings of the SPIE*, 7020: 70201R, 2008.

Michael Tinkham. *Introduction to Superconductivity*. McGraw-Hill, 1996.

Carole E. Tucker and Peter A.R. Ade. Thermal filtering for large aperture cryogenic detector arrays. *Proc. SPIE*, 6275:62750T, 2006.

S. Wang, J. Khoury, Z. Haiman, and M. May. Constraining the evolution of dark

energy with a combination of galaxy cluster observables. *Phys. Rev. D*, 70(12): 123008–+, December 2004. doi: 10.1103/PhysRevD.70.123008.

Jongsoo Yoon, J. Clarke, J.M. Gildemeister, A.T. Lee, M.J. Myers, P.L. Richards, and J.T. Skidmore. Single superconducting quantum interference device multiplexer for arrays of low-temperature sensors. *Applied Physics Letters*, 78(3):371 – 3, 2001. ISSN 0003-6951.

K. W. Yoon, P. A. R. Ade, D. Barkats, J. O. Battle, E. M. Bierman, J. J. Bock, J. A. Brevik, H. C. Chiang, A. Crites, C. D. Dowell, L. Duband, G. S. Griffin, E. F. Hivon, W. L. Holzapfel, V. V. Hristov, B. G. Keating, J. M. Kovac, C. L. Kuo, A. E. Lange, E. M. Leitch, P. V. Mason, H. T. Nguyen, N. Ponthieu, Y. D. Takahashi, T. Renbarger, L. C. Weintraub, and D. Woolsey. The Robinson Gravitational Wave Background Telescope (BICEP): a bolometric large angular scale CMB polarimeter. In *Society of Photo-Optical Instrumentation Engineers (SPIE) Conference Series*, volume 6275 of *Society of Photo-Optical Instrumentation Engineers (SPIE) Conference Series*, July 2006. doi: 10.1117/12.672652.

Y. Zhao, C. Allen, M. Amiri, J. W. Appel, E. S. Battistelli, B. Burger, J. A. Chervenak, A. Dahlen, S. Denny, M. J. Devlin, S. R. Dicker, W. B. Doriese, R. Dünner, T. Essinger-Hileman, R. P. Fisher, J. W. Fowler, M. Halpern, G. C. Hilton, A. D. Hincks, K. D. Irwin, N. Jarosik, J. Klein, J. M. Lau, T. A. Marriage, K. Martocci, H. Moseley, M. D. Niemack, L. Page, L. P. Parker, A. Sederberg, S. T. Staggs, O. R. Stryzak, D. S. Swetz, E. R. Switzer, R. J. Thornton, and E. J. Wollack. Characterization of transition edge sensors for the Millimeter Bolometer Array Camera on the Atacama Cosmology Telescope. *Millimeter and Submillimeter Detectors and Instrumentation for Astronomy IV. Edited by William D. Duncan, Wayne S.*

Holland, Stafford Withington, Jonas Zmuidzinas. Proceedings of the SPIE, 7020: 70200O, 2008.